8-18-2017

Structural Health Monitoring of Buildings for Safety Assessments Under Explosions

Edward Eskew
University of Connecticut - Storrs, edward.eskew@uconn.edu

Structural Health Monitoring of Buildings for Safety Assessments Under Explosions

Edward Eskew, PhD

University of Connecticut, 2017

Due to unstable political climates across the world, the potential for terrorist attacks against civil infrastructure has become a serious concern. The increasing threat of explosions has fueled the need for research into methods to rapidly, and safely, assess the condition and safety of a structure from a blast. The ability to assess the structures safety from a potential blast with cumulative structural damage can be used to update security operations or retro-fit elements to improve resilience. In this work, structural health monitoring is used to determine the safety of structures before and the condition after a blast event, incorporating the actual structure with the real-world damage. As the methodology utilizes vibrational measurements, the gathered information is critical to the condition assessment. However, the number of monitoring sensors is usually significantly less than the number of potential monitoring degrees-of-freedom (DOF), and there is a significant potential for malfunctioning sensors due to the blast event. To quantify damage in a structure with damaged sensors, a two phase remaining stiffness localization and quantification method for limited measurements is presented. Two optimal sensor placement (OSP) methods are used to demonstrate the proposed two phase parameter localization and quantification method ability to quantify changes in a structure using a limited number of sensors. After an explosion has occurred, one of the key structural failures is a progressive collapse of the structure. To assess a structures probability of failure after an explosion, a method is developed which uses structural health monitoring (SHM) techniques to update a numerical model with vibration measurements to represent the damaged condition of a structure after a blast, and to assess probability of failure using the alternate path method. The included work can be utilized to assess structures safety from explosions, determining appropriate security procedures, and guiding safe emergency operations after the blast event.

Structural Health Monitoring of

Buildings for Safety Assessments Under Explosions

Edward Eskew

B.S., Clarkson University, 2012

A Dissertation

Submitted in Partial Fulfillment of the

Requirements for the Degree of

Doctor of Philosophy

at the

University of Connecticut

2017

Approval Page

Ph.D. Dissertation

Structural Health Monitoring of Buildings for Safety Assessments Under Explosions

Presented by

Edward Eskew

Major Advisor: _____

Prof. Shinae Jang

Associate Advisor: _____

Prof. Michael Accorsi

Associate Advisor: _____

Prof. Richard Christenson

Associate Advisor: _____

Prof. Jeongho Kim

Associate Advisor: _____

Prof. Wei Zhang

University of Connecticut

2017

Acknowledgements

I would like to thank my adviser, Dr. Jang for her guidance and the numerous opportunities she has helped me pursue over the past five years. This experience has meant the world to me, and I am incredibly thankful for your help throughout the way. Thanks to my associate advisers and committee members, without your guidance and advice throughout the years the research presented within would not have been possible. I am especially grateful to Dr. Accorsi, for his support of my research throughout my time at UConn. And thanks to the numerous faculty and staff at the University of Connecticut for pushing me and helping develop me as a researcher, academic, and person during my time here.

Thanks to my friends, colleagues, and fellow Smart Infrastructure Lab members for helping me through the good and the trying times. To my family, for dealing with my obsessive passion to pursue my research, and always being there to support me. And a special thanks to my girlfriend and part-time collaborator Dr. Kelly Bertolaccini, for helping me through the good, the bad, and the broken times.

I would also like to acknowledge the financial support of the Department of Education and Department of Homeland Security, without which none of this would have been possible.

I could not have finished this journey without all of you. Thank you all very much.

Table of Contents

LIST OF FIGURES

LIST OF TABLES

1. INTRODUCTION

Due to the rising threat of terrorism globally, as well as the potential for accidental incidents, there is an increased concern regarding the impact of explosions near a structure. An explosion is a rapid release of a very large amount of energy, causing a large increase in temperature and pressure, creating hot compressed gases which can expand in a shock wave [1]. A blast can cause damage to a structure; including windows breaking, connections or cladding failing, damage to the internal non-structural aspects and furniture of the building, major structural failure, and even progressive collapse of the building. A progressive collapse is a failure of a structure which is disproportionate to the damaging event, usually caused by the failure of a critical element with nearby elements not being able to sustain the added loads to support the element loss, leading to a large, global failure [2]. Currently design methods exist to create buildings able to resist progressive collapse, such as the alternate path method. However, these methods do not consider additional damage to adjacent members of the structure, which could influence its resistance to progressive collapse [3, 4]. Therefore, the progressive collapse design methods are unsuitable for safety assessments after a blast.

After a blast, it is important to be able to provide an assessment on the safety of the structure for emergency response and stakeholder decision making. Current methods of post-event analysis include using simplified models [5, 6], complex finite element (FE) models [7], and/or visual inspections [8]. Each of these methods has drawbacks for rapid condition assessments due to time, accuracy, and/or safety concerns. Simplified models require information about the blast event which may not be available, and may not account for the complexities of the blasts' interaction with the structure. Complex FE simulations also require detailed information regarding the explosion, and can take too long to complete to be of use for emergency operations. And visual inspections, in addition to exposing the inspectors to danger, can take a significant amount of time and be very expensive. This has led to interest in remote safety inspection methods for first responders, including presentations on the topic at the Stabilization of Buildings Workshop in 2009 [9] and the Monitoring and Sensing of Near-Collapse Buildings Workshop in 2010 [10].

Structural health monitoring (SHM) provides the tools for such an assessment. SHM allows for the development of experimentally updated models of the structure, using vibration measurements from the structure. Updating of the original, "undamaged", structural model can reflect damage, such as from the blast, or other parameter modifications. Updated models from structures with a high probability of a blast threat can be used to update security procedures to reflect changes in the structure from damage or operation changes. And, after a blast, the updated model with the structures current condition can be used to assess the structures potential for progressive collapse using the Alternate Path (AP) method from the Department of Defense's (DOD) Unified Facility Criteria (UFC) [11].

Model updating relies upon information from the measurements to formulate the updated structural model. However, in most monitoring applications, the number of available sensors is significantly less than the potential monitoring degrees-of-freedom (DOF) [12]. Optimal Sensor Placement (OSP) techniques, such as the Effective Independence (EI) and the Effective Independence Driving Point Residue (EI-DPR) methods automatically locate the available number of sensors to optimize different measurement parameters. While different OSP methods have been developed to generate sensor networks to optimize different measurement parameters, little work has been performed comparing the sensor networks produced by these methods for SHM damage assessments. Additionally, after an explosion, there is a high potential for the existence of damaged or malfunctioning sensors. This can be due to general sensor failure, or because of the blast event itself. Therefore, an effective post-blast rapid condition assessment needs to be able to utilize a limited number of measurements.

This dissertation covers developing methods to assess the safety or probability of failure of pre and post blast structures using SHM, accounting for the potential of a limited number of sensors, or malfunctioning sensors due to the blast. The capability of SHM to develop pre-event safety evaluations incorporating damage to the structure, which can be used to update security measures or plan structural retro-fits to resist explosions, is presented in Chapter 3. To account for the probability of damaged sensors from the blast event, a method to quantify the damage to a structure with incomplete measurements due to missing or damaged sensors is presented in chapter 4. Chapter 5 uses OSP to locate limited sensors to

perform the parameter quantification using the method described in Chapter 4, showing its capacity with limited sensors, and providing a comparative analysis of the effectiveness of sensor networks developed using the OSP methods for damage quantification. In chapter 6, a method to assess the probability of failure of a post-blast structure for progressive collapse using SHM is shown.

2. BACKGROUND

2.1. Explosions on Structures

Explosives are commonly utilized by terrorists due to their ease of acquisition and use. Some examples of terrorist bombings include the 2,000 lbs vehicle bomb which destroyed the Beirut US embassy on April 18, 1983. A 1,310 pound explosive was detonated in the underground parking garage of the World Trade Center's Tower One on February 23, 1993, creating a 100 ft wide crater through four sublevels of reinforced concrete. Timothy McVeigh detonated explosives with a TNT equivalency of approximately 4,000 lbs outside the Murrah Federal building in Oklahoma City on April 19, 1995, causing a progressive collapse to occur [13]. On August 5, 2003 a car bomb severely damaged a JW Marriott in central Jakarta, Indonesia [14]. Additionally there have been over 150 attacks on U.S. embassies outside of the U.S. since 1998 [15]. According to the National Counterterrorism Center, 27% of global terrorist attacks in 2005 and 2006 were primarily bombings, 29% in 2007 (4,543 incidents), and 32% in 2008 (4,131 incidents) [16-18].

The protection of structures from a terrorist attack can be briefly categorized into three methods: prevention planning, increasing structural resiliency, and accurate post-event analysis. Civil engineers typically deal with resiliency via structural design and post-event analysis by determining the building damage and assisting in planning future use of the structure post-attack. Two broad approaches to increase a buildings' resiliency to a blast include designing buildings to better resist explosive loads by strengthening critical components using rigid design, or disperse the blasts energy using ductile design. Post-event planning involves analyzing the damage caused by the attack, and determining future action including demolition, repair, and/or a resumption of normal operations.

An explosion is defined as a rapid release of a large amount of energy, causing a large increase in temperature and pressure, creating hot compressed gases [19]. These gases expand in a shock wave, which is a short duration pressure wave that moves through the medium of air (blast wave), water, or earth, bringing a sharp increase in pressure at the front of the wave and a gradual decreasing of pressure as the

wave passes [19]. Some of the key parameters of the blast profile are its peak pressure (P_{peak}), arrival time (t_A), blast duration time (t_d), and impulse (I) or area under the pressure curve, shown in below,

$$I = \int_{t_A}^{t_2} P dt \tag{2.1}$$

where t_2 is when the blast pressure returns to ambient, and P is the pressure from the blast wave. These parameters are related to the weight and standoff distance (R) of the explosive. An example of the pressure profile of an explosion is shown in Figure 2.1.

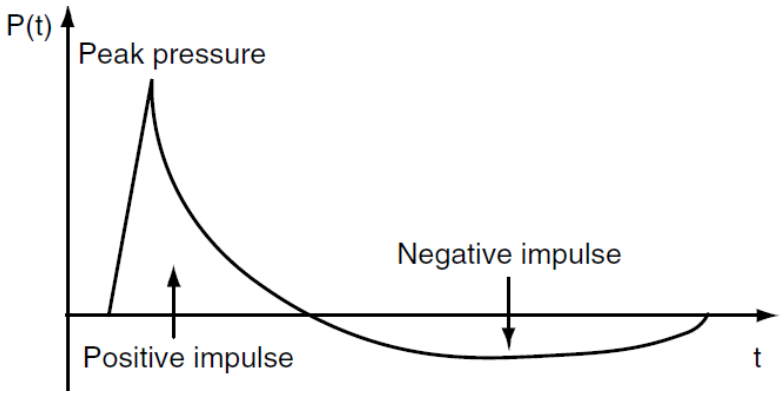

Figure 2.1 Example blast profile

Blasts can reflect off of solid surfaces, such as the ground or buildings, increasing the pressure in the shock wave based upon factors such as the type of impacting surface and the reflection angle between the pressure wave and the reflecting surface [14, 20, 21]. The increase in pressure can be calculated using numerical equations or design tables. Additional factors which can impact the pressure profile from a blast are increase due to confinement such as from being inside of a building, if the explosion is a surface or air blast, charge geometry, propagating medium, and other factors [21, 22].

An explosion can be classified based upon its Hopkinson-Cranz scaled distance (z), which is defined as follows,

$$Z = \frac{R}{W_{TNT}^{1/3}} \tag{2.2}$$

where R is the standoff distance, and W_{TNT} is the equivalent TNT weight of the explosive [14, 21, 22]. The scaled distance can be used to determine blast pressure parameters such as peak incident pressure, incident impulse, arrival time, duration time, and the reflected peak pressure and reflected impulse with the angle of impact. These blast parameters can be determined using empirical equations, design graphs such as shown in Figure 2.2, or from programs such as AT Blast [23]. The empirical pressure profiles are also built into programs such as Abaqus from the empirical CONWEP model.

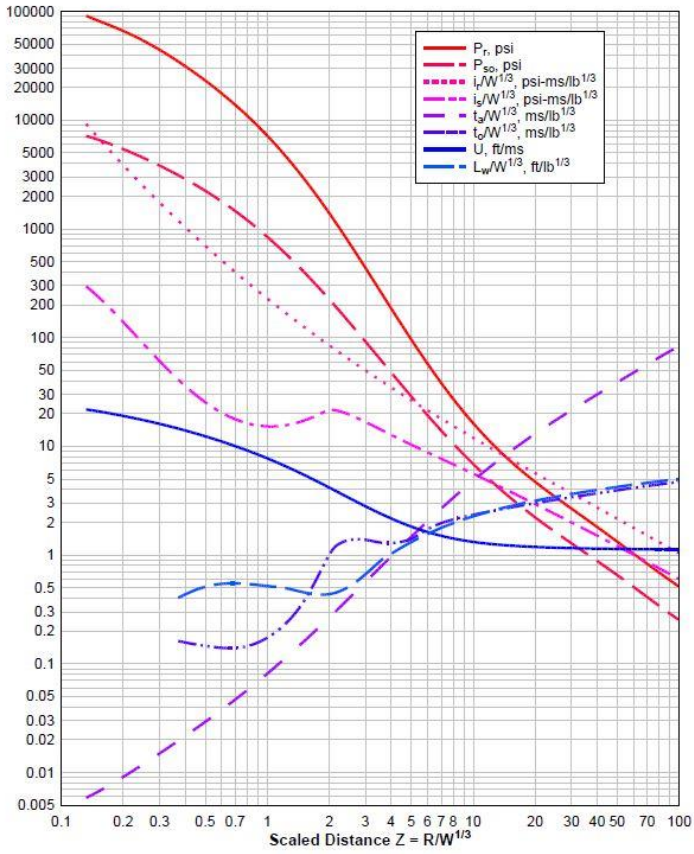

Figure 2.2 UFC 03-340-02 Positive phase shock parameters for a spherical TNT explosion in free air at sea level [24]

2.2. Analysis of Explosions on a Structure

Determining a structures response to an explosion is important for design and analysis purposes. There are different approaches to analytically determine the structural response, depending on the complexity of the structure, the required level of accuracy, the computational resources available, and acceptable computational costs [14]. Approximate methods can be used to quickly and cheaply assess the structural response to a blast. A form of approximate analysis for structural damage assessment is the use of a pressure-impulse (P-I) diagram. P-I diagrams are graphical limit states, such as found in ASCE 59-11 [25], which relate the structural damage limit states to blast peak pressure and impulse [14, 21]. These limit states are usually based upon design criteria or from empirical data. Blasts with parameters which fall to the left or under the P-I curve represent 'no damage' to the structure, while blasts to the right or above represent structural 'damage' scenarios, with the definition of damage corresponding to the limit state. P-I diagrams can also be used with additional limit states for a blast, such as injuries to people [21]. An example of a P-I diagram is shown in Figure 2.3. Examples of research involving P-I diagrams includes the work by Dragos *et al* who generated normalized P-I curves for UHPC slabs under large blasts [26]. Fallah *et al* developed a method to calculate dimensionless P-I diagrams for continuous beams, with varying load pulse shapes [27]. Li and Meng studied the impact of triangular, rectangular, and exponential pressure pulse profiles upon P-I diagrams, finding that the rectangular pulses generated the most conservative P-I diagrams, and exponential pulses generated the least conservative [28]. Shi, Li, and Hao looked into utilizing P-I diagrams and deriving initial conditions from the blast loading to account for errors due to damage in adjacent members and non-zero initial conditions in a structure subjected to a blast [29]. Ding *et al* studied the damage evolution of a steel tubular column subjected to a blast and post-blast fire, presenting pressure-impulse-exposure time limit curves [30].

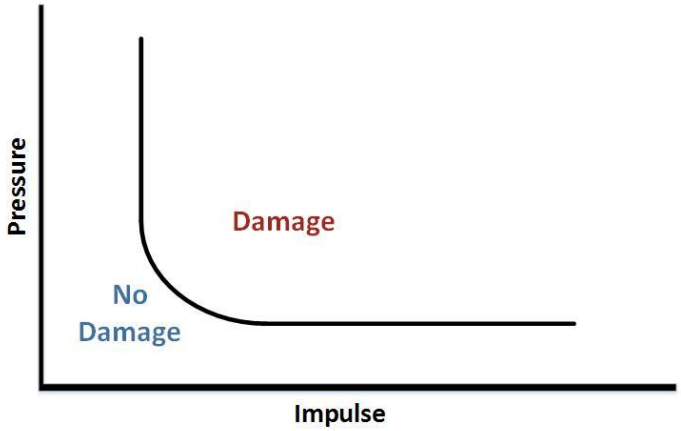

Figure 2.3 Pressure-Impulse (PI) diagram example

More detailed analyses can be performed using more complex numerical models. One of the key analytical decisions when designing a blast simulation is whether to use a coupled or uncoupled simulation. Uncoupled blast simulations are where the explosive pressure loads are modeled separately from the structural response, and applied to the structure as equivalent forces, saving significant computational costs [31]. Uncoupled analyses can be appropriate for non-complex geometries, where significant structure-blast interaction is not expected. Pape et al [1] reported that the structural response can be decoupled from the fluid dynamic analysis describing the blast pressure field, in situations where the structure does not deform significantly or moves slowly while the blast loading is present. Uncoupled analyses can be performed using models ranging in complexity from simplified static equivalent single degree-of-freedom (SDOF) models [5] to complex FE models. Equivalent models can be created by maintaining the energy in the structural response [21]. For uncoupled analyses, the blast pressure profile can be modified for analytical purposes into a simplified load, such as a triangular load, by maintaining its peak pressure and impulse, and modifying its duration [32]. Krauthammer et al described methodologies to generate pressure-impulse (P-I) diagrams, and studied the impact loading simplifications such as rise time, damping, ductility, and rectangular, triangular, and exponential equivalent loadings on the final P-I diagram [33]. Examples of uncoupled analyses include Islam and Yazdani's [34] use of simplified SDOF equivalent static loads to determine to study AASHTO girder bridges resistance to blast loads, and McConnell and Brown's [35] use

free-field blast pressures from the CONWEP program to determine failure standoff distances of steel columns.

A coupled analysis, which is typically performed using a coupled fluid dynamic (CFD) FE analysis, models the explosions pressure expansion within the model. The inclusion of the blast pressure expansion in the model allows for the incorporation of the structure-blast interaction in the analysis. This is important for the accurate modeling of the structural response of complex structural geometries, ground reflection, or other factors which render simplified analysis inadequate [31]. Some examples of coupled analyses include the work of Tang and Hao, who performed an analysis of bridge tower, pier, and deck to 1000 kg of TNT [36]. Son and Lee used coupled fluid dynamics models to simulate a car bomb on the deck of a cable-stay bridge with hollow steel box and concrete-filled composite pylons. They found that the concrete-filled pylons caused the structure to survive the blast, while the structure with hollow steel box pylons collapsed [37]. Lu and Wang used coupled numerical models to describe how global response is less significant for reinforced concrete than the local response for damage due to blasts, and how ground-vibrations play a negligible role in damage accumulation when compared to the air shock wave [31]. Additional discussion on the advantages and disadvantages of the different types of blast analyses can be found in Winget et al [38].

Indirect analyses are also used to measure the structural integrity of a structure after a blast. An indirect analysis involves removing or weakening structural elements, either numerical or experimentally, to simulate damage from a blast, and determining the effect on the structure [39]. This principle is utilized in the alternate path design method for progressive collapse resistance, and column loss experiments.

2.3. Progressive Collapse

Progressive collapse is the disproportionate global, or large scale, failure of a structure due to a local event. Potential causes of progressive collapse include vehicular impact, construction error, fires, accidental explosions, and bomb explosions [40]. European guidelines on progressive collapse prevention design can be found in the Euro-Norm EN 1991-1-7, while the U.S. uses different codes based upon U.K. standards from the Ronan Point apartment progressive collapse [14]. Three common methods of design to resist progressive collapse, found in the unified facilities criteria (UFC) 4-023-03, are the tie force method, the alternate path (AP) method, and the enhanced local resistance (ELR) method [11]. The choice of design methodology depends on the occupancy category of the building. The tie force method involves enhanced design of mechanical tie forces between structural members to increase continuity, ductility, and develop alternate load paths. The AP method involves simulating the removal of load carrying elements, and checking if the structure can still meet design standards to resist progressive collapse. The ELR method is used in addition to other progressive collapse design methods for certain building occupancy conditions, and is meant to guarantee a ductile failure in the event of a column or wall failure [39]. The ELR method designs key columns to ensure they reach their maximum flexural strength before failing in shear, to guarantee a ductile failure in the event of a column or wall failure [11, 41]. All of these methods are threat independent, meaning that they require no prior knowledge of the event which is causing the progressive collapse. Threat dependent methods also exist, which design the structure to resist a specific event or loading, such as the specific load resistance method [11].

One of the key design methods for progressive collapse is the AP method. In the AP method, critical elements are removed from the structural model, and an analysis is performed and response limits are checked. If the response limits are exceeded, then it indicates a high probability of progressive collapse in the event that the element fails, and the structure is re-designed. The AP method can be performed using a linear static, nonlinear static, or a nonlinear dynamic analysis. The linear static analysis utilizes conservative factors to account for nonlinear and dynamic behavior of the structure. A linear static analysis is beneficial due to its simplicity and low computational cost, but it does not accurately consider numerous factors of the analysis making it more suitable for initial design or simple structures. A nonlinear static analysis

involves a similar method to the linear static analysis, but with the addition of nonlinearity. This method offers the benefit of considering nonlinear behavior in the analysis; however the increased accuracy comes at the cost of increased complexity and computational resources. Nonlinear dynamic analysis involves a nonlinear time history analysis of the model with the removal of the element. To simulate the removal of the element, the model is built and equivalent element forces for the removed element are determined. The element is then removed and the equivalent force applied. The model is allowed to settle to equilibrium, and the equivalent element force is then removed. The nonlinear dynamic analysis can provide the most accurate results, as it includes dynamic behavior and material nonlinearity. However, it is also the most complex, requires the most computer resources, can be time consuming, and has the most potential for error due to modeling assumptions.

The differences between the linear static, nonlinear static, nonlinear dynamic, as well as the linear dynamic analysis, were studied by Marjanishvili and Agnew [42]. The authors found that the dynamic amplification factor of 2 was appropriate for linear static analyses, and the linear analysis evaluation criteria were unconservative compared to nonlinear analysis; with appropriate recommendations provided. McKay *et al* researched the dynamic and nonlinear increase factors used in the alternate path method, and found that they are overly conservative [43]. They proposed new methods for selecting the linear static load increase factor based upon m-factors, and nonlinear static dynamic increase factors based upon allowable and yield rotations. Kim and Kim studied the differences in the AP method as proposed by the GSA [44] and DOD [11], and found that the inclusion of lateral loads in the DOD guidelines made them more conservative [45].

Significant research has been performed on the progressive collapse potential of structures utilizing the AP method. Tsai and Lin used the AP method to study the strength of earthquake-resistant reinforced concrete (RC) buildings to resist progressive collapse [46]. They surmised that earthquake-resistant RC buildings have a low potential for progressive collapse. Hao and Tang continued their work on the damage to a large cable-stayed bridge subjected to progressive collapse from a blast by removing damaged components and determining if the structures would suffer progressive collapse [36, 47]. They then

determined the safe scaled distances to prevent progressive collapse of the bridge for the tower and pier, and determined that the bridge was unsusceptible to progressive collapse due to blasts on the main span. Sasani *et al* compared two models of the 11-story Crowne Plaza Hotel, using moment and fiber plastic hinges, for progressive collapse through element removal [48]. They found that the fiber plastic hinges produced larger peak moments and shears, with permanent deflections which were closer to the experimental results then using the moment hinges which overestimated the permanent deflection. Kazemi-Moghaddam and Sasani performed an analysis of the Murrah Federal building for the sudden removal of column G20, to simulate the bombing of the structure [49]. They show that the building would have resisted progressive collapse with only the removal of the column, stating that there must have been more severe damage than just the column removal. The progressive collapse of the Jiujiang bridge in 2007 due to a collision from a barge was modeled by Jiang *et al* [50].

2.4. Structural Health Monitoring

SHM is the use of measurements from a structure to detect changes which can be indicative of damage or other significant changes in the structure. Applications of SHM include dams, bridges, offshore installations, buildings and towers, nuclear installations, and tunnels [51]. There are four general levels of SHM methods, detection of the existence of damage, localization of the damage, quantification of the damage severity, and determining the remaining life of the damaged structure [52]. Different SHM methods use measurements in the time domain, frequency domain, or a combination of both. In the frequency domain, there are many different measurement features which can be utilized to determine a structures condition based upon dynamic measurements. These include natural frequencies, mode shapes, mode-shape curvature, dynamic flexibility matrix, residual force vector, modal strain energy, and the frequency response function (FRF) [52-55]. The frequency domain features can be directly analyzed for SHM purposes, such as with the residual flexibility matrix introduced by Pandey and Biswas [56]. The frequency features can

also be incorporated into localization and quantification methods which include model updating, neural networks, metaheuristic methods, or statistical pattern recognition [52, 57].

One type of SHM utilizes model updating to detect and/or quantify damage. Model updating is an inverse problem, where the experimental measurements are used to update an original FE model to better represent the actual structure being monitored. For damage detection and quantification, the updated model is then compared to the original, undamaged model of the structure. Direct model updating techniques utilize a single updating step to incorporate experimental measurements into the structural model. One method of direct model updating for damage detection is the residual stiffness method, which uses the dynamic flexibility matrix to update the stiffness matrix, and then compares the updated stiffness to the undamaged version to determine damage [58]. Yuen proposed the efficient model correction method which updates the mass and stiffness matrices, with easy incorporation of expanded mode shapes to account for unmeasured DOF [59, 60]. The efficient model correction method was then utilized by Wu and Loh for damage identification of a frame structure [61]. A review of some additional direct model updating techniques is presented by Visser [62]. However, while direct model updating methods are beneficial due to their ease of use, they do not enforce connectivity and physical meaning, or guarantee that the modified matrices will be positive definite [63, 64].

Another type of model updating, which can solve some of the problems associated with direct model updating, are iterative optimization methods. These methods involve optimization of parameters in the model, such as stiffness, elastic modulus, element area, or mass, based upon minimization of the difference between the updated analytical model and experimental results for a feature or a combination of features. Using measurements which capture the necessary features, from on the structure, the iterative optimization model updating methods can generate accurate models to represent the current condition of the damaged structure. Wang, Lin and Lim iteratively updated a numerical model using the error in the analytical FRF using a model sensitivity matrix to detect damage, validating their method on a numerical and experimental 3-bay plane frame structure [65]. Begambre and Laier used a modified particle swarm optimization algorithm to minimize the error in the FRF for damage detection [66]. Jaishi and Ren minimized multiple

objective functions based upon the modal strain energy and eigenfrequencies to identify damage in a numerical model of a simply supported concrete beam, and experimental testing of a precast box girder bridge [67]. Hao and Xia performed optimization with a genetic algorithm using an objective function based upon the eigenvalues and mode shapes of the model to detect damage in an experimental cantilever beam and a portal frame [68]. Friswell presented a discussion on damage updating parameters for generic elements, crack models, composite structures, and to account for distributed damage; as well as parameter subset selection [63].

In iterative minimization methods, it is important to ensure that the number of observations is greater than the number of updating parameters, otherwise the problem is underdetermined, and the ill-conditioned problem can produce an infinite number of solutions [69]. However, it is unlikely that there will be measurements from all of the structural DOF, due to the limited number of available sensors and sensors not being able to record measurements due to malfunctions or damage due to hazardous events. This can result in a significant loss of potential measurements, and present limited data sets for the model updating. In such a scenario, it is important to be able to assess the structural condition with only the limited measurements. Parameter subset selection can be used to identify the parameters of interest for optimization, and can be used to reduce the number of parameters needed for the analysis. This has been done using the sensitivity matrix of the parameters to the modal measurements [70, 71] and to the residual force vector [72]. Yun *et al* [73] employed a two-stage damage detection approach, where the damage was first localized by sensitivity to changes in the residual force vector, and then quantified using a genetic algorithm using an objective function based upon the normalized flexibility matrix variations. Shadan *et al* [74] used the optimization of the frequency response function from the due to changes in the sensitivity of the stiffness and mass matrices to update a numerical model of a truss bridge with limited measurements using the EI method for sensor placement. However, each of these techniques required a preliminary analysis to calculate sensitivity matrices of the structure.

A problem in model updating is accounting for limited measurements, due to a limited number of sensors being deployed, sensors malfunctioning and not providing measurements, or to limited modes

measured due to monitoring frequency bandwidth [71]. Interpolation techniques have been used to estimate the acceleration from missing sensors [75-77]. Many authors have utilized mode shape expansion to account for the incomplete modal information, which involves transforming mode shapes with missing measurements into complete mode shapes. Levine-West, Milman, and Kissil provide a comparison of different mode shape expansion techniques using experimental measurements [78]. Limongelli performed an analysis of the error of cubic spline interpolation schemes on acceleration measurements caused by seismic motion for 5, 10, and 20 story simulated frame structures [75]. Shrikhande used a 3rd order piecewise cubic Hermite polynomial interpolation method to interpolate the acceleration at unmeasured floors of a seven story simulated concrete building under earthquake loading [76]. O'Callahan and Li present a detailed analysis of the commonly used system equivalent reduction and expansion process (SEREP) modal expansion method [79]. SEREP expansion was used by Zhao and Zhang [80] to identify damage locations using the residual force vector on a numerical imply supported truss. Yun, Ogorzalek, Dyke, and Song used SEREP expansion to account for missing sensors, and used the residual force vector sensitivity matrix to locate the damage [72, 73]. They used this method to quantify multiple damage locations in numerical beams with and without noise [72], and to quantify the damage using a steady state genetic algorithm with the Frobenius norm of the flexibility matrix error as the objective function [73]. Shi, Law, and Zhang combined the incomplete mode shapes with their analytical counterparts [81]. They then used those mode shapes to identify damage, and iteratively updated the stiffness matrix of the damaged components using the natural frequency sensitivity matrix [81]. Link and Zimmerman used the orthogonal matching pursuit optimization method with a dynamically condensed model to compensate for limited measurements [82]. Theorizing that the first mode shape dictates behavior of a structure from an earthquake, Lin *et al* [83] updated a structural model after an earthquake using limited sensors by optimization of the measurements compared to the first mode shape, and used the updated model to determine the damage to the structure.

2.5. Optimal Sensor Placement

Measurements from a structure are a key component for SHM. Generally, with significantly fewer available sensors then potential monitoring DOF, sensor placement can be critical for a successful monitoring application. OSP are methods to locate a limited number of sensors to optimize the measurements. Many authors have developed and validated methods to optimize the location of sensors on a structure. One early method of OSP is the effective independence (EI) method. Developed by Kammer [84], the EI method iteratively removes sensors from all of the available monitoring locations to maximize the linear independence of the modal measurements from each sensor. To counteract issues involving sensor networks with low energy outputs, the EI-DPR method weights the EI method with the driving point residue (DPR), which provides a weight of the relative modal contribution at potential monitoring DOF [77, 85]. Li and Li proposed a weighting of the EI method using experimentally measured modal participation factors to incorporate excitation location into the OSP [86]. Chow *et al* developed a genetic algorithm to locate sensors by minimizing the information entropy in the sensor network [87]. They used their methodology to place sensors on a numerical model of a transmission tower, with experimental validation using a lab-scale transmission tower. An integer encoded multi-swarm particle swarm optimization was utilized by He *et al* [88] to locate tri-axial sensors on a numerical model of the Laxiwa arch dam. The authors compared the effectiveness of their OSP optimization using three different fitness functions, determining that a fitness function utilizing effective independence weighted with spatial correlation produced the better performance. Jalsan *et al* presented a methodology to locate wireless strain and acceleration sensors by finding the Pareto optimal solutions based upon minimizing the ratio of mode shape expansion to modal clarity index and the energy consumption through the wireless communication [89].

Some researchers have compared the sensor networks developed using multiple OSP methods. Rao and Anandakumar compared the sensor networks developed using different effective independence methods, energy based methods, the eigenvalue vector product method, the non-optimal driving point method, and the variance method using evaluations of the developed sensor networks [12]. The OSP methods were compared using numerical models of a cantilever beam, a microwave tower, a five-bay frame structure, a rectangular plate, and a bridge section. The authors concluded that the EI method consistently provided

better performance, based upon the total mean square error of the interpolated modes, the modal assurance criterion (MAC), and analyses of the Fisher information matrix. Papadopolous and Garcia used the singular value decomposition ratios and a model reduction frequency criterion to compare OSP methods [90]. They looked into OSP methods based upon kinetic energy, driving point residue, effective independence, singular value decomposition, model reduction, the Hankel matrix, and others. The methods were evaluated using a cantilever beam model and an experimental cantilever frame, with most of the methods yielding reasonable results. Li, Li, and Fritzen explored the connection between the EI and modal kinetic energy (MKE) methods, and showed how the EI method is an iterated version of the MKE method with re-orthonormalized mode shapes [91]. Meo and Zumpano compared sensor networks developed with the EI, EI-DPR, eigenvalue vector product, and non-optimal driving point residue using the mean square error of the interpolated mode shapes and the Fisher information determinant [85]. They performed their analysis using a model of the Nottingham Wilford suspension bridge, finding that the EI-DPR method produced better sensor networks than the other methods. The authors later expanded their work, comparing the previously stated methods with the kinetic energy method and a developed variance method using the mean square error of the interpolated mode shapes and the Fisher information determinant, with the EI-DPR method still providing the better performance [92]. Chang and Pakzad proposed an OSP method based upon modified variance, and compared the networks produced with the EI, EI-DPR, and MKE methods using interpolated modal assurance criterion (MAC) matrices for models of a simply supported beam, the Northampton street bridge, and the Golden Gate bridge [77]. These papers presented comparisons regarding the sensor networks developed by the differing OSP methods for different types of structures.

Some developed OSP techniques were used to locate a limited number of sensors for SHM applications. Shi *et al* proposed a method to locate sensors using the EI of the modal damage sensitivity matrix [93]. The sensor placement methodology was validated for damage detection using the multiple damage location assurance criterion method to localize the damage, with quantification performed using the sensitivity matrix to reduce frequency error on a numerical and experimental truss structure. The method accurately located the damaged elements on the numerical truss, with small errors in a noise free simulation

and increasing errors with the addition of noise; with only localization completed using the experimental measurements. Guo *et al* located sensors to minimize the information entropy from measurements of different potential ship collision locations, to detect damage to bridges from ship collisions [94]. Azarbayejani *et al* researched locating sensors using the weights from an artificial neural network trained to use features from a priori damage models to detect damage [95]. The authors demonstrated the method using a numerical model of a prestressed concrete bridge to locate sensors to monitor three locations for damage detection. Cheng *et al* located sensors to detect damage in a structure by maximizing the Fisher information matrix determinant of the modal flexibility sensitivity matrix [96]. The methodology was used to locate 15 sensors on a numerical model of a truss with 25 degrees-of-freedom (DOF) subjected to stiffness losses, with a particle swarm optimization used to quantify the stiffness reductions, producing errors under 5% for the quantification. Riveros-Jerez *et al* compared sensor networks developed with the EI and eigenvector sensitivity for damage detection using a Bayesian probabilistic method on numerical models of a 31 node three span beam, with seven and eleven sensors [97]. The authors determined that the eigenvector sensitivity method produced better performance for damage detection than the EI method.

3. PRELIMINARY DAMAGE BLAST SAFETY ASSESSMENTS

3.1. Introduction

P-I diagrams can show the limit states the structure or key structural elements to different types of blasts. The limit states typically relate to expected levels of damage to the structure. The P-I diagrams can be generated from empirical measurements, or from numerical models of the structure or element. The assessment of damage from different types of blasts can then be utilized by building stakeholders to make appropriate security and resiliency decisions to create an acceptable level of risk.

Over time, changes can occur to a structure. This can be due to reductions in elemental stiffness due to damage, or changing masses due to modified operations. Changes in the structure can change its resistance to an explosion, modifying the P-I limit states. This could require structural retrofits, or modifications in security procedure to maintain the same level of risk to the structure from a blast.

In this chapter, numerical model updating utilizing dynamic measurements from the structure is used to generate an updated structural model. The updated model incorporates the current condition of the structure, including damage to structural elements. Updated P-I diagrams, which reflect the structural safety including the impacts of damage, are generated using the updated numerical model. The updated P-I diagrams can be used to assess the current damage limit states, which can assist structural stakeholders in maintaining requisite levels of risk.

3.2. Methodology

The natural frequencies and mode shapes from a structure are functions of its stiffness and mass. If it is assumed that the mass of a structure remains relatively constant, then the changes in these dynamic properties are mainly due to changes in its stiffness. Utilizing these dynamic modal properties, it is therefore possible to determine an updated equivalent stiffness matrix of a damaged structure based upon dynamic

measurements. For a structure represented by a single degree-of-freedom (SDOF) model, the equivalent stiffness (K_E) can be calculated by as follows,

$$\boldsymbol{K_E = \omega^2 m} \tag{3.1}$$

Where ω is the experimentally determined natural frequency, and m is the mass. For a multiple degree-of-freedom (MDOF) model, the direct model updating method of Ewins and Sidhu [58] can be used, shown below,

$$\boldsymbol{K_E = K_{ru}\, F\, K_{ru}} \tag{3.2}$$

where $\boldsymbol{K_{ru}}$ is a condensed stiffness matrix from the undamaged numerical model, which can be calculated by static condensation of the global stiffness matrix from a detailed finite element model (FEM) [98], and $\boldsymbol{F}$ is the experimentally determined flexibility matrix. The experimentally determined modal flexibility matrix can be computed using the following equation [56, 99],

$$\boldsymbol{F = \Phi \begin{bmatrix} \ddots & & \\ & \frac{1}{\omega^2} & \\ & & \ddots \end{bmatrix} \Phi^T} \tag{3.3}$$

where $\boldsymbol{\Phi}$ is the mass-normalized modal matrix, and $\boldsymbol{\omega}$ are the natural frequencies, which can be determined from the vibrational measurements, in rad/sec.

To calculate the P-I diagram, simulations of the numerical structure with equivalent blast pressures are performed. The equivalent loading is simplified as a triangular pulse, with an impulse and peak pressure relating to the blast parameters. The blast parameters are then optimized to find where the structural response is equal to the design limits. The design limits used in this application are presented in ASCE's Blast Protection of Buildings [25] and Design of Blast-Resistant Buildings in Petrochemical Facilities [5].

The design limit states are low, medium, and high damage. The limit state displacement (X_L) for each damage severity is calculated based on the minimum inter-story displacement for buildings, determined from three different parameters: ductility ratio (μ), support rotation (θ), and building sidesway limit (Δ). Each limit displacement is defined such that,

$$X_{L,d} = \mu\, X_E \tag{3.4}$$

$$X_{L,r} = \tan(\theta)\, H \tag{3.5}$$

$$X_{L,s} = \Delta\, H \tag{3.6}$$

where, X_L is the inter-story displacement for the limit case, μ is the ductility ratio, X_E is the elastic displacement, θ is the support rotation limit, H is the story height, and Δ is the sidesway limit. The ductility ratio, support rotation, and sidesway limit values are presented in the design codes based upon building type and material properties. The final limit state displacement is then determined as the minimum of the displacements for each limit parameter, shown below,

$$X_L = \min(X_{L,d}, X_{L,r}, X_{L,s}) \tag{3.7}$$

For the low damage limit state, the building can be used for emergency operations with moderate repair costs exist. For medium damage, the building cannot be used for emergency operations and significant repair costs are likely. And for heavy damage, the building is at risk for collapse and the repair cost is likely to be similar to the replacement cost. These limit states are defined in Table 3.1.

Table 3.1 Limit state definitions

Damage severity	Description	Repair cost
Low	Building can be used	Moderate
Medium	Widespread damage building cannot be used	Significant
High	Building may collapse	Similar to replacement cost

To validate the updated P-I diagram procedure, an experimental modifiable steel frame building model was utilized. Testing was performed using the single story configuration shown in Figure 3.1, and the multi-story configuration shown in Figure 3.2. Damage was simulated by introducing thinner columns onto the structure, reducing the cross-sectional area of the elements and causing a corresponding reduction in the structural stiffness. Two types of damaged columns were used, shown in Figure 3.3, with the orange column reducing the diameter by 24.21%, and the red column reducing the diameter by 48.82%. The damage scenarios are shown in Table 3.2 for the single story configuration which corresponded to one orange column for damage 1, two orange columns for damage 2, and one red column for damage 3. The damage for the multi-story configuration is shown in Table 3.3, with pictures of the damage scenarios shown in Figure 3.4 (a)-(c). For the SDOF testing, an equivalent numerical model was used. For the multi-story configuration, a MDOF model was generated by condensing the SAP2000 model shown in Figure 3.5 into one horizontal direction per floor. The SAP2000 model used a fixed base, with steel shells for the plates and frames for the columns.

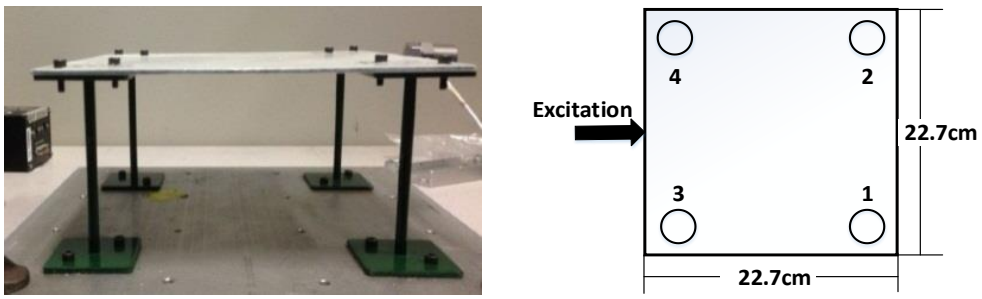

Figure 3.1 SDOF frame experimental set-up

Figure 3.2 MDOF frame experimental set-up

Table 3.2 SDOF model damage scenarios

Damage Scenarios	Radius Reduction(cm)	Area Reduction (cm^2)	Stiffness Reduction (N/m)	Damage Location
Undamaged	0	0	0	--
Damage 1	0.0781	0.0192	128910	1
Damage 2	0.1562	0.0766	257810	1,2
Damage 3	0.1575	0.0779	179190	1

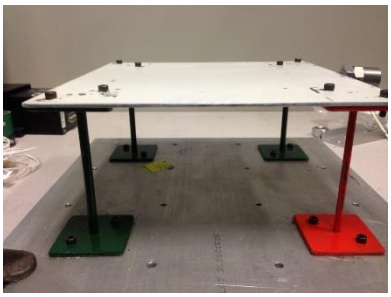

(a) Orange damage column

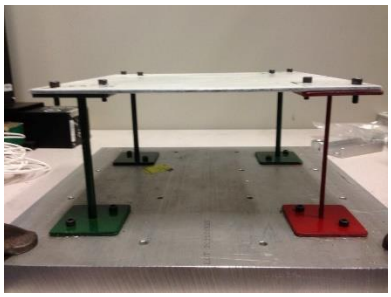

(c) Red damage column

Figure 3.3 Modifiable steel frame damage elements

Table 3.3 MDOF model damage scenarios

Damage scenario	Description
Undamaged	No damage
Damage 1	23% reduction in 1st floor
Damage 2	40% reduction in 1st Floor
Damage 3	33.5% reduction in 1st Floor 16.75% reduction in 2nd Floor

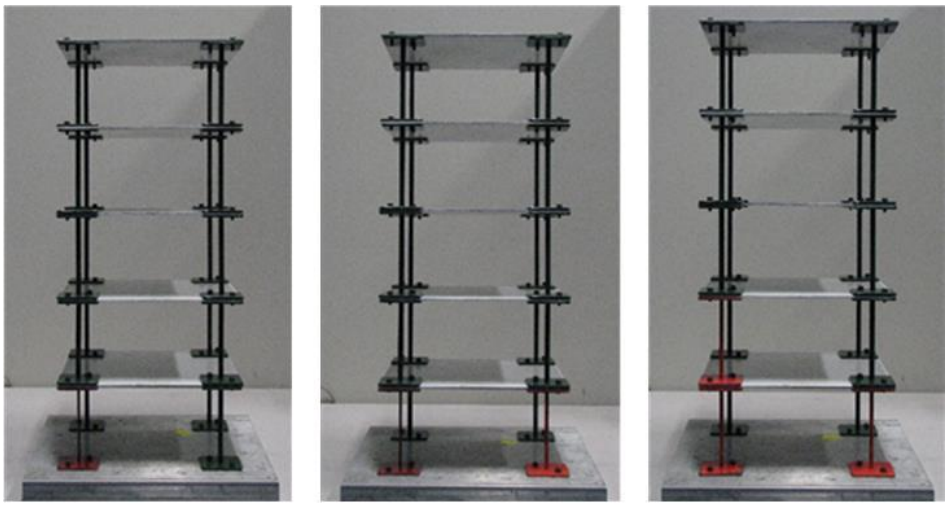

(a) Damage #1 (b) Damage #2 (c) Damage #3

Figure 3.4 MDOF frame damage scenarios

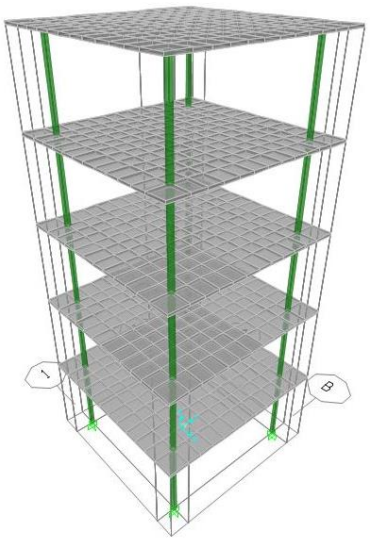

Figure 3.5 SAP2000 undamaged frame model

Vibrational measurements were gathered using one PCB 353B33 accelerometer on each floor to measure horizontal acceleration in the direction of excitation, with excitation provided as an impact force using a PCB 086C03 impact hammer. Measurements were collected using a sampling frequency of 1024 Hz with a uniform window. A sample time history from the undamaged five story model testing is shown in Figure 3.6, while the FRF, phase angle, and coherence function from the undamaged five story model testing are shown in Figure 3.7. A comparison of the natural frequencies from the SAP2000 model and from the experimental measurements from the multi-story configuration are shown in Figure 3.8. While there are some high errors in the 4^{th} and the 5^{th} modes due to the difficulty in modeling higher modes of vibration, the lower three modes agree very well; within 1% for modes 1 and 3, and 7% for the second mode. Therefore, it is assumed that the model is a reasonable representation of the actual structure. The experimental measurements were used to determine the natural frequencies and mode shapes from the frequency response functions (FRF), and experimental stiffness matrices were calculated. The experimental stiffness matrices were used to compute P-I diagrams for the undamaged and damaged scenarios.

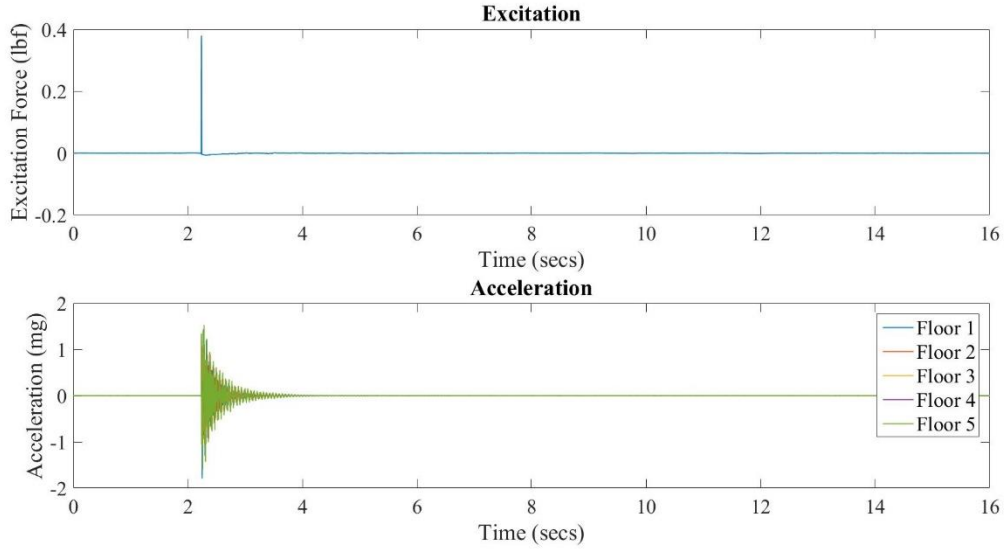

Figure 3.6 Undamaged structure time history

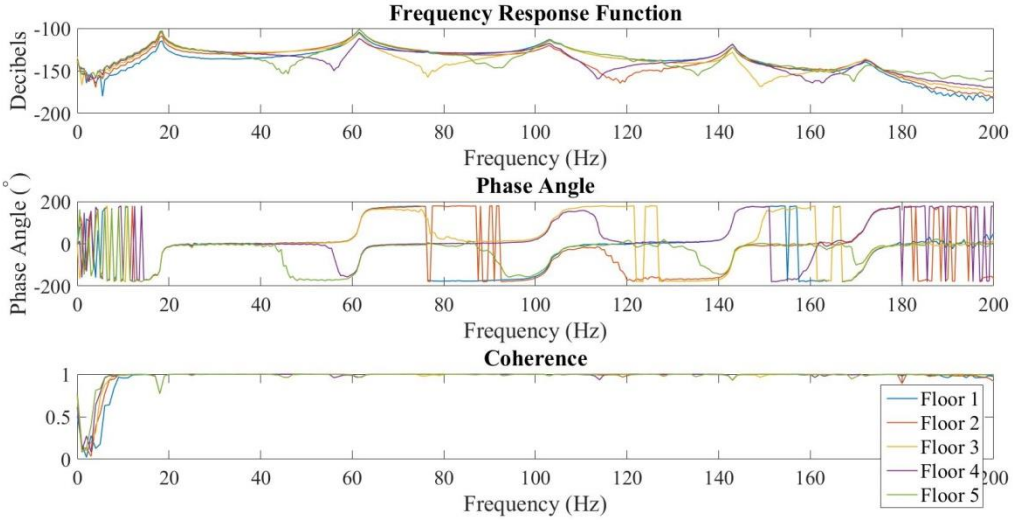

Figure 3.7 Undamaged structure frequency response function, phase angle, and coherence

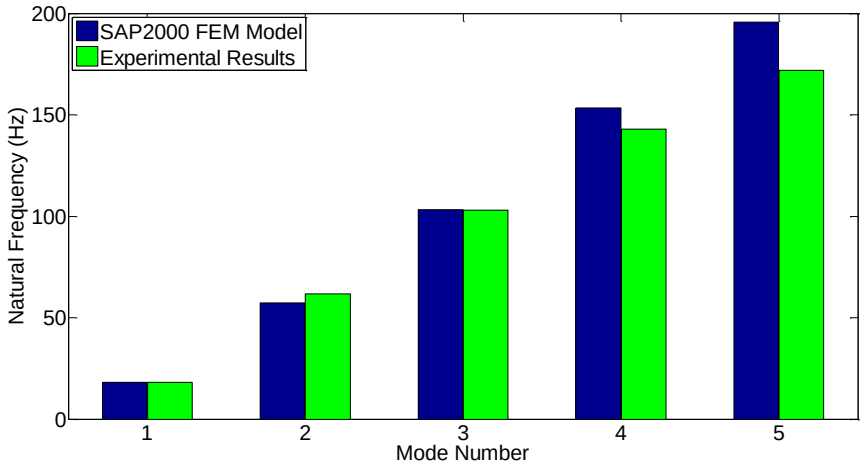

Figure 3.8 Natural frequency comparison between SAP2000 model and experiments

3.3. Results

To demonstrate the benefits of the updated P-I diagrams, P-I diagrams created from the undamaged numerical model were compared to the P-I diagrams created from the equivalent stiffness models for the undamaged and damaged experimental measurements. The P-I diagrams were calculated by minimizing the difference between the simulated maximum inter-story displacement from the equivalent blast loads on the numerical model and the limit state inter-story displacement. The numerical simulations were performed using a central difference method numerical simulation [98]. Due to the size of the structure, it was assumed that the blast's pressure profile was constant on each floor, and that the blast initiated at the same time on each floor. It was also assumed that the columns were not slender and only failed in flexure. Additional dead and live loads on the structure, uplift from the blast, and vertical blasts loads on the structure were neglected. The structural material only behaved elastically. The final P-I diagrams for the SDOF structure are shown in Figure 3.9. The P-I limit states using the original numerical model are represented with the solid blue (low damage), green (medium damage), and red (high damage) lines. And the P-I limit states from the experimentally updated models are represented with the dotted green (low damage), magenta (medium damage), and black (high damage) lines. From the comparisons between the SDOF original numerical and experimentally updated P-I diagrams, it can be seen that the experimentally updated P-I

diagram for the undamaged scenario closely matched the numerical P-I limit states, and that the addition of damage lowered the peak pressure and impulse required to achieve the damage limit states for damage scenarios 1-3. The decrease in limit states would represent a smaller or further away explosive causing the same damage as a closer or larger explosive as determined from the original model. Therefore, the updated model presents a more conservative estimate of the damage to the structure, by accounting for the preliminary damage.

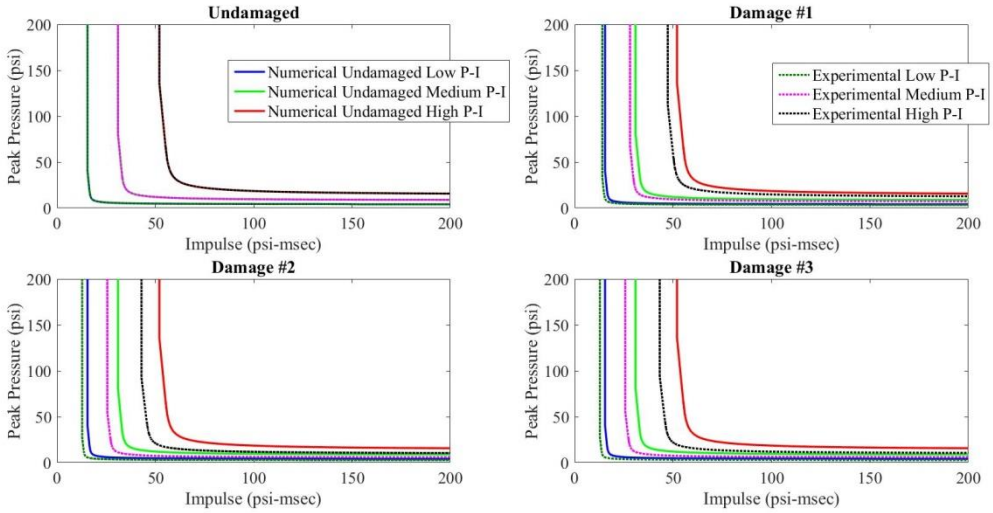

Figure 3.9 SDOF frame P-I diagrams

The P-I diagrams for the MDOF structure are shown in Figure 3.10. The P-I limit states are represented by the same lines as the SDOF P-I limits in Figure 3.9. The experimentally updated undamaged model was once again similar to the numerical original model, with a similar reduction in the P-I diagram limit states occurring with the updating of the model to account for the stiffness reductions for damage 1. However, for damage 2 and 3, the reduction in the peak pressure and impulse was less drastic, and for some blast parameters the experimentally updated P-I limit states exceeded the original numerical value. This is likely due to the discrepancies in the higher modes between the experimental measurements and numerical model. Additionally, the use of more accurate model updating with limited modes would likely be required to generate updated MDOF P-I diagrams.

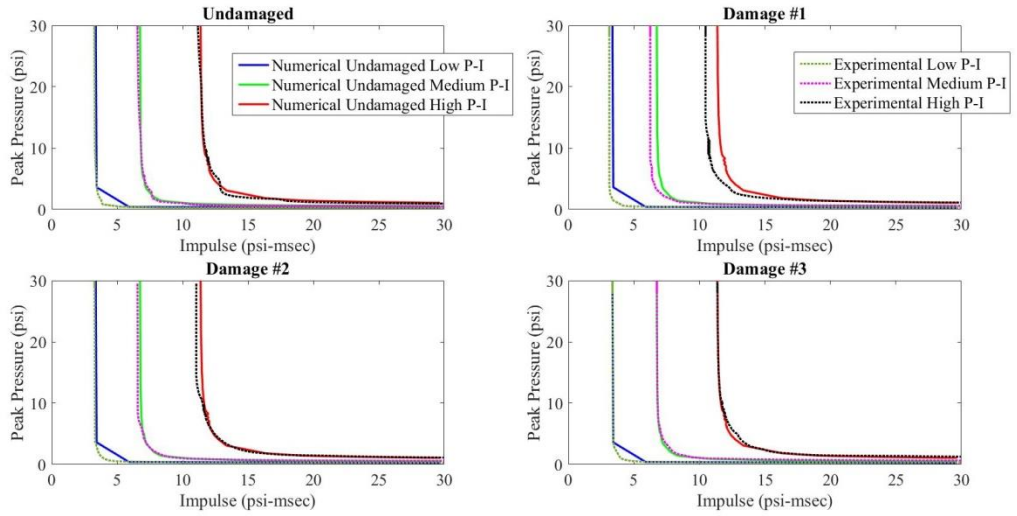

Figure 3.10 MDOF frame P-I diagrams

3.4. Conclusions

In this chapter, direct model updating using experimental measurements were utilized to generate P-I diagrams which incorporate preliminary damage to the structure. For the SDOF structure, the undamaged experimental model closely matched the numerical model, and the damaged models showed a decrease in limit states consistent with a less resistant structure. This information can be utilized by building stakeholders to increase security or resiliency to maintain the desired safety levels to certain explosive threats, or by emergency responders to have a more accurate estimate of the structures damage after an explosion. The MDOF structure showed accurate matching for the updated undamaged P-I diagram with the original model P-I diagram, and a decrease in resistance for the damage 1 P-I diagrams. However, there were unexpected increases in the P-I diagram for damage scenarios 2 and 3. These are likely due to issues with the model updating, due to the use of direct model updating methods. A more accurate model updating method for remaining stiffness quantification is addressed in Chapter 4.

4. DAMAGE ASSESSMENT USING INCOMPLETE MEASUREMENTS

4.1. Introduction

Structural health monitoring (SHM) involves determining the condition of a structure in regards to potential damage through the analysis of measurements from said structure. SHM has the potential to allow for the analysis of structures after hazardous events, such as blasts, earthquakes, impacts, etc. The measurements can be utilized to quickly determine the structures current condition, identifying if damage has occurred and its extent. This information can be of importance to emergency responders and building stakeholders. However, after an extreme event, there is the potential that some of the sensors on the structure may be not be able to record measurements, due to malfunctions or damage due to the extreme event. This can result in a significant loss of measurements, presenting incomplete data sets for the SHM damage assessment.

Direct model updating techniques involve updating models using one a single updating formula or series of formulas, based upon modal parameters such as natural frequencies and mode shapes. However, while direct model updating is beneficial in its ease of use, it does not ensure the connectivity and physical meaning of the model [64]. Another model updating technique, which can enforce the physical meaning of the model, involves optimization of parameters in the model, such as stiffness, young's modulus, or element area, based upon differences in the model and experimental modal parameters. Using a full set of measurements, from sensors at all relevant locations on the structure required to provide an accurate assessment of the structure, optimization model updating methods can provide accurate models to represent the current condition of the damaged structure. However, optimization model updating methods can have problems producing a unique solution if the problem is ill-condition, or the number of parameters is greater than the number of measurements. Such a scenario may occur due to the loss of sensors due to malfunctions or damage due to hazardous events.

This chapter will discuss a two-phase damage localization and quantification method which has been developed for damage assessment with incomplete measurements. In the first phase, direct model updating is employed to localize potential damage and identify a subset of potentially damaged parameters for optimization. In the second phase, the selected potentially damaged parameters are updated to match the incomplete experimental measurements. After damage quantification, the optimized model can be used to identify the severity of damage, and in further analysis assess the condition of the structure. The method presented in this chapter calculates the residual stiffness of a damaged structure with missing sensors, making it potentially beneficial for emergency response in hazardous situations, such as a building subjected to a blast. In the rest of the chapter, the discussed methodology will be presented, and validation provided using an ASCE benchmark numerical model and experimental testing of a modifiable 5-story steel building frame structure.

4.2. Methodology

The proposed technique utilizes a two-phase approach. In the first phase, potential damage parameters are localized through the use of direct model updating with augmented modal information. In the second the phase, iterative optimization of the subset of potential damage locations occurs, to quantify the damage in the structure. In this example, the localization was performed using the efficient model correction (EMC) technique, with constrained least-square optimization used for the quantification.

Efficient Model Correction

The EMC method builds a transformation matrix ($\boldsymbol{R}$) using measurements from the structure and an analytical undamaged model [60, 61], which is defined such that:

$$\boldsymbol{R} = \boldsymbol{\Phi_D}{\boldsymbol{\Phi_A}}^{-1} \tag{4.1}$$

where $\boldsymbol{\Phi_D}$ is the complete mass-normalized mode shape from the experimental, potentially damaged, structure, and $\boldsymbol{\Phi_A}$ is the mass-normalized mode shape from the analytical, undamaged, model. To compensate for missing measurements and limited modal measurements, components of the modal matrix which are not recorded are replaced by their analytical values, defined as:

$$\boldsymbol{\Phi}_D = \sum_{i=1}^{m}\sum_{j=1}^{n} \boldsymbol{\phi}_{E,i,j} + \sum_{i=m+1}^{M}\sum_{j=n+1}^{N} \boldsymbol{\phi}_{A,i,j} \tag{4.2}$$

where m is the number of measured modes, M is the number of modes in the full matrix, n is the number of measured DOF, N is the full number of DOF, $\boldsymbol{\phi}_E$ are the experimental mode shapes, and $\boldsymbol{\phi}_A$ are the analytical mode shapes.

The transformation matrix is then used to create a modified stiffness ($\boldsymbol{K}^*$), mass ($\boldsymbol{M}^*$), and modal matrix ($\boldsymbol{\Phi}^*$) using the equations:

$$\boldsymbol{K}^* = \left(\boldsymbol{R^{-1}}\right)^{\boldsymbol{T}} \boldsymbol{K_A R^{-1}} \tag{4.3}$$

$$\boldsymbol{M}^* = \left(\boldsymbol{R^{-1}}\right)^{\boldsymbol{T}} \boldsymbol{M_A R^{-1}} \tag{4.4}$$

$$\boldsymbol{\Phi}^* = \boldsymbol{R\Phi_A} \tag{4.5}$$

where $\boldsymbol{K_A}$ is the analytical stiffness matrix, and $\boldsymbol{M_A}$ is the analytical mass matrix. The updated, experimental stiffness matrix ($\boldsymbol{K_E}$) is then computed as,

$$\boldsymbol{K}_E = \boldsymbol{K}^* + \boldsymbol{M}^*\left[\sum_{\boldsymbol{i=1}}^{M}\left(\boldsymbol{\omega}_{E,i}{}^2 - \boldsymbol{\omega}_{A,i}{}^2\right)\boldsymbol{\Phi}^*{}_{\boldsymbol{i}}\boldsymbol{\Phi}^*{}_{\boldsymbol{i}}{}^{\boldsymbol{T}}\right]\boldsymbol{M}^* \tag{4.6}$$

where $\boldsymbol{\omega_E}$ are the experimentally measured natural frequencies, and $\boldsymbol{\omega_A}$ are the analytical natural frequencies. For the measured natural frequencies, values corresponding to unmeasured modes are replaced with the analytical values.

Least Squares Optimization

Least-squares optimization was utilized to modify the parameters within the numerical model to minimize the error in an objective function, creating a numerical model which better represented the monitored structure. This chapter utilized the minimization of a multi-objective function using the mode shape and natural frequency differences. The complete objective function is calculated as follows,

$$\mathbf{min}\ \mathbf{J}(\boldsymbol{\theta}) = \boldsymbol{W_1 J_1}(\boldsymbol{\theta}) + \boldsymbol{W_2 J_2}(\boldsymbol{\theta}) \tag{4.7}$$

where θ are the optimization parameters, W_1 and W_2 are weighting values, J_1 is the objective function for the mode shapes, and J_2 is the objective function for the natural frequencies. For this example, the optimization parameters are reductions in the stiffness of elements, such that

$$\boldsymbol{k_{D,i} = k_{A,i}\theta_i} \tag{4.8}$$

where $k_{D,I}$ is the ith elemental stiffness for the damaged model, and $k_{A,I}$ is the ith elemental stiffness for the analytical model. The updating parameters are bounded, such that $0 \leq \theta \leq 1$. The mode shape objective function utilizes the coordinate modal assurance criterion (COMAC), shown below,

$$\boldsymbol{J_1} = \sum_{\boldsymbol{i=1}}^{\boldsymbol{m}} (\boldsymbol{COMAC_i - 1})^{\boldsymbol{2}} \tag{4.9}$$

$$\boldsymbol{COMAC_i} = \frac{\left(\sum_{j=1}^{n} \boldsymbol{\phi_{E,ij}^T \phi_{\theta,ij}}\right)^2}{\left(\sum_{j}^{N} \boldsymbol{\phi_{E,ij}^T \phi_{E,ij}}\right)\left(\sum_{j}^{N} \boldsymbol{\phi_{\theta,ij}^T \phi_{\theta,ij}}\right)} \tag{4.10}$$

where ϕ_θ is the updated models mode shapes. And the second objective function is,

$$\boldsymbol{J_2} = \sum_{i=1}^{m} \left(\frac{\boldsymbol{\omega_{\theta,i}}}{\boldsymbol{\omega_{E,i}}} - \mathbf{1}\right)^2 \tag{4.11}$$

where ω_θ is the updated models natural frequencies. The objective function minimization was performed in MATLAB 2013a using the constrained multivariable derivative free minimization function, *fmincon*.

Remaining Stiffness Evaluation with Incomplete Measurements

Missing sensors on a structure presents problems with implementing iterative optimization or direct model updating. For optimization problems with more updating parameters then measurements, it may not be possible to accurately update the model due to the optimization problem being ill-conditioned, and increased updating parameters may lead to increased computational costs. Direct model updating equations cannot guarantee the physical connectivity of the model, and would require the use of expanded models. While the expanded models present full modal information, they introduce potential errors from the expansion process into the updating procedure which makes them ill-suited for damage quantification. To solve these issues, parameter subset selection utilizing direct model updating was used to select a reduced number of updating parameters. Then, least squares optimization was performed on the selected parameter subset to determine the updated structural model, with the remaining stiffness quantification.

The efficient model correction updating technique was used as the direct model updating method for the damage localization and parameter selection. Limited modal parameters from the measurements were utilized in the localization. The modal properties were calculated using the N4SID (numerical algorithms for state space system identification) procedure, with the excitation force and acceleration responses [100, 101]. The N4SID algorithm is able to accurately identify the natural frequencies and mode shapes from the

measurements, and is a built-in function in the MATLAB system identification toolbox. The number of mode shapes used in the localization were determined by the modal participation mass ratio (α),

$$\boldsymbol{\alpha} = \frac{(\boldsymbol{\phi}_{A,i}^{T} M_A \boldsymbol{D})^2}{\boldsymbol{D}^T M_A \boldsymbol{D}} \tag{4.12}$$

where D is a vector of the excitation influence [102]. When the sum of the modal participation mass ratio exceeded a threshold, then those p modes were used for the damage localization. In this work, the threshold is set at approximately 90% participation. For the unmeasured DOF due to missing sensors, the mode shapes at said DOF were assumed to be from the undamaged model. This will create errors in the localization at those DOF, however all DOF with missing measurements will be assumed to be updating parameters, minimizing the errors influence on the localization. The limited modal matrix $\boldsymbol{\phi}_{1:p}$, and the augmented modal matrix $\boldsymbol{\Phi_D}$ are expressed as:

$$\boldsymbol{\phi}_{\mathbf{1:p}} = \begin{Bmatrix} \boldsymbol{\phi}_{\mathbf{1:p},E_{1:n}} \\ \boldsymbol{\phi}_{\mathbf{1:p},A_{n+1:N}} \end{Bmatrix} \tag{4.13}$$

$$\boldsymbol{\Phi}_D = [\boldsymbol{\phi}_{\mathbf{1:}p} \quad \boldsymbol{\phi}_{p:M}] \tag{4.14}$$

After the damaged stiffness matrix is calculated ($\boldsymbol{K_D}$), it is compared to the analytical stiffness matrix to determine damage locations by determining the percent difference of the diagonal terms of the damaged stiffness matrix to the diagonal terms of the analytical stiffness matrix,

$$\Delta \boldsymbol{k_i} = (\frac{\boldsymbol{k_{D,ij}} - \boldsymbol{k_{A,ij}}}{\boldsymbol{k_{A,ij}}})\mathbf{100}\% \tag{4.15}$$

where i is equal to j, and Δk is a vector of the difference between the diagonal damaged and analytical stiffness matrices. The floor analytical bending stiffness for a frame structure with circular columns can be computed as follows,

$$k_i = \sum_{j=1}^{C} \frac{12E(\frac{\pi r^4}{4})}{H^3} \tag{4.16}$$

where k is the i^{th} floor stiffness, C is the number of columns per floor, E is the Young's modulus, r is the column radius, and H is the height of the column.

If the stiffness difference is less than a threshold value, then the stiffness at that DOF is identified as an optimization parameter. In addition, all missing sensor locations are identified as optimization parameters. The final selection of damage parameters is then used in the least-squares optimization to determine the final updated stiffness matrix for the damaged structure.

4.3. Numerical Validation

To demonstrate the proposed damage assessment methodology for incomplete measurements, the analytical MATLAB model presented by Johnson *et al* [103] of the Phase I IASCE-ASCE Structural Health Monitoring Benchmark Problem, stored in the NEEShub database, was employed. The researchers used the 12DOF stick frame model, shown in Figure 4.1, where the first three stiffness terms per floor (k) relate to the x translation stiffness, y translation stiffness, and rotation around the z-axis respectively.

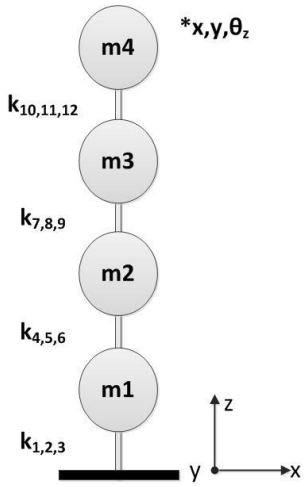

Figure 4.1 IASCE-ASCE SHM benchmark problem numerical model

The model uses three global DOF for each floor: two translations (x, y) and one rotation (θ_z). Two damage conditions were considered: (1) damage on the 1st floor, and (2) damage on the 1st and 3rd floors. In addition, the undamaged model was analyzed, as damage scenario zero, to provide a baseline for the estimation. Excitation was simulated as band-limited white noise on all floors in both translational DOFs, with acceleration measurements simulated in the two translational DOF (x, y). No noise was added to the numerical measurements. The 12 natural frequencies from the undamaged and damaged models are presented in Table 4.1.

Table 4.1 IASCE-ASCE SHM benchmark model natural frequencies

Mode	Undamaged (Hz)	Damage #1 (Hz)	Damage #2 (Hz)
Y-translation 1	9.41	6.24	5.83
X-translation 1	11.79	9.91	9.51
Torsion 1	16.38	11.73	11.01
Y-translation 2	25.54	21.53	14.89
X-translation 2	32.01	28.92	24.91
Torsion 2	44.64	38.28	28.41
Y-translation 3	38.66	37.37	36.06
X-translation 3	48.44	47.34	46.79
Torsion 3	67.48	65.31	63.64
Y-translation 4	48.01	47.83	41.35
X-translation 4	60.15	59.99	54.34
Torsion 4	83.62	83.31	72.61

The two phase remaining stiffness estimation with incomplete measurements method was analyzed using the three structural conditions by assuming the first floor sensors were damaged, and therefore excluded from the analysis. A threshold of -0.1% was used for the parameter subset selection, and the optimization weights from equation 4.7 were set at $W_1 = W_2 = 1$. These were valid values due to the lack of noise in the measurements. As the sum of the modal participation ratio of the first mode in the x and y DOFs summed to 89%, the first mode was accepted as providing enough information for the analysis. In the results, the estimated remaining stiffness and the actual remaining stiffness are presented, as well as if the DOF was identified as a potentially damaged DOF for the remaining stiffness optimization. DOF which were selected as optimization parameters (Θ) for the remaining stiffness optimization procedure are noted with a check mark (✓).

Table 4.2 shows the remaining stiffness for the undamaged scenario. The damage localization identified the two DOF at the first floor with the missing sensors and the adjacent second floor DOF as potential damage locations. Optimization using the selected damage parameters lead to an accurate

assessment of zero damage for all parameters, and therefore 100% remaining stiffness for all updated DOF. This is an accurate assessment, as there was no damage in the model.

Table 4.2 Remaining stiffness evaluation for undamaged scenario

Undamaged				
DOF	*Θ*	*Calculated Remaining Stiffness Ratio (%)*	*Actual Remaining Stiffness Ratio (%)*	*Error (%)*
1st Floor X	✓	100	100	0.00%
1st Floor Y	✓	100	100	0.00%
2nd Floor X	✓	100	100	0.00%
2nd Floor Y	✓	100	100	0.00%
3rd Floor X	-	100	100	0.00%
3rd Floor Y	-	100	100	0.00%
4th Floor X	-	100	100	0.00%
4th Floor Y	-	100	100	0.00%

Table 4.3 shows the results for damage scenario 1, with damage on the first floor. The damage localization identified the two DOF at the first floor with the missing sensors and the adjacent second floor DOF. Optimization using those four stiffness parameters lead to an accurate assessment of 28.97% remaining stiffness on the first floor y direction and 54.76% remaining stiffness for the first floor x direction, which is the same as the remaining stiffness from the model.

Table 4.3 Remaining stiffness evaluation for damage #1

Damage #1				
DOF	*Θ*	*Calculated Remaining Stiffness Ratio (%)*	*Actual Remaining Stiffness Ratio (%)*	*Error (%)*
1st Floor X	✓	54.7558	54.7561	0.00%
1st Floor Y	✓	28.973	28.9732	0.00%
2nd Floor X	✓	100	100	0.00%
2nd Floor Y	✓	100	100	0.00%
3rd Floor X	-	100	100	0.00%
3rd Floor Y	-	100	100	0.00%
4th Floor X	-	100	100	0.00%
4th Floor Y	-	100	100	0.00%

Table 4.4 shows the results for damage scenario 2, with damage on the first and third floor. The damage localization identified the two DOF at the first floor with the missing sensors and the damaged third floor DOF. Optimization using those four stiffness parameters leads to an accurate assessment of 28.97% remaining stiffness on the first and third floor y direction, 54.76% remaining stiffness for the first and third floor x direction, which is the same as the remaining stiffness from the model.

Table 4.4 Remaining stiffness evaluation for damage #2

Damage in #2				
DOF	*Θ*	*Calculated Remaining Stiffness Ratio (%)*	*Actual Stiffness Remaining (%)*	*Error (%)*
1st Floor X	✓	54.7561	54.7561	0.00%
1st Floor Y	✓	28.9732	28.9732	0.00%
2nd Floor X	-	100	100	0.00%
2nd Floor Y	-	100	100	0.00%
3rd Floor X	✓	54.7561	54.7561	0.00%
3rd Floor Y	✓	28.9732	28.9732	0.00%
4th Floor X	-	100	100	0.00%
4th Floor Y	-	100	100	0.00%

For all of the scenarios presented, the parameter selection methodology either perfectly selected the damage locations, or added additional potential damage locations next to the missing sensors, likely due to the influence of the assumed undamaged analytical values on the assessment. The optimization based upon the limited parameters was then able to accurately quantify the damage.

4.4. Experimental Validation

To further validate the damage quantification with limited sensors, the 5-story steel frame structure, shown in Figure 4.2, was utilized. Each floor has a height of 10.2 cm, and is supported by four columns which are

connected to the floor using two screws. Damage was simulated on the frame by replacing the original columns with columns of a thinner radius. Three damage scenarios were used, with the estimated stiffness reductions outlined in Table 4.5. The stiffness reductions were estimated as a percent reduction from the undamaged columns using the floor stiffness calculated from equation 4.16, with a Young's modulus of $200e^9$ N/m^2. Numerical models of the damaged frames are shown in Figure 4.3, where the undamaged green columns have a radius of 0.3226 cm, the orange columns have a radius of 0.2445 cm, and the red columns have a radius of 0.1651 cm. Impact hammer testing was performed to gather the measurements from the system. A PCB 086C03 impact hammer and PCB 353B33 accelerometers were utilized in the experiments. Sixteen seconds of measurements were recorded at 1024 Hz using a uniform window. A representative time history and frequency response function (FRF) from the undamaged experimental testing are shown in Figure 4.4. Further details regarding the experimental testing can be found in Eskew and Jang [104].

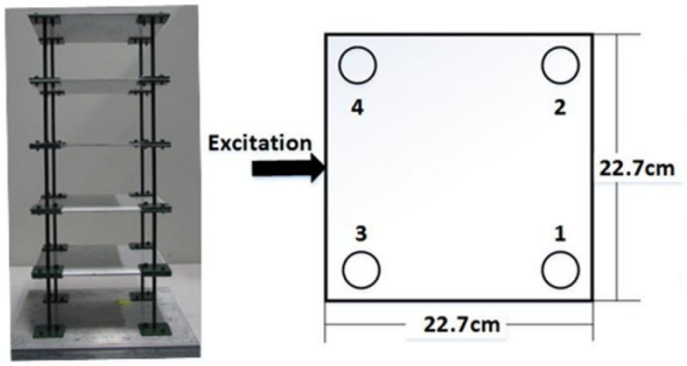

Figure 4.2 Modifiable steel frame image and cross section

Table 4.5 Estimated experimental stiffness reductions

Damage scenario	Description
Undamaged	No damage
Damage 1	23% reduction in 1st floor
Damage 2	40% reduction in 1st Floor
Damage 3	33.5% reduction in 1st Floor 16.75% reduction in 2nd Floor

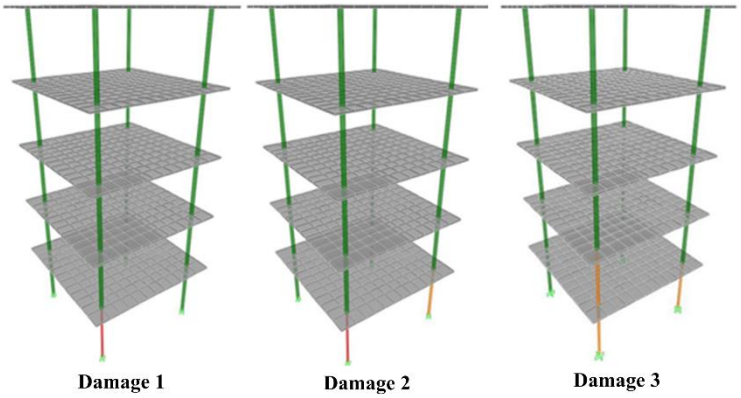

Figure 4.3 Modifiable steel frame damage scenarios

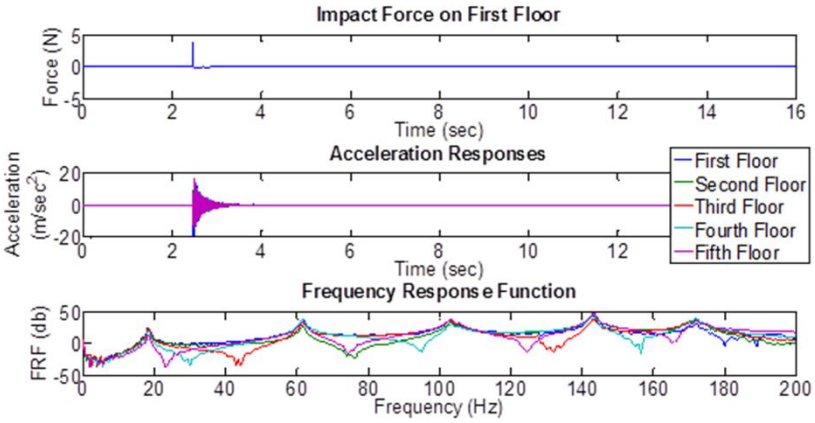

Figure 4.4 Undamaged experimental measurements

A FEM of the undamaged structure was developed in SAP2000, and utilized for the analytical stiffness. The FEM model is shown in Figure 4.5. The mass matrix was calculated by lumping of the applicable masses from the experiment. The analytical mode shapes and natural frequencies were calculated from the FEM stiffness matrix, updated using the experimental results, and the mass matrix.

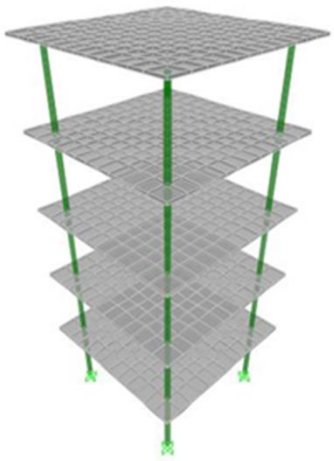

Figure 4.5 SAP2000 modifiable steel frame model

A shear model of the frame structure was generated, and used as the analytical model for the parameter updating. A threshold of 0% was used for the parameter selection, and the optimization weights from equation 4.7 were set at W_1 = 10 and W_2 = 1 [105]. The threshold of 0% meant any reduction would be considered damage, which is slightly more conservative to account for noise in the measurements. And the objective function weights are based upon the general assumption that mode shapes have approximately a 10 times greater impact from noise then natural frequencies. Due to the limited modal participation mass ratios from the impact hammer testing, the first four modes were used in the localization, resulting in a summed modal participation ratio of 92%. For the analysis, the sensor on the first floor was assumed to be damaged, and therefore the measurements from the first floor were removed. The calculated remaining stiffness using the remaining stiffness estimation with incomplete measurements technique and the estimated remaining stiffness for damage scenario number one are presented in Table 4.6. The damage localization identified the first floor with the missing sensor and the adjacent second floor as having

potential damage. The quantification using the limited parameters was then able to identify the second floor as having no damage, and the first floor's remaining stiffness as 76.15% of the undamaged stiffness, which is approximately 1% below the estimated value.

Table 4.6 Remaining stiffness evaluation for damage 1

Damage 1				
DOF	*θ*	*Calculated Remaining Stiffness Ratio (%)*	*Estimated Remaining Stiffness Ratio (%)*	*Error (%)*
1st Floor	✓	76.15	77	-1.10%
2nd Floor	✓	100.00	100	0.00%
3rd Floor	-	100.00	100	0.00%
4th Floor	-	100.00	100	0.00%
5th Floor	-	100.00	100	0.00%

Table 4.7 shows the remaining stiffness for damage scenario number two. The damage localization identified the first floor with the missing sensor and the adjacent second floor as having potential damage. The quantification using the limited parameters was then able to identify the second floor as having approximately 97% remaining stiffness, which is about 3% lower than estimated, and the first floor as having about 59% remaining stiffness, which is approximately 1% below the estimated value. As the addition of damage required removing screws which held the column of note as well as columns on adjacent floors, minor damage to adjacent floors may be due to changes induced during the column modification.

Table 4.7 Remaining stiffness evaluation for damage 2

Damage 2				
DOF	*θ*	*Calculated Remaining Stiffness Ratio (%)*	*Estimated Remaining Stiffness Ratio (%)*	*Error (%)*
1st Floor	✓	59.39	60	-1.01%
2nd Floor	✓	97.27	100	-2.73%
3rd Floor	-	100.00	100	0.00%
4th Floor	-	100.00	100	0.00%
5th Floor	-	100.00	100	0.00%

Table 4.8 shows the remaining stiffness for damage scenario number three. The damage localization identified the first floor with the missing sensor and the second floor as having potential damage. The quantification using the limited parameters was then able to identify the second floor as having approximately 89% remaining stiffness, which is about 7% higher than estimated, and the first floor as having about 67% remaining stiffness, which is approximately 0.4% below the estimated value. While the 7% error is larger than expected, with the accurate assessment of the first floor and the potential variations between the estimated and actual reductions, the assessment presents credible results.

Table 4.8 Remaining stiffness evaluation for damage 3

Damage 3

DOF	*Θ*	*Calculated Remaining Stiffness Ratio (%)*	*Estimated Remaining Stiffness Ratio (%)*	*Error (%)*
1st Floor	✓	66.74	66.5	0.37%
2nd Floor	✓	89.05	83.25	6.97%
3rd Floor	-	100	100	0.00%
4th Floor	-	100.00	100	0.00%
5th Floor	-	100.00	100	0.00%

For the first and second damage scenarios, the methodology was able to accurately identify the damage location and quantify its severity. For the third scenario, the damage location was accurately identified, and the remaining stiffness was accurately quantified for the first floor, with slight errors in the second floor quantification. As the results come from experimental measurements, this could be due to the second floor being stiffer than anticipated or experimental noise. In addition, the optimization utilized a shear model, while the structure was 3-dimensional, potentially introducing additional error into the updating. However, the experimental results using the remaining stiffness evaluation with incomplete measurements still can be said to have produced a highly accurate assessment, showing its potential applicability.

4.5. Conclusions

Damage identification and remaining stiffness quantification can be used for condition assessment of structures after extreme, hazardous events, which is extremely beneficial for emergency response. However, the forces which can induce damage to a structure can also damage the sensors on said structure, creating the need for an analysis using incomplete measurements. In this chapter, a simple two-phase damage localization and remaining stiffness quantification method was presented. In the method, damage is localized using limited measurements with direct model updating, and then the limited parameter subset is updated using least-squares optimization. The method was validated using a numerical model of the Phase I ASCE SHM benchmark problem with missing sensors on the first floor. For the numerical simulations, the method was able to accurately identify the damage location and quantify the remaining stiffness. Further validation was performed using experimental testing on the 5-story steel frame structure with a missing sensor on the first floor. The method was able to identify the damage locations, and was able to relatively accurately quantify the remaining stiffness in the structure. The validation showed the potential applicability of this method to quantify the remaining stiffness of structures after hazardous events, even if there are damaged or malfunctioning sensors. This method can be incorporated into future remaining life condition assessment methods for structures after hazardous events occur, to provide accurate assessments even with incomplete measurements.

5. OPTIMAL SENSOR PLACEMENT FOR DAMAGE ASSESSMENT

5.1. Introduction

Structural health monitoring (SHM) involves gathering measurements from a structure over time for a variety of applications, such as validating or updating numerical models, determining a structure's operational performance, monitoring stress for fatigue accumulation, and/or detecting feature changes which can be attributed to damage. SHM can be used for a wide variety of structures, including dams, tunnels, bridges, and buildings [51]. Due to an aging infrastructure network in the United States, along with an increased focus on the impact of extreme events on structures, the ability to detect damage to structures is a growing need. Knowing about current damage on a structure can be useful for assessing its safety, and planning long-term maintenance and operations. For SHM applications, one would ideally locate sensors at all of the available locations. However, this is frequently unfeasible due to data storage requirements and a limited number of available sensors, which is significantly less than the number of potential monitoring locations [12]. To place a limited number of sensors to gather the optimized information from the structure, optimal sensor placement (OSP) methods can be used.

Significant research focused on developing different OSP methods to locate sensors to detect damage, and comparing the sensor networks developed by different OSP techniques. However, the majority of the papers comparing OSP methods utilized evaluation metrics based upon the sensor placement. While these evaluation metrics monitor features which influence the SHM methods such as independence or energy of the measurements, they do not assess the capability of the SHM application with the sensor network. For the analyses of damage detection methods using limited sensor networks, with the exception of one paper, only a single OSP method was covered. By not utilizing multiple OSP methods, it is difficult to determine which OSP method to use for SHM purposes, especially with the varying structures and damage detection methods used by the authors.

This chapter assesses the capability of sensor networks developed by two OSP methods commonly used in literature, the EI and EI-DPR methods, to quantify parameter changes in a building structure. The two-phase stiffness estimation methodology for incomplete measurements, previously shown in Chapter 4, was modified to estimate changes in the mass or stiffness of a structure using a limited number of measurements. The addition of mass was included to expand the monitoring to be able to detect significant operational changes; such as overloaded trucks on a bridge, or heavy equipment on a building, etc. To validate the SHM method with limited sensor networks located with the OSP methods, the parameter localization and quantification was performed on an experimental lab-scale 7-story frame building, subjected to increased mass and reduced stiffness. Two sensor networks were developed using each OSP method, with three and five sensors, to monitor the first three bending modes. The results of the localization and quantification using the OSP sensor networks were analyzed with respect to the results using measurements from all 7 stories, to validate the performance of the parameter estimation with the optimally placed limited number of sensors. The parameter estimations from the two OSP methods were then compared, to determine which OSP method produced better sensor networks for the two phase parameter localization and quantification method.

5.2. Theory

Optimal Sensor Placement Methods

Two established OSP techniques are compared in this chapter; the EI and the EI-DPR methods. The EI method, proposed by Kammer [84], locates the sensors to maximize the linear independence of the modal information [84, 90, 91]. The EI method utilizes the Fisher information matrix ($\boldsymbol{A}$) from the mode shapes. Assuming uncorrelated measurement noise, the Fisher information matrix is below,

$$\boldsymbol{A} = \boldsymbol{\Phi_{sM}}^T \boldsymbol{\Phi_{sM}} \tag{5.1}$$

where $\boldsymbol{\Phi}$ are the mass normalized mode shapes, *s* are the potential monitoring DOF, and *M* are the modes of interest. The EI is then calculated as,

$$\boldsymbol{EI} = diag(\boldsymbol{\Phi_{sM}}(\boldsymbol{A^{-1}})\boldsymbol{\Phi_{sM}}^{T}) \tag{5.2}$$

The values of the EI vary from 0 to 1, with 0 meaning that the sensor provides no independent information, and 1 meaning that the information from the sensor is completely independent from any other sensor [84]. Sensor selection is performed through iterative removal of the sensor with the lowest EI value, until the required number of sensors is reached or all of the EI values are 1, meaning that all of the sensors are linearly independent from each other and no additional sensors can be removed.

The EI method can create sensor networks with low energy outputs [77, 85]. To increase the energy outputs at the sensor locations, the EI-DPR method weights the EI method with the driving point residue (DPR), which is a measure of the monitored DOF's relative modal contribution [77, 90]. The equation for the DPR for the monitored modes is shown below,

$$\boldsymbol{DPR_s} = \sum_{j=1}^{M} \frac{\Phi_{sj}^2}{\omega_j} \tag{5.3}$$

where ω is the natural frequency, *M* is the number of modes in the measurement range, and *j* is the j^{th} mode number. The DPR for each DOF is then multiplied by the EI for the DOF, as shown below,

$$\boldsymbol{EIDPR} = \boldsymbol{EI} \otimes \boldsymbol{DPR} \tag{5.4}$$

where $\otimes$ represents term-by-term multiplication. Sensor selection is then done iteratively, with the DOF that has the lowest EI-DPR value each iteration being removed as a candidate sensor location. The EI-DPR

method can be used to identify sensor locations which are linearly independent and have high energy responses [12, 77, 92].

Parameter Localization and Quantification

The quantification of the stiffness and mass parameters in this chapter is performed using the two phase localization and quantification methodology. For this approach, damage localization is performed using direct model updating to identify potential updating parameters. The localized, limited parameter subset is then used to quantify the parameter modifications. The mathematical descriptions of the localization and quantification are presented in the following sections.

Parameter Localization

The parameter localization is performed by comparing the analytical mass and stiffness matrices to experimentally updated mass and stiffness matrices from the structure; generated using a direct model updating method. The experimental mass and stiffness matrices are generated from the measured natural frequencies and mass-normalized mode shapes. Due to the limited measurement locations, SEREP expansion was used to expand the measured locations to all modeled DOF [79]. SEREP expansion consists of generating a transformation matrix (***T***) using an analytical model of the structure, and then using the transformation matrix to expand the measured mode shapes. The SEREP expansion procedure is shown below.

$$\boldsymbol{T} = \boldsymbol{\Phi}[(\boldsymbol{\Phi}_S{}^T\boldsymbol{\Phi}_S)^{-1}\boldsymbol{\Phi}_S{}^T] \tag{5.5}$$

$$\boldsymbol{\Phi}_{E_{SEREP}} = \boldsymbol{T}\boldsymbol{\Phi}_E \tag{5.6}$$

Using the SEREP expanded measured mode shapes, the experimental stiffness and mass matrices are calculated using the efficient model correction (EMC) method [59, 61]. To account for unmeasured modes, the corresponding analytical modes are substituted into an experimentally updated modal matrix ($\boldsymbol{\Phi}_D$), shown below,

$$\boldsymbol{\Phi_D} = \sum_{\boldsymbol{i=1}}^{\boldsymbol{m}} \boldsymbol{\phi_{E_{SEREP},i}} + \sum_{\boldsymbol{i=m+1}}^{\boldsymbol{M}} \boldsymbol{\phi_{A,i}} \tag{5.7}$$

where $\boldsymbol{m}$ is the number of measured modes, $\boldsymbol{M}$ is the number of modes in the full matrix, $\boldsymbol{\phi}_{E,SEREP}$ are the SEREP expanded experimental mode shapes, and $\boldsymbol{\phi}_A$ are the analytical mode shapes. A transformation matrix ($\boldsymbol{R}$) for the EMC is then calculated from the experimentally updated and analytical mode shapes [59, 61], shown below.

$$\boldsymbol{R} = \boldsymbol{\Phi_D}\boldsymbol{\Phi_A}^{-1} \tag{5.8}$$

The EMC transformation matrix is used to create the experimental mass matrix ($\boldsymbol{M}_E$), the modified stiffness matrix ($\boldsymbol{K}^*$), and the modified mode shape ($\boldsymbol{\Phi}^*$) matrix using equations 5.9-5.11 respectively,

$$\boldsymbol{M}_E = (\boldsymbol{R}^{-1})^T \boldsymbol{M_A} \boldsymbol{R}^{-1} \tag{5.9}$$

$$\boldsymbol{K}^* = (\boldsymbol{R}^{-1})^T \boldsymbol{K_A} \boldsymbol{R}^{-1} \tag{5.10}$$

$$\boldsymbol{\Phi}^* = \boldsymbol{R}\boldsymbol{\Phi_A} \tag{5.11}$$

where $\boldsymbol{M_A}$ is the analytical mass matrix. The experimental stiffness matrix ($\boldsymbol{K}_E$) can then be calculated as,

$$\boldsymbol{K_E} = \boldsymbol{K}^* + \boldsymbol{M}_E[\sum_{i=1}^{\boldsymbol{M}} \left(\boldsymbol{\omega}_{D,i}{}^2 - \boldsymbol{\omega}_{A,i}{}^2\right) \boldsymbol{\Phi}^*{}_i * \boldsymbol{\Phi}^*{}_i{}^T] \boldsymbol{M}_E \tag{5.12}$$

where $\boldsymbol{\omega}_D$ are the natural frequencies corresponding to the experimental and analytical mode shapes in $\boldsymbol{\Phi}_D$.

To localize the parameter modifications, the experimental mass and stiffness matrices are compared to their analytical counterparts. An increase in the experimental mass over a threshold percent, or a decrease

in the experimental stiffness over a threshold percent, indicate that the specific DOF is a potential location for parameter modification. The equations for the mass and stiffness localization are shown in equations 5.13 and 5.14 respectively,

$$\frac{M_{E,i,i}-M_{A,i,i}}{M_{A,i,i}} * 100\% < Threshold_M(\%) \tag{5.13}$$

$$\frac{K_{E,i,i}-K_{A,i,i}}{K_{A,i,i}} * 100\% > Threshold_K(\%) \tag{5.14}$$

where *i* is the i[th] DOF, $Threshold_M$ is the threshold for mass parameter identification, and $Threshold_K$ is the threshold for stiffness parameter identification.

Parameter Quantification using Genetic Algorithm

Once the localization has identified the subset of DOF that have potential mass or stiffness parameter modifications, the changes in the selected parameters are quantified using a genetic algorithm (GA) to optimize the subset of updating parameters to reflect the experimental measurements. For the mass parameters, updating occurs by adding mass to the selected DOF. Stiffness parameter updating is performed by reducing the average diameter of the columns on the floors which connect to the identified stiffness DOF. Optimization occurs through the minimization of the objective function (*J*), shown below,

$$J(\theta) = W_{freq} \sum_{i=1}^{m} (\frac{\omega_{\theta,i}}{\omega_{E,i}} - 1)^2 + W_{mode} \sum_{i=1}^{m} (COMAC_i - 1)^2 \tag{5.15}$$

where θ are the localized stiffness and mass optimization parameters, W_{freq} and W_{mode} are the weights of the natural frequency and mode shapes respectively, and *COMAC* is the coordinate modal assurance criterion,

$$COMAC_i = \frac{\left(\sum_{j=1}^{n} \phi_{E,ij}^T \phi_{\theta,ij}\right)^2}{\left(\sum_j^N \phi_{E,ij}^T \phi_{E,ij}\right)\left(\sum_j^N \phi_{\theta,ij}^T \phi_{\theta,ij}\right)} \tag{5.16}$$

where ϕ_E are unity normalized experimental mode shapes from the monitored DOF, and ϕ_θ are unity normalized mode shapes from the updated model for the monitored DOF. For this work, the frequency and mode shape objective weights were set at 10 and 1 respectively [105]. These weights reflect the higher confidence in accurate frequency measurements versus measured mode shapes.

A GA is a metaheuristic method to find near-optimal solutions for optimization problems, which can be used to perform the optimization of the multi-objective function shown in equation 5.15 [106]. The GA begins by randomly generating an initial population of chromosomes, or sets of solutions for the individual optimization parameters. Each chromosome is then evaluated using equation 5.15. A percentage of the chromosomes with the fittest solutions, or minimal objective values, are chosen to be parents in the next generation. The next generation of chromosomes, or children, are then created from the parents of the past generation, using the crossover function,

$$Child = ParentA(\beta) + ParentB(1-\beta) \tag{5.17}$$

where *ParentA* and *ParentB* are randomly selected chromosomes from the parent pool, and β is a random value from zero to one which is used to determine how much of each parent each parameter of the child is made up of [106]. To maintain population diversity and avoid local minima, a proportion of the children are subjected to a mutation function. The mutations are defined as additions or subtractions to the optimization parameter within a mutation range, using randomly selected parameters within the population of children. The number of mutations is a percentage of the number of optimization parameters within the population, and the mutation range decreases as the GA progresses. The GA finishes when convergence occurs, which is defined as when the overall fittest objective function for all iterations hasn't decreased by more than the convergence threshold for the number of iterations required to achieve convergence. The GA

is then be repeated, due to the fact that the use of random variables means the GA may not converge to the near-optimal solution every time. The framework of the GA procedure is shown in Figure 5.1.

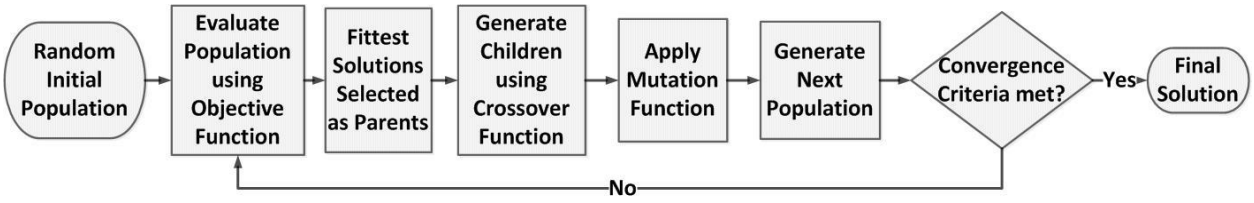

Figure 5.1 Genetic algorithm framework

5.3. Experimental Testing

To test the performance of the two OSP methods for parameter localization and quantification, a 7 story modifiable steel frame structure, shown in Figure 5.2(a), was utilized. The floors of the structure are 22.7 cm wide, 22.7 cm long, and 0.3 cm thick. The columns are each 10.2 cm tall with a diameter of 0.645 cm. An analytical model of the structure with 525 DOF was created in SAP2000, shown in Figure 5.2(b). The floors were modeled as thin shells, and the columns as frame elements. For this work, the model was condensed to the 7 translational DOF at the center of each floor, using Guyan condensation [98]. The condensed model is shown in Figure 5.2(c), where **X** represents the translation DOF, the arrow to the left of the model represents the location of the impact force, and the arrows to the right represent the condensed, monitored DOF.

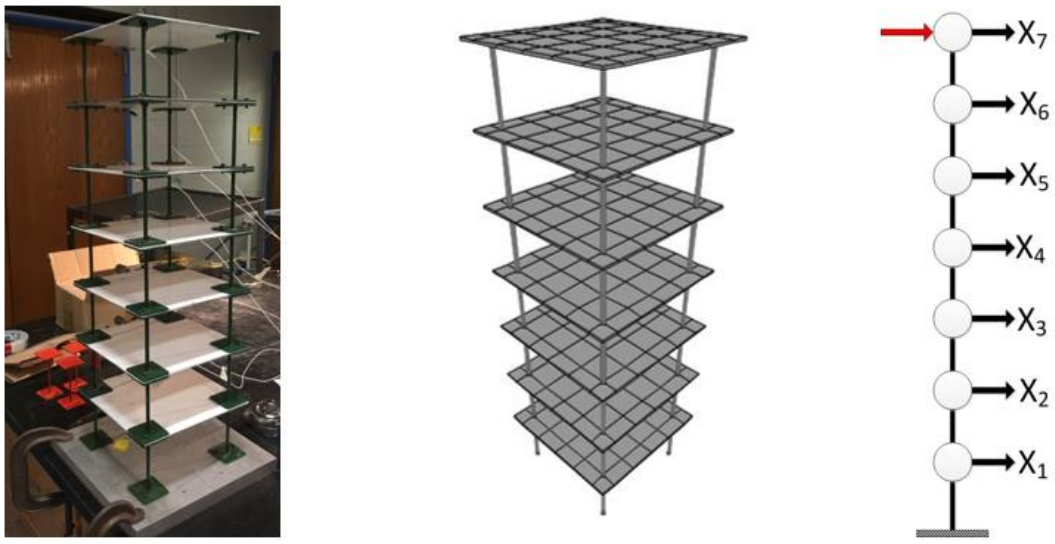

Figure 5.2 Steel frame structure experimental set-up and analytical model

The experimental testing utilized 7 PCB 353B33 accelerometers attached on the sides of each floor in the direction of excitation; with impulse excitation provided using a PCB 086C03 impact hammer on the seventh floor. Acceleration measurements were recorded using a sampling frequency of 512 Hz for 8 seconds, with a uniform window. In this work, the natural frequencies and mode shapes from the experimental measurements were determined using the numerical algorithms for state space system identification (N4SID) procedure [107].

An example time history from the unmodified experimental testing is shown in Figure 5.3, with the top plot showing the force from the impact hammer, and the bottom plot showing the measured accelerations from the seventh floor of the structure. The frequency response functions (FRF) and coherence function from all sensors of the unmodified experimental measurements, up to 100 Hz, are shown in Figure 5.4. The FRF shows clear poles and zeros, with the coherence function showing values of approximately 1 except at those locations. This verifies the quality of the data, and indicates the validity of the modal analysis as the three peaks were identified as the first three bending modes.

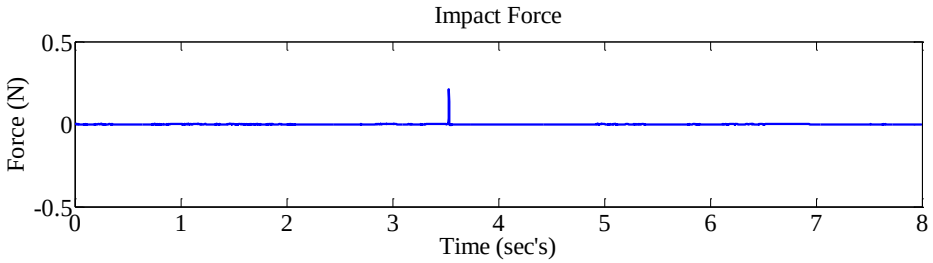

(a) Input Force: Impact Hammer

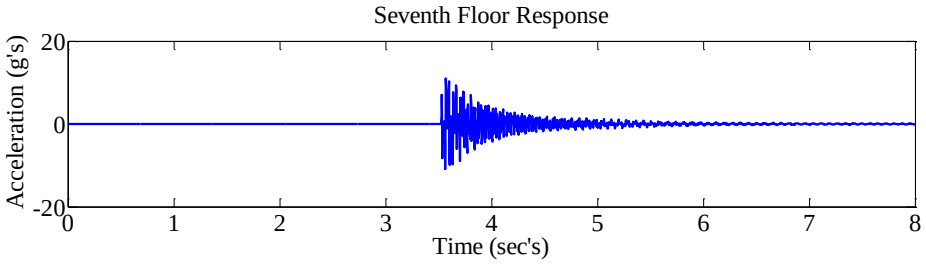

(b) Acceleration: sensor 7 (X7)

Figure 5.3 Example time history from unmodified test

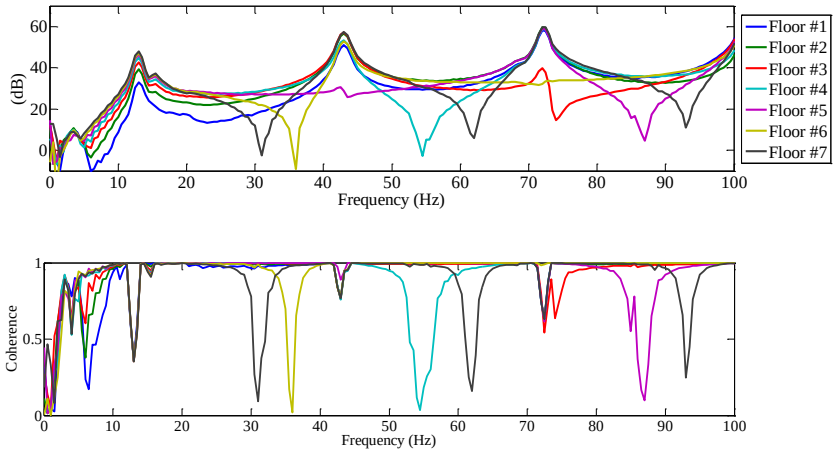

Figure 5.4 Example frequency response function and coherence from unmodified test

In total, 4 different scenarios have been considered for mass and stiffness parameter identification (see Table 5.1). In scenario 1, 0.5 kg of mass has been securely attached on the 5th floor to simulate an increased

mass on a specific floor. Scenario 2 reduced the diameter of all 4 columns on the first floor by 24.2%, which equates to approximately a 77% reduction in their bending stiffness. Stiffness reduction is a common damage which can be due to steel corrosion, concrete cracking, fires, or other extreme events. For scenario 3, the 0.5 kg mass was attached to the 5^{th} floor of the structure from scenario 2, to assess the capability of the parameter estimation to perform on an already modified structure. Providing progressive modification assessments would be important for long-term SHM. Scenario 4 instituted multiple parameter modifications, with 24.2% reduction in the first floor diameters, and a 24.5% reduction in the fifth floor diameters which equated to a bending stiffness reduction of approximately 46.6%. The experimental structures for each scenario are shown in Figure 5.5 with scenario 1 shown in (a), scenario 2 in (b), scenario 3 in (c), and scenario 4 in (d).

Table 5.1 Parameter modification scenarios

Scenario number	**Scenario type**	**Parameter Modification Location**
1	0.5 kg mass addition	Floor 5
2	75.8% remaining column diameter	Floor 1
3	75.8% remaining column diameter 0.5 kg mass addition	Floor 1 Floor 5
4	75.8% remaining column diameter 75.5% remaining column diameter	Floor 1 Floor 5

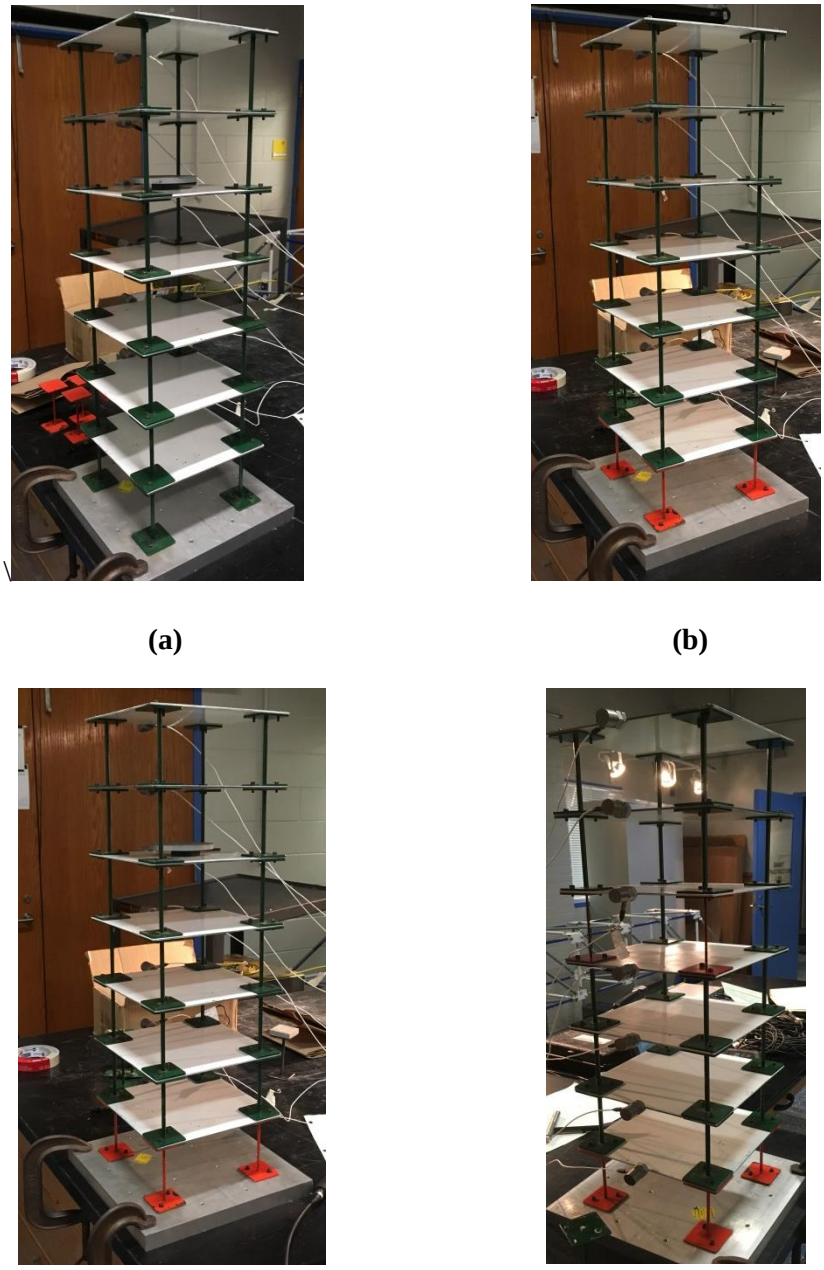

(a) **(b)**

(c) **(d)**

Figure 5.5 Experimental parameter modification scenarios

To compare the parameter quantification using the different OSP methods, sensors were located using the EI and EI-DPR methods to monitor the first three bending modes. The first three bending modes were used due to experimental limitations in gathering accurate measurements at higher frequencies. The natural

frequencies for the three bending modes from the analytical model, as well as from each experimental test scenario, are shown in Figure 5.6. The unmodified experimental and analytical natural frequencies are 3%, 4% and 0.1% different for the first three bending modes respectively, representing a good original analytical model. Further refinements in the analytical model were made through optimization of the column average diameters using the experimental measurements from the unmodified scenario, using the full and OSP sensor networks for each respective analysis. Additionally, it can be seen that the reductions in column diameter, and additions of mass caused reductions to the natural frequencies, which was expected.

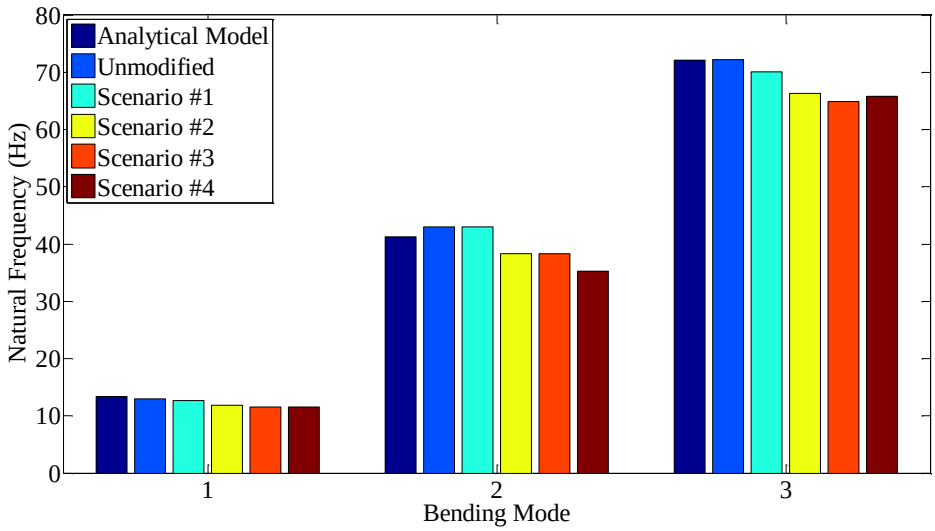

Figure 5.6 Analytical and experimental natural frequencies

Sensor networks have been developed using the EI and EI-DPR OSP methods to monitor the first three bending modes, using three and five sensors. The sensor reduction equates to approximately 43% and 71% of potential locations for the reduced model respectively. However, when compared to the original FEM the limited sensors equate to approximately 0.57% and 0.95% of the potential sensor locations respectively. The sensor networks for each OSP method are presented in Table 5.2, which shows the floors of the sensors used in the localization and quantification. Using both methods, the second and the top floors were always included, showing the relevance of the information provided by those locations. The experimental

measurements were gathered using all 7 sensors, with only the measurements from the OSP sensors used for their respective analyses. To provide a reference, the SHM was also performed using all 7 sensors.

Table 5.2 OSP sensor networks

Number of Sensors / OSP Method	Sensor Locations		
	3 Sensors	**5 Sensors**	**7 Sensors**
Effective Independence (EI)	2, 4, 7	2, 3, 4, 5, 7	1-7
Effective Independence – Driving Point Residue (EI-DPR)	2, 5, 7	2, 4, 5, 6, 7	1-7

5.4. Results

Using the sensor networks identified by the OSP techniques, parameter estimation was used to quantify the diameter reduction of the column(s) and to quantify the added mass. This process was performed through model updating of the first three bending modes using the experimental measurements. The process began by updating the original model with the unmodified experimental measurements, to account for minor modeling errors. For the unmodified experimental updating, all of the floor column diameters were used as optimization parameters. The updating was completed using the experimental measurements from each sensor network, for their respective analyses, with the updated models having natural frequencies within 0.1% of the experimental values. The close match between the updated and experimental natural frequencies led to the conclusion that the updated models provide an accurate representation of the experimental structure. For the parameter localization and quantification with the modification scenarios, the updated unmodified models were used instead of the original analytical model, except for scenario 3

where the model with the parameter modifications identified from scenario 2 was used as the analytical model.

Using the updated unmodified models, the localization and quantification described in section 2 was completed using the measurements from each sensor network. The localization utilized a mass threshold of 0.3% and a stiffness threshold of -0.3%, and the quantification GA used the parameters in Table 5.3. For each scenario, the GA only updated either additional mass or column diameter reductions, depending upon the parameter modification.

Table 5.3 Genetic algorithm parameters

Parameter	Value	Parameter	Value
GA Iterations	2	Mutation Reduction Iterations	20
Population	150	Convergence Iterations	50
Parent Percentage	15%	Convergence Threshold	$5x10^{-7}$
Mutation Percent	20%	Minimum Mutation Percentage	1%
Mutation Reduction Rate	50%		

Parameter Localization and Quantification using the EI method

The quantifications for each floor for the unmodified scenario and each parameter modification scenario using the EI sensor networks are shown in Figure 5.7. The left three figures show the remaining diameters of the columns for the unmodified scenario and scenarios 2 and 4, and the right two figures are showing the changes in mass of the floors for scenarios 1 and 3. In each plot, the first column (in blue) indicates the quantification results using 7 sensors, the second column (in green) indicates the quantification results using 5 sensors, and third column (in red) indicates the quantification results using 3 sensors. The close match between the quantifications using 5 and 7 sensors shows the ability of the methodology to estimate the parameter modifications using 5 sensors. The one notable exception is scenario 3. However, as that model

uses the updated analytical model from scenario 2, some increase in quantification error was expected. With a decrease in sensors from five to three, an increase in the quantification errors for the stiffness reduction can be seen. This was expected, as reduced sensors provide less information to update. However, scenario 2 is the only scenario where the error is 10% greater than with 5 sensors. For the increased mass scenarios, there is relatively little change in the localization and quantification with the reduction in sensors.

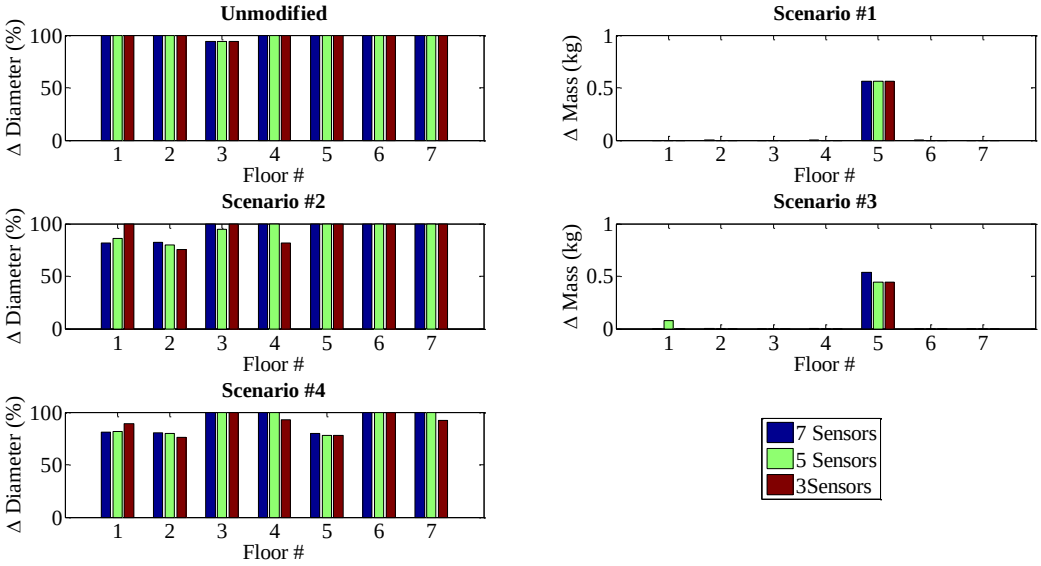

Figure 5.7 Sensor networks parameter quantification: EI method

The results from the localization and quantification using five and three sensors located with the EI method are shown in Tables 5.4-5.5 respectively. The updating parameter percentages show the percentage of potential updating parameters selected by the localization method. In each scenario, all of the modified parameters were correctly identified. The localization reduced the number of updating parameters in the majority of cases, with the reduction depending upon the parameter modifications. The mass modification scenarios, which affected a single DOF, provided better localizations than the column diameter reductions, which influenced multiple DOF.

Tables 5.4-5.5 also show the parameter quantifications from the 7 sensors, the OSP sensor network, and the OSP quantification errors in relation to the 7 sensor quantifications. As the quantification with 7 sensors reduced the column diameter for the second floor when the first floor column diameter was reduced, likely due to modifications at the column-floor connections when the thicker columns were replaced with the thinner columns, the error in the reduction of the second floor diameter is presented when applicable. The quantification with five sensors produced errors around 5 percent or less, with the exception of scenario 3. The increased error in scenario 3 could be due to the use of the updated model using the modifications from scenario 2, with the errors being carried over. For the sensor network with three sensors, the errors were similarly low for scenario 1. However, they were higher for the other scenarios, except for the fifth column in scenario 4. This was particularly true for scenario 2, which failed to quantify the diameter reduction on the first floor, and instead further reduced the diameter on the second floor. The sensor network with three sensors also modified the diameter of the fourth floor columns in scenarios 2 and 4. The increase in quantification error was expected as the number of sensors was reduced, due to the decrease in information from the measurements. With the coarse network demonstrated by the three sensors, it may be more viable to use the proposed methodology for detection of parameter modifications, with accurate quantification being unachievable.

Table 5.4 Parameter localization and quantification : EI sensor network with 5 sensors

Scenario	Updating Parameters (%)	Seven Sensor Quantification	EI Sensor Quantification	Error (%)
1	28.57%	Floor 5 : 0.56 kg	Floor 5 : 0.56 kg	Floor 5 : -0.18%
2	71.43%	Floor 1 : 81.89% Floor 2 : 82.21%	Floor 1 : 86.02% Floor 2 : 80.08%	Floor 1 : 5.05% Floor 2 : -2.59%
3	57.14%	Floor 5 : 0.54 kg	Floor 5 : 0.44 kg	Floor 5 : -17.27%
4	100.00%	Floor 1 : 81.07% Floor 2 : 80.42% Floor 5 : 79.58%	Floor 1 : 81.96% Floor 2 : 79.82% Floor 5 : 77.90%	Floor 1 : 1.10% Floor 2 : -0.74% Floor 5 : -2.11%

Table 5.5 Parameter localization and quantification : EI sensor network with 3 sensors

Scenario	Updating Parameters (%)	Seven Sensor Quantification	EI Sensor Quantification	Error (%)
1	57.14%	Floor 5 : 0.56 kg	Floor 5 : 0.56 kg	Floor 5 : -0.05%
2	100.00%	Floor 1 : 81.89% Floor 2 : 82.21%	Floor 1 : 100% Floor 2 : 75.63%	Floor 1 : 22.12% Floor 2 : -8.01%
3	71.43%	Floor 5 : 0.54 kg	Floor 5 : 0.45 kg	Floor 5 : -17.03%
4	85.71%	Floor 1 : 81.07% Floor 2 : 80.42% Floor 5 : 79.58%	Floor 1 : 89.12% Floor 2 : 76.10% Floor 5 : 78.24%	Floor 1 : 9.92% Floor 2 : -5.37% Floor 5 : -1.68%

Parameter Localization and Quantification using the EI-DPR method

The quantifications for each floor for the unmodified and each modification scenario using the EI-DPR sensor networks are shown in Figure 5.8. The formatting is the same as for the EI sensor networks, from Figure 5.7. The mass quantification from scenario 1 produced little error. For scenario 2, both the five and three sensor networks falsely identified damage on the fourth floor. The reduction in the number of sensors from five to three also introduced more error. These results were consistent with scenario 4. There is an increasing error with a reduction in sensors for scenario 3; however this could be due to increased error in the analytical models generated from the parameter quantification from scenario 2.

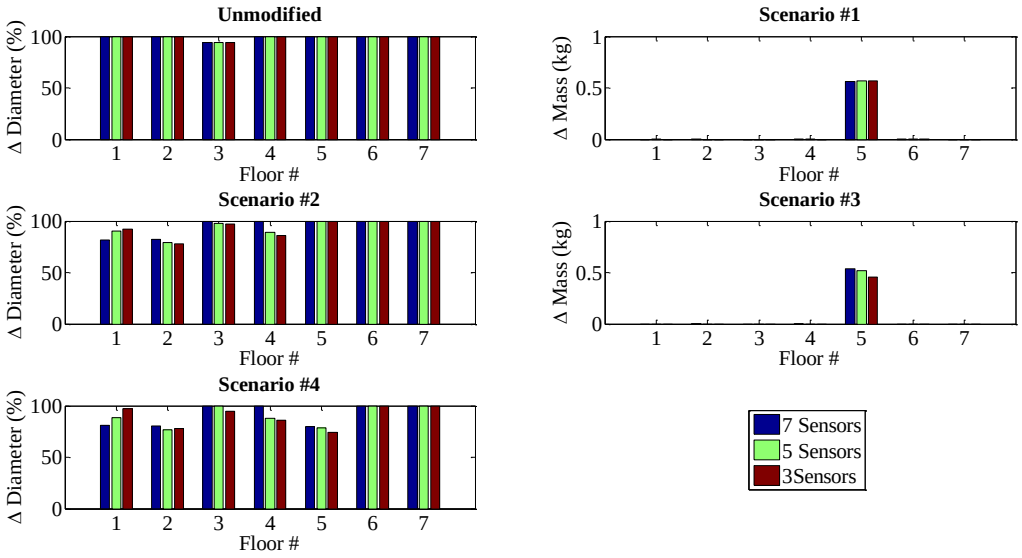

Figure 5.8 Sensor networks parameter quantification: EI-DPR method

The localization and quantification results from the EI-DPR sensor networks using five and three sensors are shown in Tables 5.6-5.7 respectively. All of the modified parameters were correctly identified in each scenario. The localization reduced the number of parameters for scenarios 1 and 3 for both EI-DPR sensor networks, and scenario 4 for the three sensor network. However, over 50% of the potential parameters were selected for each scenario. The increase in selected parameters using the

sensor network developed by the EI-DPR method should be considered in larger models, which can have an increased number of potential updating parameters.

The quantification errors for the modified parameters for the EI-DPR sensor networks with five and three sensors are also shown in Tables 5.6-5.7, with the same format as Tables 5.4-5.5. As previously stated for the EI sensor networks, as the quantification with 7 sensors reduced the column diameter for the second floor when the first floor column diameter was reduced, likely due to modifications at the column-floor connections when the thicker columns were replaced with the thinner columns, the error in the reduction of the second floor diameter is presented when applicable. The quantification using all five sensors produced quantification errors around 10 percent or lower. It is notable that the error for scenario three using five sensors is 3.17%, showing the capability of the parameter quantification to be used for multiple parameter modifications over time, due to the analytical model for scenario 3 being updated with the modified parameters from scenario 2. For the sensor network with three sensors, the errors were similar for scenario 1 and 2. However, they were significantly higher for scenarios 3 and 4. While the second floor column diameters in scenario 4 had a lower error than in the quantification with five sensors, this was likely due to the large increase in error for the first floor column diameters. Both sensor networks located with the EI-DPR method also reduced the column diameters for the fourth floor in scenarios 2 and 4.

Table 5.6 Parameter localization and quantification : EI-DPR sensor network with 5 sensors

Scenario	Updating Parameters (%)	Seven Sensor Quantification	EI-DPR Sensor Quantification	Error (%)
1	71.43%	Floor 5 : 0.56 kg	Floor 5 : 0.57 kg	Floor 5 : 0.45%
2	100.00%	Floor 1 : 81.89% Floor 2 : 82.21%	Floor 1 : 90.22% Floor 2 : 79.08%	Floor 1 : 10.17% Floor 2 : -3.81%
3	57.14%	Floor 5 : 0.54 kg	Floor 5 : 0.52 kg	Floor 5 : -3.17%
4	100.00%	Floor 1 : 81.07% Floor 2 : 80.42% Floor 5 : 79.58%	Floor 1 : 88.78% Floor 2 : 76.40% Floor 5 : 78.70%	Floor 1 : 9.51% Floor 2 : -5.00% Floor 5 : -1.11%

Table 5.7 Parameter localization and quantification : EI-DPR sensor network with 3 sensors

Scenario	Updating Parameters (%)	Seven Sensor Quantification	EI-DPR Sensor Quantification	Error (%)
1	57.14%	Floor 5 : 0.56 kg	Floor 5 : 0.57 kg	Floor 5 : 0.31%
2	100.00%	Floor 1 : 81.89% Floor 2 : 82.21%	Floor 1 : 92.50% Floor 2 : 77.95%	Floor 1 : 12.96% Floor 2 : -5.18%
3	57.14%	Floor 5 : 0.54 kg	Floor 5 : 0.46 kg	Floor 5 : -15.29%
4	85.71%	Floor 1 : 81.07% Floor 2 : 80.42% Floor 5 : 79.58%	Floor 1 : 97.47% Floor 2 : 77.79% Floor 5 : 74.50%	Floor 1 : 20.23% Floor 2 : -3.27% Floor 5 : -6.39%

Comparison of OSP methods from Experimental Results

The results of the localization and quantification using the sensor networks developed with the EI and EI-DPR methods with five and three sensors can be used to compare the OSP methods capability for parameter localization and quantification using the described methodology. To illustrate the differences between the methods, the quantifications using each OSP method with five sensors and three sensors are presented in Figure 5.9 and Figure 5.10 respectively, with the blue bars representing the quantification using all 7 sensors, the green bars representing the quantification using the EI sensor network, and the red bars representing the quantification using the EI-DPR sensor network. As can be seen, for the sensor networks with five sensors, the EI sensor network produced quantifications with lower errors than the EI-DPR sensor network when compared to the full sensor network, except for scenario 3. For three sensors, the EI-DPR sensor network produced quantifications with lower or similar errors to those from the EI sensor network, except for scenario 4.

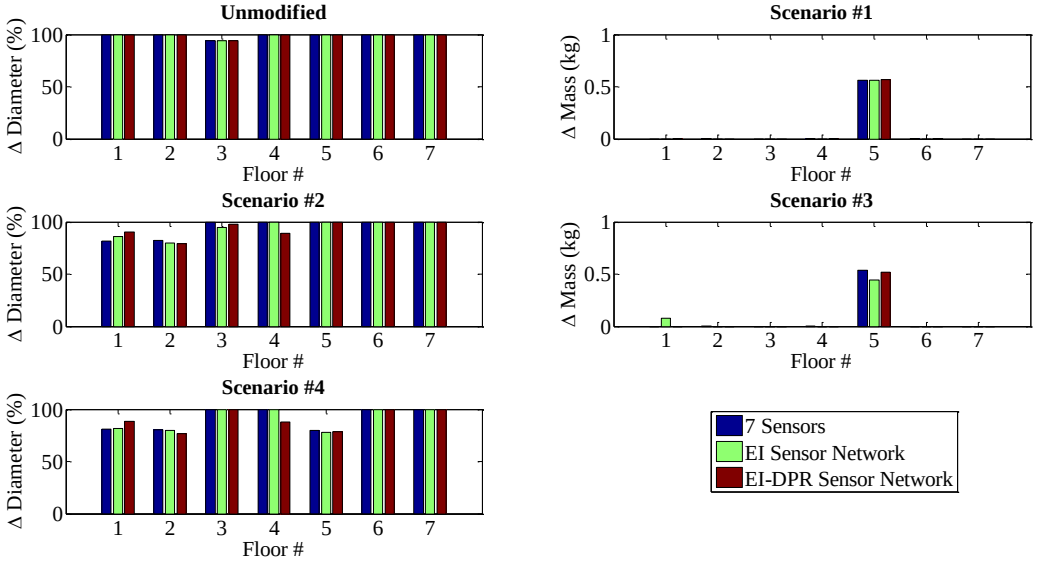

Figure 5.9 Sensor networks parameter quantification: five sensors

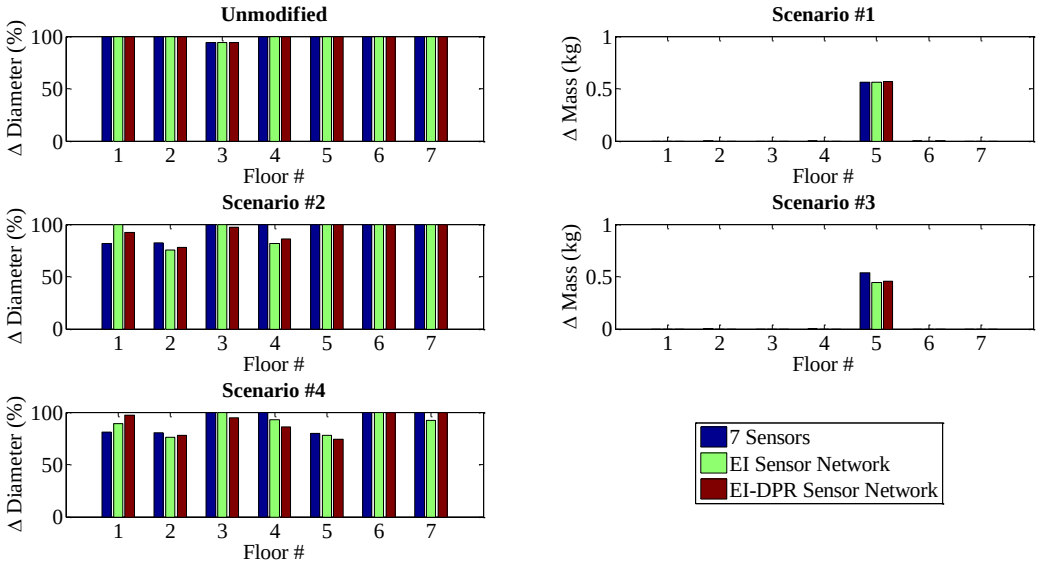

Figure 5.10 Sensor networks parameter quantification: three sensors

While the sensor networks developed with both OSP methods using five sensors were able to provide accurate quantifications of the parameter modifications, from the presented results it can be seen that the EI sensor network was more effective for the parameter localization and quantification. This was due to the improved parameter selection and reduced quantification errors. The EI methods' improved performance is likely due to its focus on increased monitored modal information and linear independence, which provides more information for the localization and quantification. Improvements in the localization method would be beneficial for improved results, especially for larger models and real-world applications.

For the parameter localization and quantification with the sensor networks with three sensors, both networks accurately quantified the added mass for scenario 1, the EI-DPR sensor network performed better for scenarios 2 and 3, and the EI sensor network producing a better quantification for scenario 4. However, both sensor networks had consistent difficult quantifying the first floor column diameter reductions. While the quantification with three sensors can be said to locate parameter modifications quite well, with a coarse sensor network large quantification errors and false assessments need to be expected.

The results demonstrate that both the EI and EI-DPR methods are capable of locating sensors to quantify parameter changes using the two-phase parameter localization and quantification methodology with enough sensors. With a denser sensor network, the EI method produced better parameter modification quantifications, and was able to reduce the number of parameters to modify for the simpler modification scenarios. With the coarser network, both sensor networks experienced an increase in quantification error. But, both networks show potential for utilization for parameter modification detection purposes using the described methodology.

5.5. Conclusions

For large scale SHM applications, OSP methods can be utilized to locate the limited number of sensors to provide the best evaluations of the structures. In this chapter, the two phase parameter localization and quantification method was validated for parameter estimation using OSP sensor networks developed with the EI and EI-DPR methods. Accurate assessments were provided with both networks using five sensors, with comparisons of the results showing that the EI sensor network provided the best parameter estimations. With coarser OSP sensor networks using only three sensors, both methods produced significant errors, and may be better used for detection instead of quantification. The results provide insight on the selection of OSP method, and sensor network density, for locating sensors on buildings to monitor for parameter modifications using the presented two phase localization and quantification methodology. This chapter also shows the impact of number of sensors on quantification errors, and how if the sensor network is too coarse accurate parameter quantification may be impossible with detection presenting a viable alternative.

6. ADAPTIVE ALTERNATE PATH ANALYSIS

6.1. Introduction

Progressive collapse can be described as when a local structural failure or damage occurs which leads to an extensive or complete failure of the building, disproportionate to the initial damage event [108]. After events such as the Ronan Point apartment collapse (1968), Murrah Building bombing (1995), and World Trade Center collapse (2001), progressive collapse analysis of structures has become an extremely important research focus. Different types of extreme events can lead to progressive collapse, including impact loads for vehicle crashes, earthquakes, fires, or explosions [41]. The department of defense presents guidelines to design structures to resist progressive collapse in the unified facilities criteria (UFC) 4-023-03 [11]. One of the methods to design a structure to resist progressive collapse is the alternate path (AP) method. While useful for design, it does not provide an ability to assess a structure for its potential for progressive collapse after a blast. In addition, a drawback to the AP method is that it does not consider additional damage to members adjacent to the one to be removed, which could cause significant changes in the structures potential for progressive collapse [3, 4].

Should a structure not suffer a progressive collapse immediately after an explosion, the ability to quickly assess its probability of failure would be beneficial to emergency responders and structure stakeholders. The post-event structural probability of failure can be used to determine safe emergency operations, and monitor for further structural degradation. An ideal assessment method should ideally not involve putting personnel into potentially dangerous situations. Structural health monitoring (SHM) can be used to determine a structures post-blast probability of failure using measurements from the post-event structure to generate an updated structural model. The updated model would include changes in the structure reflecting the real-life damage. An alternate path analysis would then be performed on the updated structure, providing the benefit of including damage to additional elements beyond the critical member(s) for removal. As the AP method is threat independent, knowledge of the size and location of the explosion would not be

required. Since the measurements would be recorded using a previously installed sensor network, no additional personnel would need to be put in harm's way to assess the structures safety. The sensor network itself can also be utilized to perform a variety of monitoring applications for the building.

In this chapter, a method is proposed to determine the elemental probability of failure for a structure after a blast is presented. As progressive collapse occurs after a local failure, when additional elements cannot transfer the additional loads, determining the elemental probability of failure is one method to monitor for progressive collapse. The proposed method is demonstrated using a modified version of the steel frame structure found in Appendix E of the UFC guidelines [11]. To demonstrate the impact of additional damage on the final condition assessment, a study on the impact of added damage was performed using simulated structural damage to non-removed elements. Additionally, a numerical blast simulation is performed to demonstrate a scenario where the adaptive alternate path method could be used to assess a structures probability of failure. Damage was assessed to the building due to the numerical blast, and simulated measurements from the damaged model were used to generate an updated, equivalent model which reflected the damage. From the updated model the elemental probability of failure was calculated using the adaptive alternate path method.

6.2. Methodology

The adaptive alternate path method involves generating an updated numerical model of the post-blast damaged structure using experimental measurements. An AP analysis is then performed to determine the structures potential for progressive collapse. The methodology for the model updating and AP analysis are discussed in this section.

Model Updating

Updating of the analytical model to represent the experimental, post-event, structure is done using a two-phase localization and quantification methodology to minimize the differences between the experimental and analytical natural frequencies and mode shapes. Localization is performed through direct model

updating of the analytical model using the efficient model correction (EMC) method. The experimentally updated stiffness matrix is compared to the original analytical model, with potential damage DOF identified through decreases in the diagonal of the stiffness matrix. Columns connected to the potentially damaged DOF are identified for updating. The mathematical formulation of the localization method can be found in Section 5.3.

Once the updating parameters are localized, damage quantification is performed through optimization of the model to minimize the objective function shown in equation 6.1, which is also shown in Chapters 4 and 5 as equations 4.7 and 5.15,

$$J(\theta) = W_{freq} \sum_{i=1}^{m} (\frac{\omega_{\theta,i}}{\omega_{E,i}} - 1)^2 + W_{mode} \sum_{i=1}^{m} (COMAC_i - 1)^2 \tag{6.1}$$

where θ are the optimization parameters, W_{freq} and W_{mode} are the weights of the natural frequency and mode shapes respectively which were set at 10 and 1 respectively [105], and *COMAC* is the coordinate modal assurance criterion,

$$COMAC_i = \frac{(\sum_{j=1}^{n} \phi_{E,ij}^T \phi_{\theta,ij})^2}{(\sum_j^N \phi_{E,ij}^T \phi_{E,ij})(\sum_j^N \phi_{\theta,ij}^T \phi_{\theta,ij})} \tag{6.2}$$

where ϕ_E are unity normalized experimental mode shapes from the monitored DOF, and ϕ_θ are unity normalized mode shapes from the updated model for the monitored DOF. For this work, the updating parameters used were the elastic and shear moduli of the identified frame elements. The objective function is minimized using a genetic algorithm (GA). A description of the GA can be found in Section 5.3.

Adaptive Alternate Path Method

Once the equivalent structural model has been generated using the damage localization and quantification, the progressive collapse probability of failure can be determined using the adaptive AP analysis. For the

design of structures, the AP method is used to determine if a structure is capable of developing alternate load paths to compensate for the removal of an element. For the adaptive AP analysis, the same procedure is performed using the updated model, and the structural response is compared to the design acceptance criteria to determine each elements probability of failure. In this work, the nonlinear dynamic AP method is used. As a progressive collapse occurs when structural elements cannot carry the additional loads caused by the removal of key elements, the failure of additional elements beyond the removed elements will be used as the failure criteria for the structure.

Elements with an elastic modulus reduction, from the model updating over a threshold percentage are identified as potentially failed. In this work, the threshold percentage is set at 80% of the original value. Elements which suffer a reduction greater than the threshold are removed in the AP analysis. Element removal is performed by replacing the element to be removed with equivalent joint forces. The equivalent forces supply the same reactions to the structure as the element for removal. For the adaptive AP analysis the equivalent forces are the forces from the original model. With the equivalent forces applied, the structure is allowed to settle to a steady-state condition. Loads with the equal and opposite value as the equivalent forces are then applied to "remove" the equivalent forces, at a rate under $1/10^{th}$ of the vertical period of the structure. The numerical model with the removed element is then allowed to settle to a steady-state condition.

After the model settles, the envelope response of elements subjected to plastic deformation is checked for determination of the elements probability of failure using the AP method. If the model fails, then it is assumed that the structure is likely to be subjected to a progressive collapse. If the model settles to a steady-state, for a non-linear dynamic analysis the envelope plastic hinge responses are compared to the acceptance criteria to determine the elemental probability of failure. For beam elements with M3 hinges, the probability of failure equation is presented below,

$$P_f = \frac{|\theta_{Upd}|}{\theta_{Acc}} \tag{6.3}$$

where θ_{Upd} is the plastic hinge rotation from the updated AP analysis, θ_{Acc} is the plastic hinge rotation for the acceptance criteria, and P_f is the elemental probability of failure. For columns with P-M2-M3 hinges, the probability of failure is determined by if the column is deformation-controlled ($P/P_c \leq 0.5$), or force-controlled ($P/P_c > 0.5$). Under deformation-controlled response, the probability of failure takes into account the rotations in both local DOF, shown below,

$$P_f = \frac{|\theta_{Upd,2}|}{\theta_{Acc,2}} + \frac{|\theta_{Upd,3}|}{\theta_{Acc,3}} \tag{6.4}$$

where $_2$ and $_3$ represent the local rotation DOF. For force-controlled hinges, the probability of failure is dependent upon the load capacity at the hinge, shown below,

$$P_f = \frac{P}{P_c} + \frac{M_2}{M_{2,c}} + \frac{M_3}{M_{3,c}} \tag{6.5}$$

where P is the axial load, P_c is the axial compressive load capacity, M_2 is the column moment in the weak axis direction, $M_{2,c}$ is the column moment capacity in the weak axis direction, M_3 is the column moment in the strong axis direction, and $M_{3,c}$ is the column moment capacity in the strong axis direction. The probability of failure of the structure is then determined as the maximum elemental value. The acceptance criteria for nonlinear plastic hinges of steel elements can be found in UFC 04-023-03 Table 5-2 [11], and/or chapter 5 of ASCE 41 [109]; with the acceptance criteria for the Life Safety condition governing the columns and the Collapse Prevention acceptance criteria for the flexural beams. Further details on performing a nonlinear dynamic AP analysis can be found in UFC 04-023-03 [11].

6.3. Numerical Model Development for Realistic Blast Simulation

To demonstrate the adaptive alternate path method, a numerical model of a steel frame structure, modified from the model used in UFC 04-023-04 appendix E, was developed in SAP2000. An equivalent numerical model was built in Abaqus 6.13-2, and used to simulate the structure under a blast. The simulated damage to the structure from the Abaqus blast simulation was then manually incorporated into the SAP2000 model. Model updating was performed using the mode shapes and natural frequencies from the damaged SAP2000 model to create the updated model. Each of these numerical models is described in this section.

UFC Modified Frame Structure

In this work a modified version of the steel frame structure found in UFC 04-023-04 appendix E is utilized [11]. Dimensions of the structure can be found in Figure 6.1. The member sections were chosen from the re-designed structure after the nonlinear dynamic analysis from UFC 04-023-04, and are shown in Figure 6.2. The applied loads were consistent with the dead, live, superimposed dead, and cladding loads present in the design example, shown in Table 6.1. To simplify the structural model, diaphragm constraints were used to model the floors. Modifications to the structure involved removal of the bracing elements, and changing the column-to-foundation connections from pinned to fixed. Plastic behavior was modeled using two P-M2-M3 hinges for each column, and three M3 hinges for each beam, with properties automatically determined by the SAP2000 software based upon ASCE 41-13, at the locations shown in Figure 6.3. The full numerical model is shown in Figure 6.4.

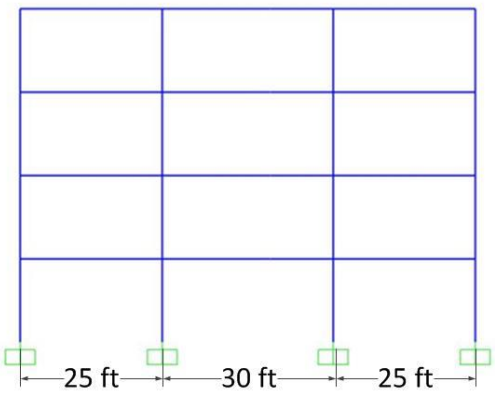

(a) Exterior cross section

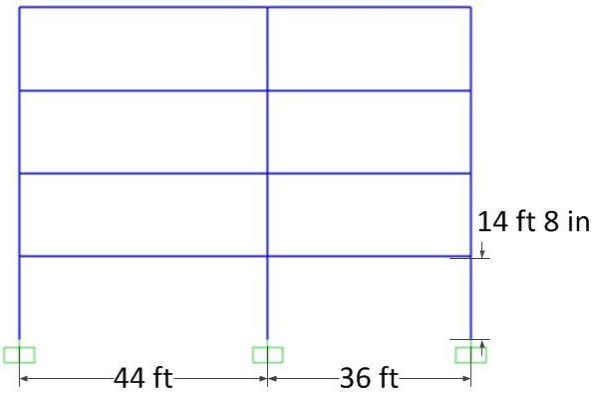

(b) Interior cross section

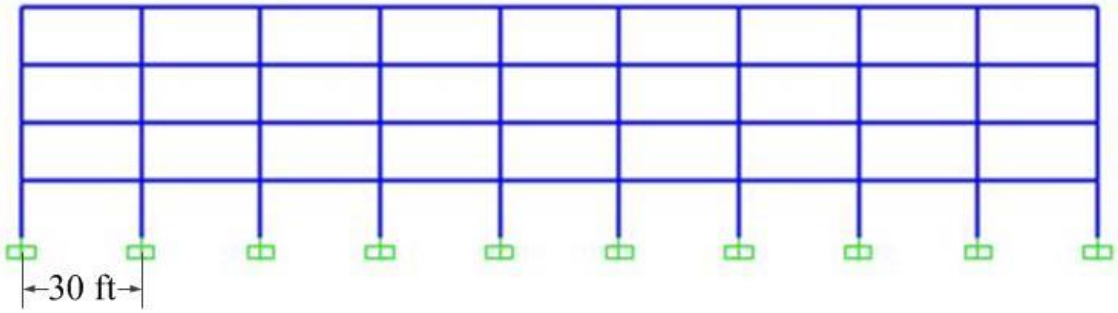

(c) Exterior side view

Figure 6.1 UFC modified structure dimensions

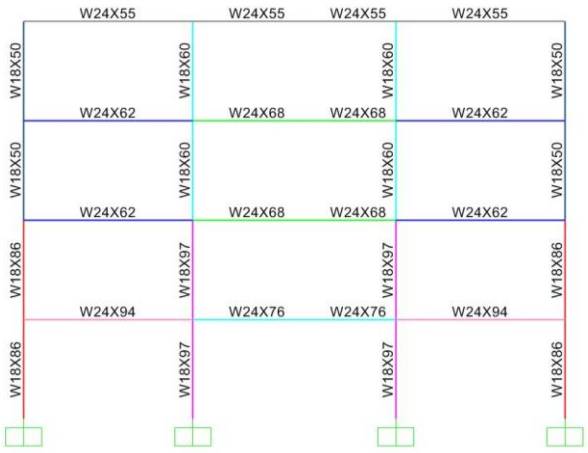

(a) Exterior cross section

(b) Interior cross section

(c) Interior side view

(d) Exterior side view

Figure 6.2 UFC modified structure sections

Table 6.1 UFC modified model structural loads

Load Type	Load Description	Weight
Dead Load	Floor	78 psf
	Roof	5 psf
Live Load	Floor	100 psf
	Roof	20 psf
Super Imposed Load	Ceiling Weight	15 psf
Cladding	Cladding	220 plf on perimeter

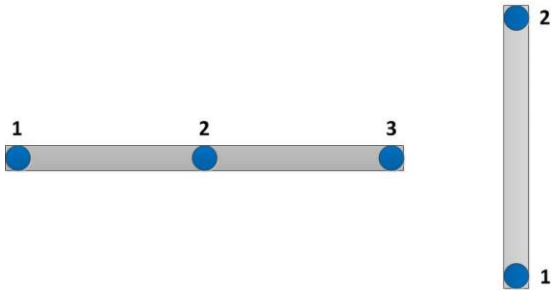

(a) Beam **(b) Column**

Figure 6.3 Element hinge locations

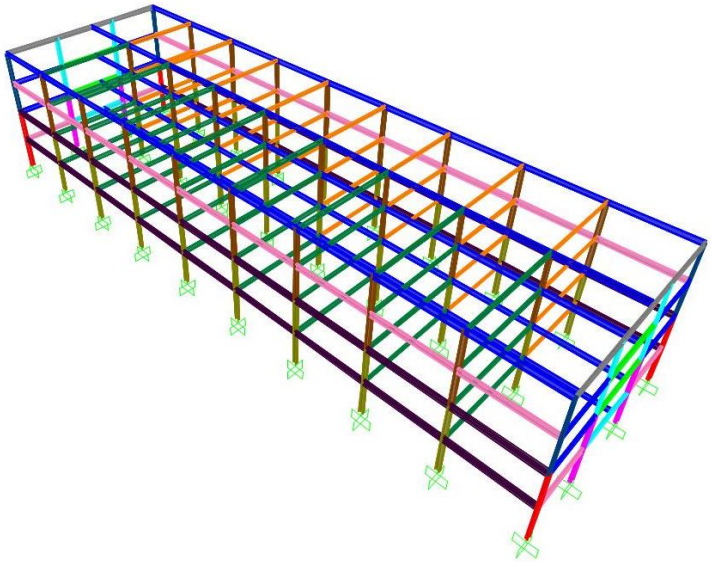

Figure 6.4 UFC modified structure

An alternate path analysis was performed on the modified model with column 21 from Figure 6.5, which is also circled in Figure 6.6, selected for removal. Column 21 was selected for removal as it is the column closest to the numerical blast used to demonstrate the adaptive alternate path method later in this chapter. To perform the alternate path analysis, a static analysis of the original structure without the column removal was first performed. From that analysis, the equivalent forces from the column for removal were determined. The values for the equivalent forces for column 21 are shown in Table 6.2, where *X* is into the page, *Y* is to the left, and *Z* is vertical.

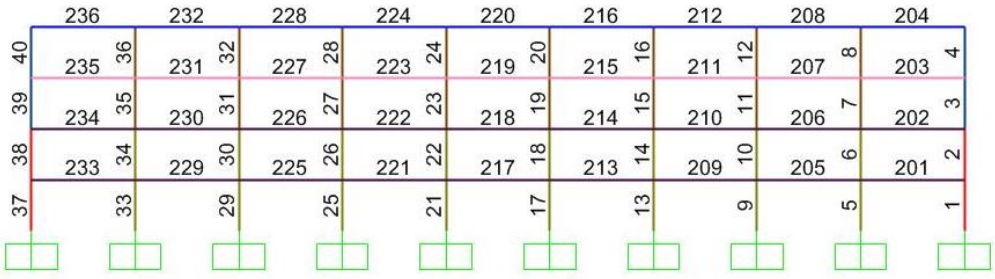

Figure 6.5 Exterior element number

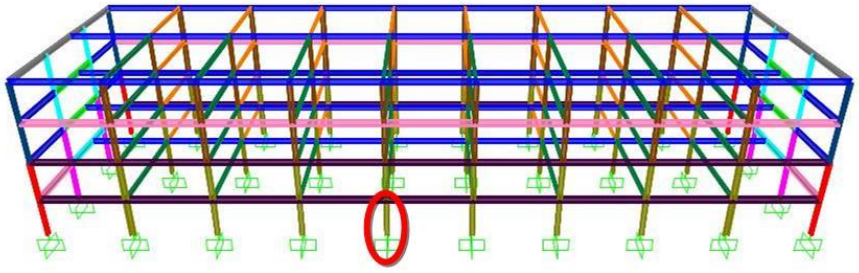

Figure 6.6 Column removal location

Table 6.2 Joint equivalent force

Force	Equivalent Value (kips)	Moment	Equivalent Value (ft-kips)
F_X	0.823	M_X	-0.0218
F_Y	-0.00215	M_Y	-7.6952
F_Z	440.814	M_Z	-6.852×10^{-19}

After identifying the equivalent loads, the specified column was deleted from the model, and the equivalent loads were applied to the joint previously attached to the column. The model with the column removed is shown in Figure 6.7. A static analysis of the model with the removed column and equivalent loads was performed to allow the structure to settle, with the responses from the simulation compared to the original model to confirm equivalency. Once the equivalency of the models was confirmed, the equivalent load was removed through the application of an equal and opposite force with a ramp time under $1/10^{th}$ of the structures 1^{st} vertical period. For the numerical model, the first vertical period is approximately 0.028 secs, leading to a removal time of 0.0025 secs. Once the element was removed, the structure was allowed to settle for 10 sec's. The envelope from the settled structure is shown in Figure 6.8 and 6.9.

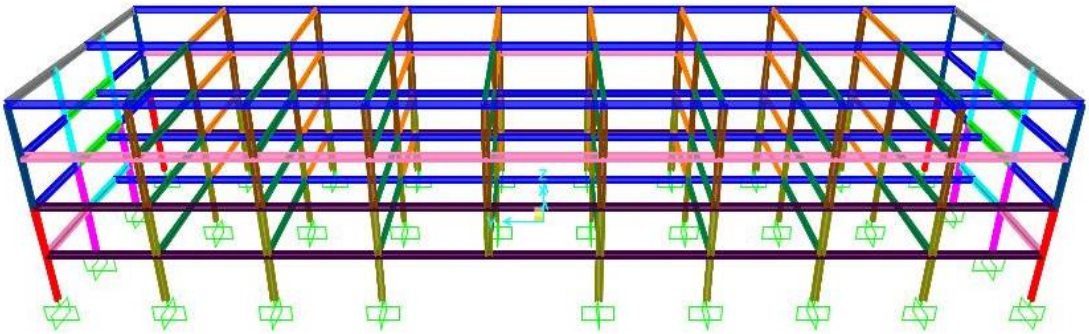

Figure 6.7 Element removal

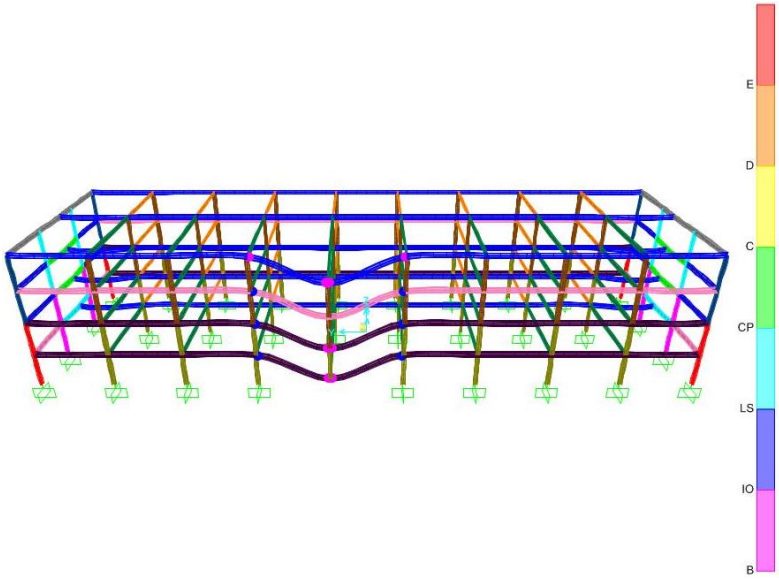

Figure 6.8 Envelope response for modified structure: 3-D view

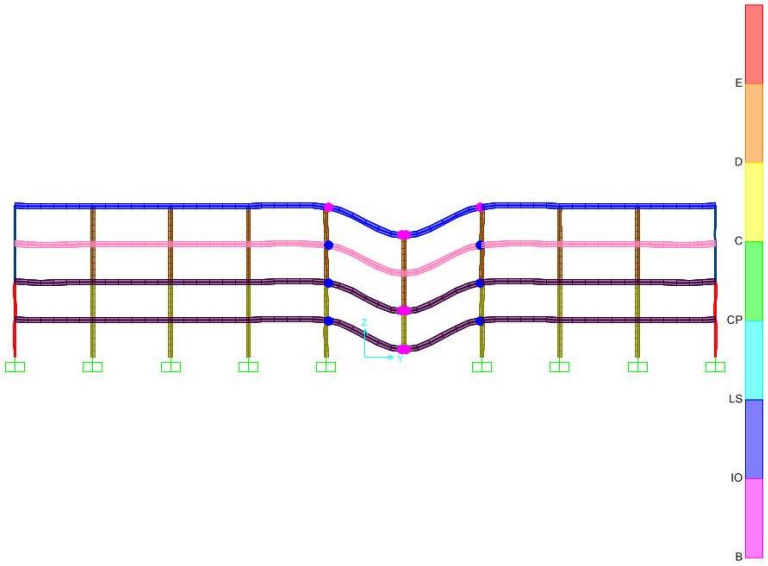

Figure 6.9 Envelope response for modified structure: 2-D view

In Figures 6.8-6.9, the plastic hinge conditions are shown in the legend. Magenta, yellow, orange and red represent locations on the plastic hinge moment-rotation backbone. Blue hinges represent exceedance of the immediate occupancy acceptance criteria, cyan hinges represent exceedance of the life safety acceptance criteria, and green hinges represent exceedance of the collapse prevention acceptance criteria. The progressive collapse potential can then be determined from the hinge envelope responses.

Blast Simulation

To simulate the impact of a blast on the modeled structure, a model of the frame structure previously described was built in the FE software Abaqus 6.13-2. The model used A992 steel with a Young's Modulus of 4176000 ksf, a density of 15.2297 lbs/ft^3, and a Poisson's ratio of 0.3. A Johnson-Cook material model was used to simulate the plastic behavior of the steel, which determines the stress-strain relationship of the material determined using the following equation,

$$\sigma = \left[A + B\varepsilon_{pl}^{n}\right][1 + C\ln\dot{\varepsilon}^{*}][1 - T^{*m}] \tag{6.6}$$

where A is the yield stress, B and n control the strain hardening, C is a strain-rate constant, m is a material constants, ε_{pl} is the equivalent plastic strain, T^* is the homologous temperature, and $\dot{\varepsilon}$ is the plastic strain rate [39], described by equation 6.7.

$$\dot{\varepsilon}^* = {\dot{\varepsilon}}/{\dot{\varepsilon}_o} \tag{6.7}$$

To calculate the damage in the model, the Johnson-Cook damage parameter was used. Element damage (D) was calculated as the accumulated plastic strain over the fracture strain using the following equation,

$$D = \sum \frac{\Delta\varepsilon_{pl}}{\varepsilon^f} \tag{6.8}$$

where ε^f is the equivalent fracture strain, determined from equation 6.9,

$$\varepsilon^f = \left[D_1 + D_2 e^{D_3\sigma^*}\right][1 + D_4 \ln \dot{\varepsilon}^*][1 - D_5 T^*] \tag{6.9}$$

where D_1, D_2, D_3, D_4, and D_5 are material constants, and σ^* is the effective stress [110]. Johnson-Cook strength and damage models have been frequently used to model steel under high strain rates, such due to blast loads [30, 35, 111]. Due to a lack of experimental material properties for A992 steel, the collection of material properties used by McConnell and Brown [35] to represent A992 steel were used in this work. The material properties are presented in Table 6.3. While damping can be neglected for blast simulations due to an undamped simulation creating a more conservative analysis, it was required for the model to settle after the application of the structural loads. Therefore, damping was modeled using 50% Rayleigh mass damping.

Table 6.3 Johnson-Cook material model parameters

Johnson-Cook Strength Model	Johnson-Cook Damage Model

A	7915579 ksf	D_1	0.05
B	3049273 ksf	D_2	3.44
C	0.0327	D_3	2.12
n	0.241	D_4	0.002
m	0	D_5	0.61
$\dot{\varepsilon}_o$	0.0057	$\dot{\varepsilon}_o$	1

Each frame element was modeled as a beam, with sections determined from the respective I-beam dimensions, and the transverse shear stiffness was specified by the elastic material properties. The column-foundation connections were modeled using a fixed boundary condition. To create the diaphragm constraint, the joints and frames on each floor were coupled to the center of the structure for the two horizontal translation DOF and the vertical rotation DOF. The Abaqus model of the modified frame is shown in Figure 6.10.

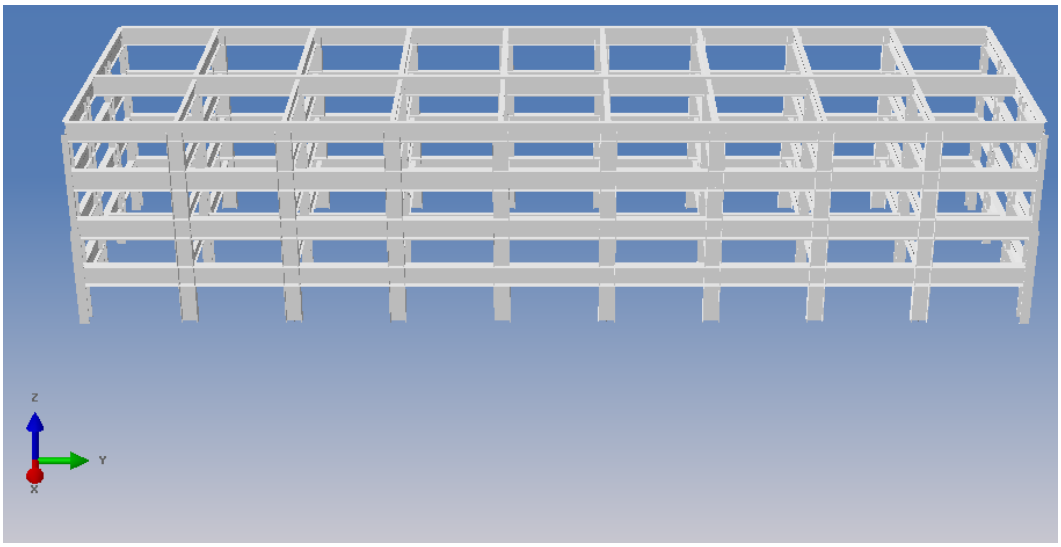

Figure 6.10 Abaqus frame model

To validate that the Abaqus model accurately represented the SAP2000 model, a modal comparison was performed. For the modal comparison, the Abaqus model used a mesh of one B31 linear element per frame, to correlate with the SAP2000 model. The first ten natural frequencies from each model are shown in Table 6.4. Due to the fact that the error for each mode was approximately 1% or lower, it was concluded that the Abaqus model represented the same structure as the SAP2000 model for the purposes of simulating damage from a blast.

Table 6.4 SAP2000 and Abaqus model natural frequencies

Mode Number	SAP2000 Model ω_n (Hz)	Abaqus Model ω_n (Hz)	Percent Error
1	2.257	2.259	0.08%
2	3.034	3.046	0.39%
3	3.043	3.071	0.92%
4	6.719	6.725	0.10%
5	8.336	8.413	0.92%
6	8.606	8.628	0.25%
7	12.015	12.060	0.38%
8	13.833	13.987	1.11%
9	14.729	14.785	0.38%
10	17.311	17.482	0.99%

To simulate the blast on the structure, the CONWEP blast codes were utilized. CONWEP is a set of blast equations, which are built into Abaqus as an incident wave interaction, which can be used to generate pressure loads equivalent to those from an explosion. The CONWEP pressure loads are based upon the charge equivalent TNT weight, detonation location, and type of explosion [112]. In this work, the numerical explosion was modeled as a surface blast. To provide an interface for the loads to be applied on,

steel cladding was modeled on one side of the frame structure. The cladding was modeled as an elastic material, with the density, Poisson's ratio, and Young's modulus previously described for the frame elements. Each cladding segment covered one bay of the model, and were modeled using homogeneous shell elements with a thickness of 0.03 ft. The cladding thickness was chosen to create a mass which matched the design cladding loads. The cladding loads at the locations where the cladding was modeled were then neglected. The edges of each cladding segment were tied to the relevant frame elements, with the cladding's base edges being pinned to the foundation. Each cladding segment was modeled using 12x12 S4R elements, with 12 B31 beam elements used for the connected frame elements. The rest of the frames elements were modeled with two B31 elements. The frame structure with the attached cladding is shown in Figure 6.11.

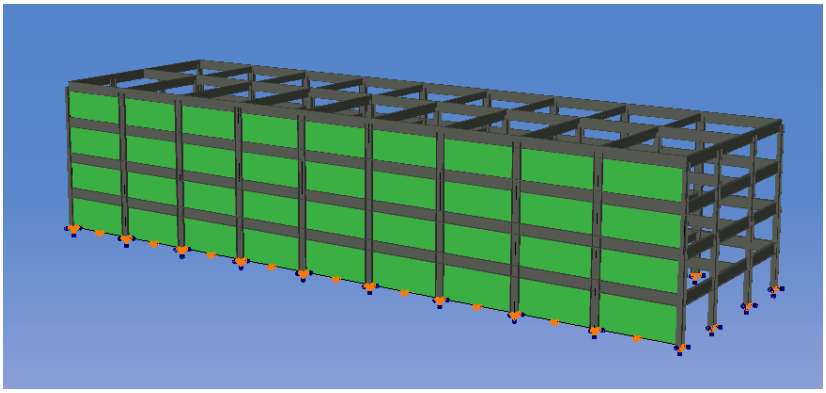

Figure 6.11 Frame structure with cladding in Abaqus

The numerical blast was simulated using an explicit analysis. The simulation began with the structural loads being applied as a ramp loading over 5 secs. After the loads were applied, the structure was allowed to settle for an additional 5 secs. At 10 secs into the simulation, the blast initiated. The pressures were calculated using a reference point for the explosive location, with the pressure loads applied to the exterior of the cladding. The response of the model to the blast loads was simulated for five seconds after the blast occurred, to ensure envelope responses were recorded.

Damaged Model

To create a model with representative damage from a blast, the damage from the Abaqus model was used to create a damaged SAP2000 model. The level of damage was determined using the Johnson-Cook damage parameter. Each column from the blast simulation was individually assessed, with the maximum damage parameter from the elements on the column dictating its damage level. If the maximum damage to a column was below 0.1, it was neglected for the damage assessment. Once the damage to each column was determined, it was transferred onto the SAP2000 model. Various researchers have used different damage indices to modify the yield stress, and the elastic and shear moduli [30, 113-116]. In this work, to demonstrate the impact of potential damage, modifications were applied to the SAP2000 model by changing the material of the damaged elements to a material which had the requisite reductions in elastic modulus, shear modulus, yield stresses, and ultimate stresses corresponding to the damage index, as shown in equation 6.10-6.13,

$$E_D = E(1 - D) \tag{6.10}$$

$$G_D = G(1 - D) \tag{6.11}$$

$$\sigma_{y,D} = \sigma_y(1 - D) \tag{6.12}$$

$$\sigma_{ult,D} = \sigma_{ult}(1 - D) \tag{6.13}$$

where E is the elastic modulus, $_D$ indicates the damaged value, G is the shear modulus, σ_y is the yield stress, and σ_{ult} is the ultimate stress. An example of the A992 material model from SAP2000 for the undamaged, and D = 0.5 conditions is shown in Figure 6.12 (a) and (b) respectively.

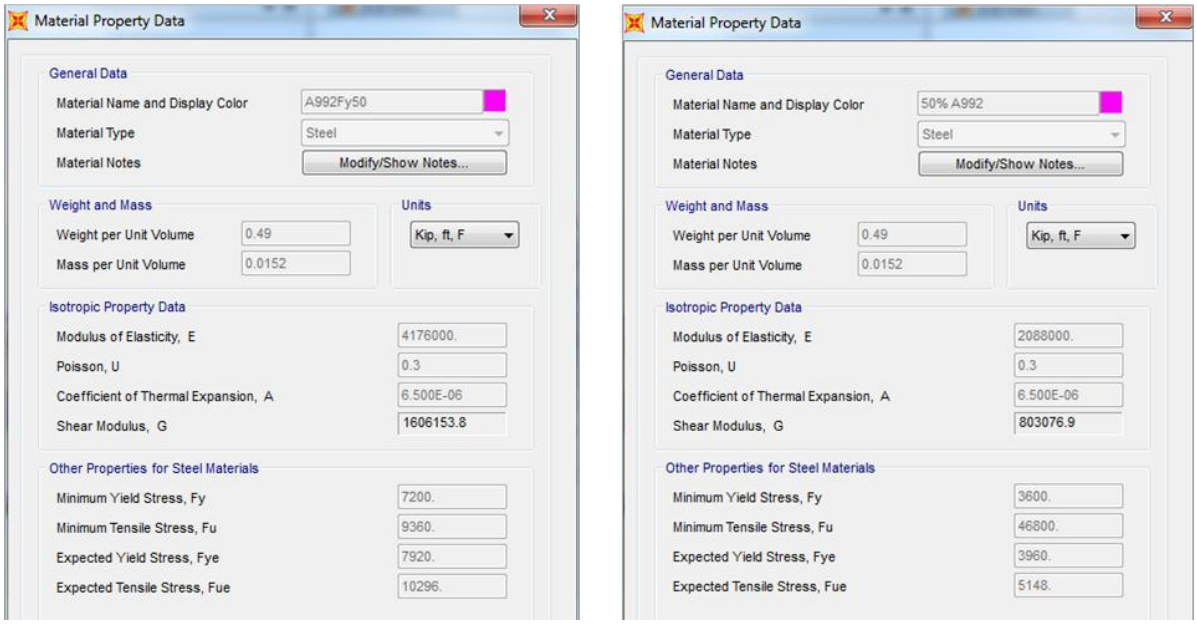

(a) A992 steel **(b) A992 steel with D = 0.5**

Figure 6.12 SAP2000 damage material modeling

6.4. Impact of Existing Damage on Performance of Building after Blast

To demonstrate the impact of additional damaged elements on the AP assessment, the elemental probabilities of failure were calculated using the SAP2000 structural model with different types of simulated damage, for the removal of column 21. The first assessment, scenario 1, was performed using the original model, as described in Section 6.3, to provide a baseline assessment for comparison. Scenario 2 utilized 50% damage to column 17, to show the impact on the elemental probability of failure due to damage to an adjacent column. Scenario 3 incorporated 50% damage to column 22, above the column for removal. Scenario 4 applied 50% damage to columns 22 and column 17, to show how multiple damage scenarios impact the elemental probability of failure. And scenario 5 utilized 50% damage to beam 217, to demonstrate the impact of damage on a beam connected to the element for removal. The different scenarios are summarized in Table 6.5. Damage was assessed as described in Section 6.3, with reductions in the elastic modulus, shear modulus, yield strength, and ultimate strength of the respective element(s).

Table 6.5 Damage scenarios for progressive collapse analysis

Scenario	Element Removal	Simulated Damage
1	Column 21	None
2	Column 21	Column 17 : D = 50%
3	Column 21	Column 22 : D = 50%
4	Column 21	Column 17 : D = 50% Column 22 : D = 50%
5	Column 21	Beam 217 : D = 50%

The envelope response for scenario 1, the undamaged structural model, after the removal of column 21 is shown in Figure 6.13, with the undamaged elements shown in grey. The elemental probability of failure for each hinge with plastic rotation was assessed, and is shown in Table 6.6. The hinge numbering corresponds to the values shown Figure 6.3. The maximum elemental probability of failure is seen to lie with beam 221, at 19.11%, which governs the assessment for the entire model.

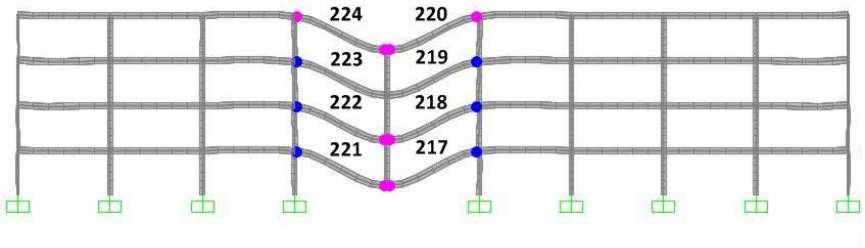

Figure 6.13 Envelope response for scenario 1

Table 6.6 Elemental probability of failure for scenario 1

Element Number	Hinge Number	Elemental Probability of Failure (%)
217	1	19.10%
217	3	1.00%
218	1	18.51%
218	3	0.50%
219	1	9.59%
220	1	4.59%
220	3	1.97%
221	1	0.99%
221	3	19.11%
222	1	0.48%
222	3	18.49%
223	3	9.58%
224	1	1.94%

The response of the structure for scenario 2 after the removal of column 21 is shown in Figure 6.14, with the undamaged elements shown in grey, and the damaged element shown in red. The probability of failure for each hinge with plastic rotation was assessed, and is shown in Table 6.7. The maximum elemental probability of failure is seen to lie with column 17, at 66.89%, which governs the assessment for the whole model. While the probability of failure for each beam is approximately the same or reduced from scenario 1, the addition of damage to column 17 leading to a force-controlled response, causing the increased probability of failure.

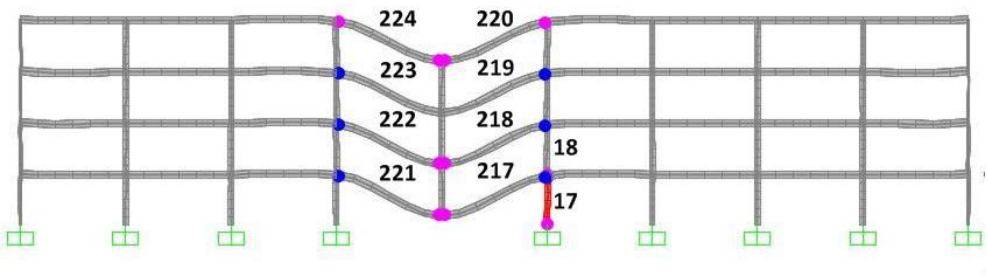

Figure 6.14 Envelope response for scenario

Table 6.7 Elemental probability of failure for scenario 2

Element Number	Hinge Number	Elemental Probability of Failure (%)
17	1	65.67%
17	2	66.89%
18	1	5.02%
217	1	14.96%
217	3	0.65%
218	1	18.60%
218	3	0.25%
219	1	9.34%
220	1	4.40%
220	3	1.87%
221	1	1.20%
221	3	19.58%
222	1	1.20%
222	3	19.18%
223	3	9.98%
224	1	2.25%
224	3	4.84%

The envelope response of the structure from scenario 3 after the removal of column 21 is shown in Figure 6.15. The probability of failure for each hinge with plastic rotation was assessed, and is shown in Table 6.8. The maximum probability of failure is seen to occur for beams 217 and 221, at 19.23%, which governs the assessment for the whole model. The damage to the column on the second floor did not lead to increased plastic rotation of the columns, and little change in the load transfer to the beams. Therefore, there was only a slight change in the elemental probability of failure.

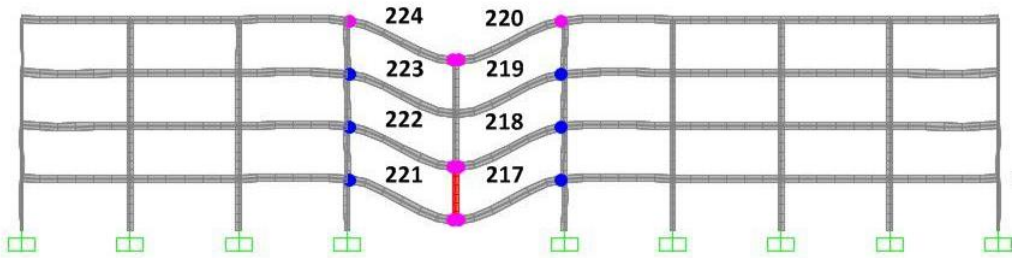

Figure 6.15 Envelope response for scenario 3

Table 6.8 Elemental probability of failure for scenario 3

Element Number	Hinge Number	Elemental Probability of Failure (%)
217	1	19.23%
217	3	1.13%
218	1	18.64%
218	3	0.64%
219	1	9.69%
220	1	4.65%
220	3	2.04%
221	1	1.12%
221	3	19.23%
222	1	0.62%
222	3	18.62%
223	3	9.67%
224	1	2.00%
224	3	4.62%

Scenario 4's envelope response after the removal of column 21 is shown in Figure 6.16. The probability of failure for each hinge with plastic rotation was assessed, and is shown in Table 6.9. The maximum probability of failure is seen to lie with column 17, at 70.89%, which governs the assessment for the whole model. While the damage to column 22 alone did not significantly impact the elemental probabilities of failure, coupled with the damaged column adjacent to the element removal, there was an increase in the maximum elemental probability of failure, as increased moments were applied to column 17 due to the damage in column 22.

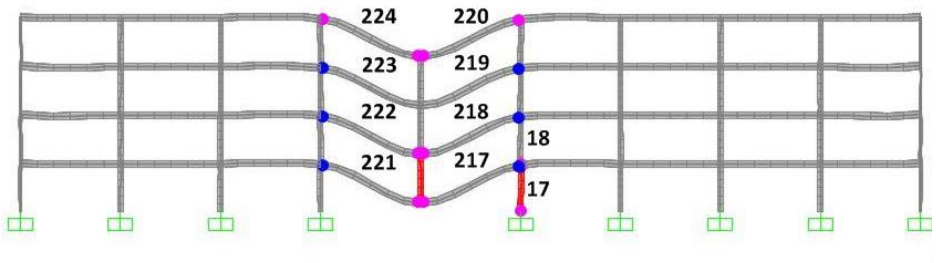

Figure 6.16 Envelope response for scenario 4

Table 6.9 Elemental probability of failure for scenario 4

Element Number	Hinge Number	Elemental Probability of Failure (%)
17	1	65.35%
17	2	70.89%
18	1	5.11%
217	1	15.08%
217	3	0.87%
218	1	18.73%
218	3	0.39%
219	1	9.44%
220	1	4.46%
220	3	1.94%
221	1	1.72%
221	3	19.72%
222	1	1.33%
222	3	19.32%
223	3	10.07%
224	1	2.32%
224	3	4.90%

The response of the structure for scenario 5 after the removal of column 21 is shown in Figure 6.17. The calculated probability of failure for each hinge with plastic rotation was assessed, and is shown in Table 6.10. The maximum probability of failure is seen to lie with beam 222, at 33.65%, governing the assessment for the whole model. The damage to the beam adjacent to the column removal lead to a significant change in load transfer, causing an increase in the probability of failure in the majority of the plastic hinges.

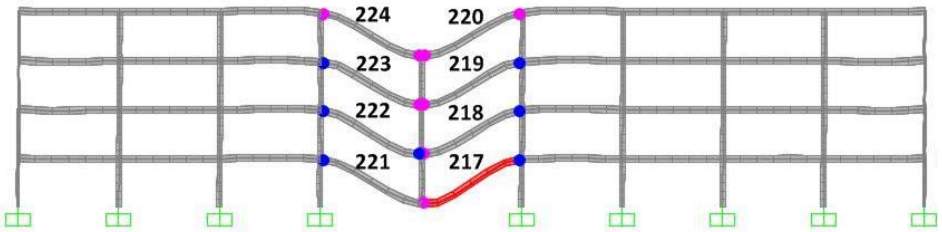

Figure 6.17 Envelope response for scenario 5

Table 6.10 Elemental probability of failure for scenario 5

Element Number	Hinge Number	Elemental Probability of Failure (%)

217	1	25.35%
217	3	3.20%
218	1	32.85%
218	3	5.19%
219	1	15.43%
219	3	2.59%
220	1	8.69%
220	3	5.39%
221	3	31.43%
222	1	11.74%
222	3	33.65%
223	1	2.22%
223	3	15.51%
224	1	5.75%
224	3	8.77%

From the presented analyses, the maximum probability of failure for scenario 1 was calculated at 19.11%. Damage to columns on the base, near the column for removal, lead to a 47.78% increase in the maximum probability of failure, as the governing element changed from beam 221 to column 17. Damage to the column directly above the removed element did not cause a drastic change in the elements probability of failure. However, damage to the column directly above the removed element did modify the load transfer when coupled with additional damage to columns on the structures base, as shown by the 4% increase in the maximum probability of failure from scenario 2 to 4. Damage to the beams caused a significant change in load transfer, leading to larger hinge rotations and 14.54% increase in maximum elemental probability of failure. Changes in the elemental probability of failure with damage to beams, in the context of potential

for progressive collapse, could be useful for future study, especially for the impact of potential post-blast fires on structural safety.

6.5. Results

Blast Simulation

A numerical blast with an equivalent TNT weight of 1775 lbs was chosen to demonstrate the model updating procedure and adaptive alternate path methodology. The location of the explosion was chosen to be on the ground, 5 ft back from the exterior of the structure in line with column 21 which was the column removed in Figure 6.6. The blast location is indicated by the explosion icon in Figure 6.18. The explosion began at 10 secs, with an example of the pressure applied to the structure shown in Figure 6.19, where (a) shows the pressure loads on the structure at 10.015 secs, and (b) shows the pressure time-history at the top of column 21.

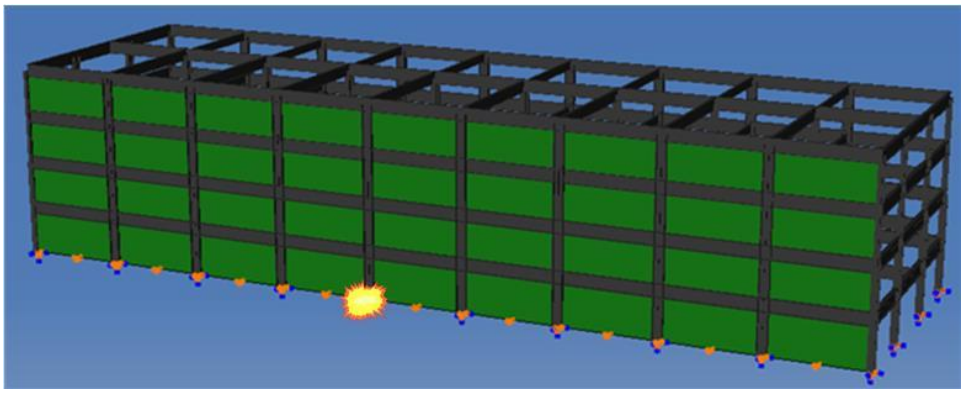

Figure 6.18 Simulated blast location

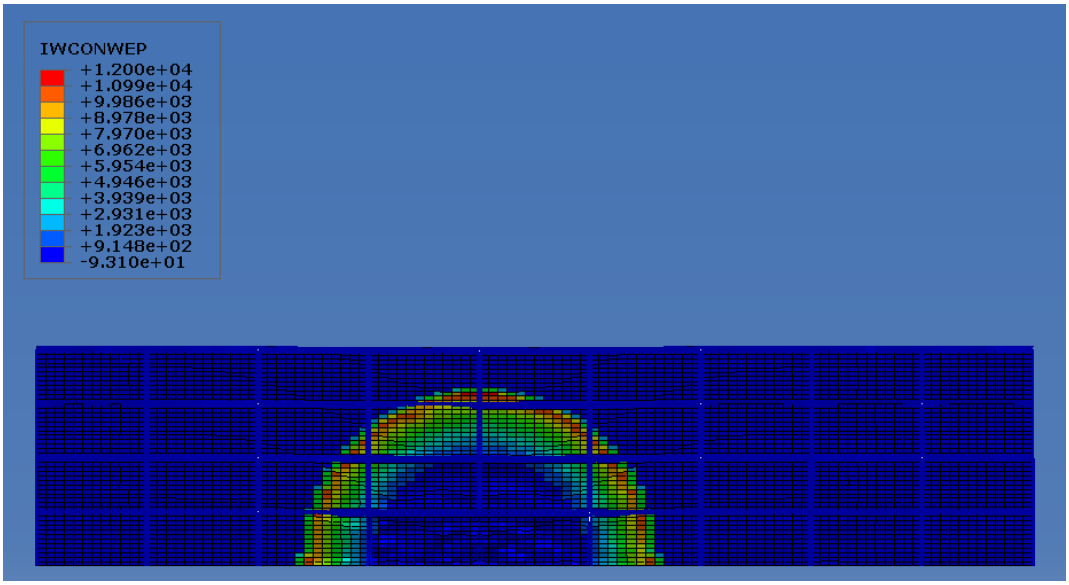

(a) Pressure contour at 10.015 secs

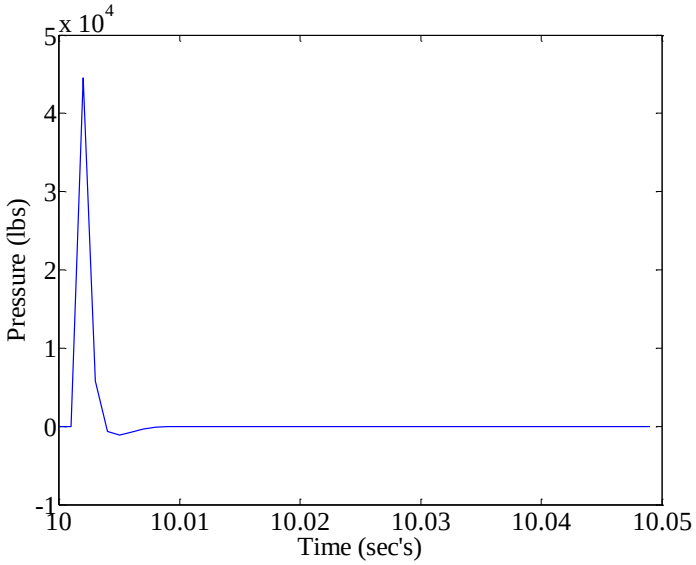

(b) Pressure Time history at the top of column 21

Figure 6.19 Blast pressure for numerical simulation

The Johnson-Cook damage parameters at the end of the simulation are shown in Figure 6.20. The maximum damage parameter per column was determined from the unique nodal elements attached to the element. The maximum damage parameter on each damaged column is presented in Table 6.11, with the

column numbers corresponding to Figure 6.5. Using the identified elemental damage index, a damaged SAP2000 model was created using the methodology described in Section 6.3.

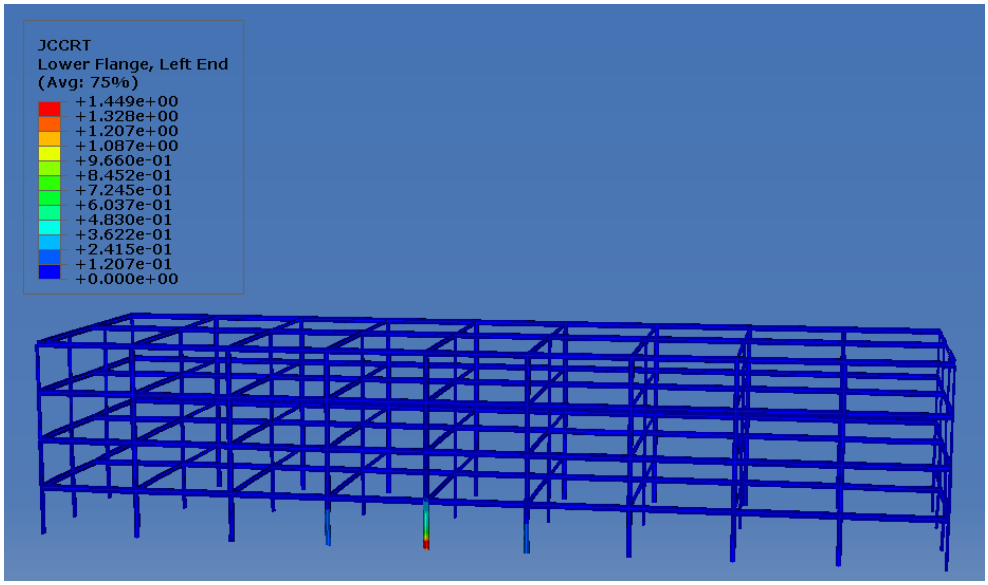

Figure 6.20 Post-blast Johnson-Cook damage index

Table 6.11 Damage from blast simulation

Column Number	17	21	22	25	26
Maximum Damage Parameter	0.229	Removed	0.510	0.214	0.109

Once the damaged model was created, the alternate path assessment was performed to determine the elemental probabilities of failure. As column 21 had a damage index over the threshold of 0.8, it was removed in the analysis. From the alternate path safety assessment, the maximum elemental probability of failure for the damaged model was determined to be 93.3%, with the elemental probabilities of failure shown in Table 6.12. The envelope displacement of the damaged model after the adaptive alternate path assessment is shown in Figure 6.21.

Table 6.12 Elemental probability of failure for damage model

Element Number	Hinge Number	Elemental Probability of Failure (%)
17	2	13.61%
25	2	93.30%
26	1	1.87%
217	1	17.74%
217	3	1.24%
218	1	19.05%
218	3	0.85%
219	1	9.79%
220	1	4.72%
220	3	2.15%
221	1	1.34%
221	3	17.09%
222	1	0.80%
222	3	18.59%
223	3	9.75%
224	1	2.08%
224	3	4.65%

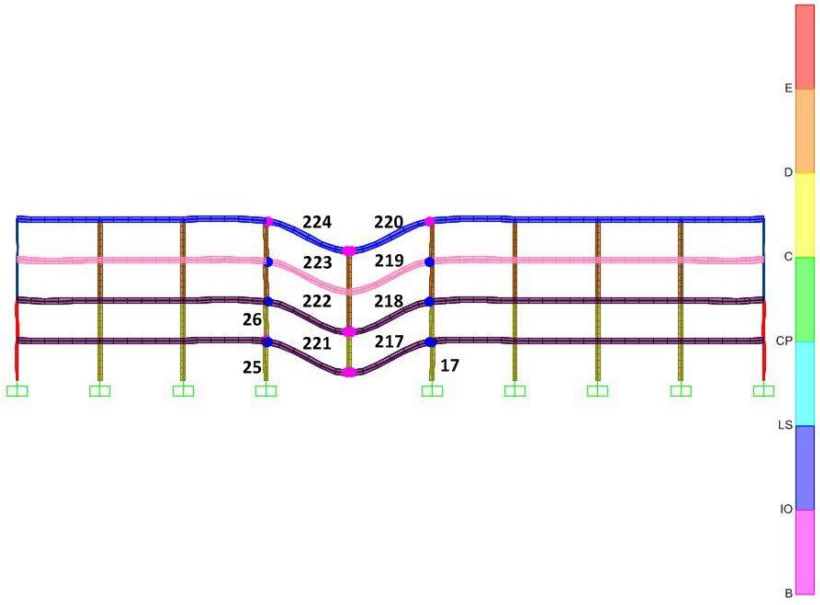

Figure 6.21 Envelope response for damaged structure

Model Updating

Once the damaged model was created, the natural frequencies and mode shapes were determined from the eigenvalues and eigenvectors of its stiffness and mass matrices. For the model updating, a reduced model was created using Guyan condensation to the displacement DOF. The first 38 modes, which corresponded to the modal participation ratio of the reduced model exceeding 92%, were used for the model updating, with a maximum natural frequency of 38.27 Hz. Updating was performed using the two phase localization and quantification method previously discussed. The localization used a stiffness threshold of -0.1%, and the quantification GA used the parameters shown in Table 6.13. The columns selected for updating, as well as the calculated damage per column are shown in Table 6.14. There are minor quantification errors between the damage used in the SAP2000 model, and the quantified damage. This is likely due to minor differences in the model generation from SAP2000, and the method used in the model updating. However, as the differences in the actual and quantified damage are under 6.5%, it was determined that the quantification was accurate enough to create the equivalent structural model.

Table 6.13 Quantification genetic algorithm parameters

Parameter	Value	Parameter	Value
GA Iterations	4	Mutation Reduction Iterations	20
Population	210	Minimum Mutation Percentage	10%
Parent Percentage	10%	Convergence Iterations	70
Mutation Percent	15%	Convergence Threshold	$1x10^{-8}$
Mutation Reduction Rate	25%		

Table 6.14 Updated column damage

Column Number	Quantified Damage (%)	Actual Damage (%)	Error (%)
17	19.89%	22.90%	-3.01%
18	6.46%	0.00%	6.46%
21	99.99%	100.00%	-0.01%
22	49.42%	51.00%	-1.58%
25	21.78%	21.40%	0.38%
26	8.66%	10.90%	-2.24%
27	2.66%	0.00%	2.66%

Adaptive Alternate Path Safety Assessment

The damage quantified from the model updating was used to generate an equivalent damaged model in SAP2000 through modification of the elemental material properties using the quantified damage. The adaptive alternate path assessment was then performed on the updated model. As the damage quantified in column 21 had a damage level over the threshold limit of 80%, it was removed in the adaptive alternate path analysis. The envelope displacement of the equivalent damaged model after the adaptive alternate path

assessment is shown in Figure 6.22. From the adaptive alternate path safety assessment, the maximum elemental probability of failure was determined to be 92.97%, with the elemental probabilities of failure shown in Table 6.15. The maximum elemental probability of failure from the equivalent model was very close to the value from the damage model, with a difference of only 0.33%, showing the applicability of the updated model for the probability of failure assessment.

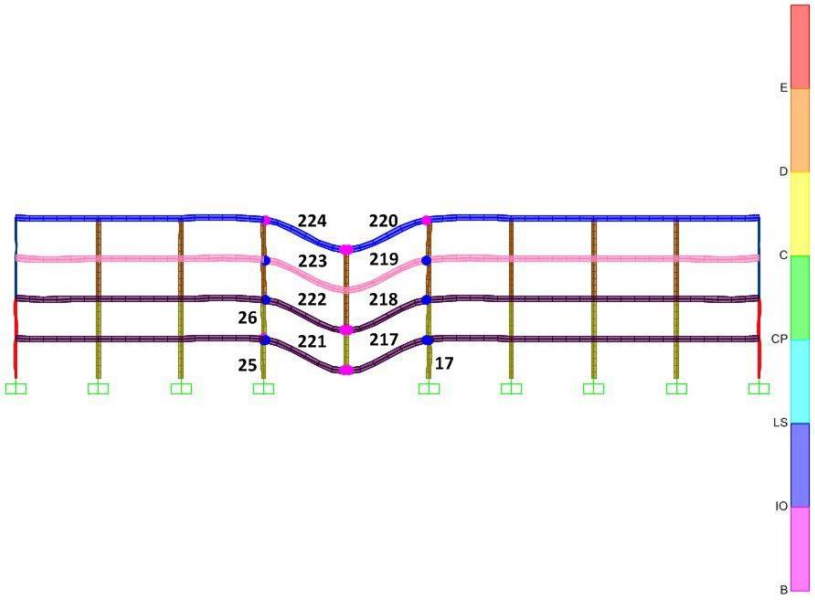

Figure 6.22 Envelope response for equivalent damaged structure

Table 6.15 Equivalent damage model elemental probability of progressive collapse

Element Number	Hinge Number	Elemental Probability of Failure (%)
17	2	10.88%
25	2	92.97%
26	1	0.50%
217	1	17.85%
217	3	1.32%
218	1	18.81%
218	3	0.86%
219	1	9.80%
220	1	4.71%
220	3	2.14%
221	1	1.30%
221	3	17.37%
222	1	0.78%
222	3	18.70%
223	3	9.75%
224	1	2.08%
224	3	4.66%

6.6. Discussion

The adaptive alternate path method has the potential to determine the elemental probability of failure for a structure after a blast. This information can be used to determine if additional elements in the structure are near failure, which could signal an imminent progressive collapse. By using a numerical model updated from the post-event structures measurements, the impact of the damage from the blast on the structure is incorporated into the analysis. As shown in Section 6.4, additional damage to elements can lead to significant increases in the maximum elemental probability of failure. This is particularly true for base columns and beams, which saw large increases in the maximum elemental probability of failure due to the introduction of damage. Additionally, multiple damaged elements can couple to increase the structures maximum elemental probability of failure.

The benefits of using updated numerical models to represent the damaged structure was shown in Section 6.5, where the damage was simulated using a numerical blast. Model updating from the natural frequencies and mode shapes of the damaged numerical model, such as could be gathered post-blast, were used to create an equivalent structural model. The maximum elemental probability of failure using the equivalent model was within 0.33% of the actual damage model. The close match shows its capability for use in assessing a post-event structural condition. The updated elemental probability of failure can then be used by emergency responders, to assess the condition of structure, and determine safe courses of action.

6.7. Conclusions

In this chapter, the adaptive alternate path assessment was presented. The methodology uses model updating to incorporate additional damage on a structure into the alternate path analysis. The adaptive alternate path analysis determined the elemental probability of failure for elements subjected to plastic deformation. As the successive failure of elements due to an inability to transfer the loads after a local failure occurs during a progressive collapse, elemental probability of failure can be used to as a safety measure for potential progressive collapse. The incorporation of damage beyond element failure from the blast into the analysis

can lead to significantly higher probabilities of failure, particularly for ground floor columns and beams. Multiple instances of additional damage can also lead to increased probabilities of failure of the elements. To validate the methodology for post-blast structures, representative damage to a structure from a blast was simulated. An equivalent model of the damaged structure was then generated, using the two-phase damage localization and quantification methodology. The low error between the equivalent and damaged elemental probabilities of failure demonstrates the capability of using measurements from a damaged structure to create an equivalent damaged model, and assessing the structures elemental probability of failure after a blast from the equivalent model. The elemental probability of failure can be used by emergency responders to determine safe courses of action in terms of evacuation assistance and operation logistics after the blast, giving them the ability to save lives with the lowest risk to their own.

7. CONCLUSIONS AND FUTURE WORK

7.1. Conclusions

With the rising threat to structures from explosions, understanding a structures safety from a blast is of increasing importance. Before a blast occurs, understanding the structures vulnerability can be used to develop acceptable levels of risk. After the blast, understanding the structures probability of failure can be used to inform safe emergency operations. Structural health monitoring (SHM) has the capability to develop these assessments. However, SHM applications for blast safety assessments have to be able to compensate for the limited number of available sensors available for monitoring, and be able to handle likely malfunctions from some sensors due to the blast event.

Chapter 3 presented a novel method to use model updating to generate updated P-I diagrams. The updated numerical models reflected additional damage to the structure, the impacts of which are incorporated into the P-I diagrams. The additional damage can reduce the pressure and impulse for each limit, or damage state. The method was validated using experimental SDOF and MDOF structures subjected to damage, with P-I diagrams generated from the updated numerical models. Structural stakeholders can use the updated P-I diagrams to assess the structures current risk, and design appropriate security or retrofit measurers to maintain their acceptable risk levels.

When a blast occurs, there is a high potential for damaged sensors due to the extreme event. Therefore, SHM on a post-blast structure needs to be able to account for damaged or malfunctioning sensors. A two-phase remaining stiffness localization and quantification method was presented in Chapter 4, utilizing the ease of direct model updating to localize damage and iterative parameter optimization to quantify the modifications, to estimate damage with missing sensors. Numerical and experimental validation of the methodology was presented for estimating damage to buildings with malfunctions of the 1st floor sensors. Such a method has the potential to quantify damage to a structure after a blast.

For most SHM applications, the number of available sensors for monitoring is usually significantly less than the number of potential monitoring locations. SHM for damage estimation needs to be able to assess parameter modifications using limited sensors networks. To maximize the parameter modification estimations, two OSP methods were used to improve the two phase parameter localization and quantification method with a limited number of sensors in Chapter 5. Experimental testing was used to demonstrate the parameter estimation with the limited sensor networks. It was shown that quantification was possible with the reduced number of sensors, with the EI OSP method providing the better estimations.

After a blast, if the structure has not failed, determining the probability of failure of the structural elements can be used to assess if a progressive collapse of the structure is imminent. This information can be of use to emergency responders to plan an efficient and safe emergency response. The adaptive alternate path method, presented in Chapter 6, determines the elemental probability of failure using a post-blast updated, equivalent model. The adaptive alternate path analysis utilizes the updated numerical model, which incorporates additional damage beyond failed elements. A numerical analysis was performed, showing increases in the elemental probability of failure due to additional elemental damage. The application of the model updating after a blast was demonstrated using a numerical blast, establishing how the model updating creates an equivalent model with similar probabilities of failure to the damaged structure. This method can be used with sensor networks on critical infrastructure to provide structural safety assessments after a blast occurs.

In this dissertation SHM was utilized to create updated P-I diagrams which accounted for structural damage, and to develop post-blast probability of failure assessments for damaged structures. To account for missing and limited amounts of sensors, a method was developed to quantify structural modifications using limited measurements with OSP, and a novel method was shown to estimate structural remaining stiffness with malfunctioning sensors. The preliminary vulnerability assessments can be used to design security measures or retro-fit structures to maintain acceptable levels of risk with structural variations. OSP methods can be used locate a limited number of sensors on a structure and produce improved accuracy for the parameter estimations. Quantifying the structural remaining stiffness with missing measurements is

important to facilitate structural assessments after a blast, where sensors are likely to be damaged. And, the post-event elemental probability of failures from the adaptive alternate path analysis can be used to develop a safe and effective emergency response after a blast occurs. The work performed in this dissertation can be used to mitigate the risk of structural damage from potential blasts, and reduce the risk of harm to emergency personnel after a blast occurs.

7.2. Future Work

Preliminary Blast Safety Assessment Expansion

The development of P-I diagrams accounting for the current condition of the structure can be expanded upon by utilizing more detailed updating methods, which improve the P-I diagrams. Additional large scale experimental validation of the updating, as well as of the safety assessments generated from the P-I diagrams to experimental blasts would be beneficial.

Comparison of Capability of OSP methods for SHM Expansion

Evaluating the capability of the presented parameter modification methodology using limited sensor networks developed with additional OSP methods can be used to determine which OSP sensor networks provide the best parameter estimates. Additional research should be performed using parameter quantification with OSP sensor networks on different types of structures, such as bridges.

Impact of Measurement Noise on Parameter Estimation

While signal noise was inherent in the experimental measurements, as the testing was performed in a laboratory setting, it can be assumed that the levels were low. In field applications, large levels of signal noise can be experienced. A study on the impact of varying levels of signal noise on parameter estimations with a limited number of sensors could provide information on the expected errors for different applications.

Adaptive Alternate Path Method Experimental Validation

Experimental validation of the adaptive alternate path method would be necessary to justify its use in real structures. Experimental testing needs to be performed to validate the acceptance criteria for failure instead of for design, to justify the validity of the experimental damage quantifications, and to determine which parameters to update in the parameter quantification to best represent the real-life damage from a blast.

Adaptive Alternate Path Method for Damage to Connections

After a blast, severe damage can occur at the connections. Expansion of the model updating, with accompanying validation, to account for damage at element connections may provide more realistic assessments of the post-blast structural condition.

Adaptive Alternate Path Method for Additional Hazards

The adaptive alternate path method is threat independent, presenting a potential for use with different types of hazardous events. Assessing the adaptive alternate path assessment's capability for different types of hazards, as well as for different types of structures can provide applicability for a wide variety of scenarios.

System Level Probability of Failure for Adaptive Alternate Path Method

The probability of failure in the adaptive alternate path method currently only assesses individual elements. While individual element failure is a component of progressive collapse, it does not necessarily mean progressive collapse will occur. Expansion of the current assessments to system level probability of failure would be beneficial.

8. REFERENCES

[1] Pape, R., Mniszewski, K. R. and Longinow, A. (2009). "Explosion phenomena and effects of explosions on structures. I: Phenomena and effects." *Pract.Periodical Struct.Des.Constr.*: 15(2): pp. 135-140.

[2] Marjanishvili, S. (2004). "Progressive analysis procedure for progressive collapse." *J.Perform.Constr.Facil.*: 18(2): pp. 79-85.

[3] Fu, F. (2013). "Dynamic response and robustness of tall buildings under blast loading." *Journal of Constructional steel research*: 80: pp. 299-307.

[4] Tsai, M. (2012). "Assessment of analytical load and dynamic increase factors for progressive collapse analysis of building frames." *Adv.Struct.Eng.*: 15(1): pp. 41-54.

[5] Bounds, W. L. (2010). [Design of Blast-Resistant Buildings in Petrochemical Facilities], *ASCE Publications*.

[6] Ngo, T., Mendis, P., Gupta, A. and Ramsay, J. (2007). "Blast loading and blast effects on structures–an overview." *Electronic Journal of Structural Engineering*: 7: pp. 76-91.

[7] Birnbaum, N. K., Clegg, R. A., Fairlie, G. E., Hayhurst, C. J. and Francis, N. J. (1996). "Analysis of blast loads on buildings." *Preprint from Structures Under Extreme Loading Conditions*.

[8] Chege, J. and Matalanga, N. (2000). "NDT application in structural integrity evaluation of bomb blast affected buildings." *Proc. 15th World Conference on Nondestructive Testing, Italy*.

[9] *Stabilization of Buildings Workshop* (2009) Vicksburg, MS.

[10] *Monitoring and Sensing of Near-Collapse Buildings Workshop* (2010) Oxford, MS.

[11] DoD (2013). *Unified Facilities Criteria: Design of Buildings to Resist Progressive Collapse.*, United States Department of Defense.

[12] Rao, A. and Anandakumar, G. (2008). "Optimal sensor placement techniques for system identification and health monitoring of civil structures." *Smart Structures and Systems*: 4(4): pp. 465-492.

[13] Corley, W. G. (2004). "Lessons learned on improving resistance of buildings to terrorist attacks." *J.Perform.Constr.Facil.*: 18(2): pp. 68-78.

[14] Dusenberry, D. O. (2010). [Handbook for Blast-Resistant Design of Buildings], *Wiley Online Library*.

[15] Lefter, J. (2010). "Mitigating terrorist attacks and earthquake risk: International building code revisions can provide solutions." *Structure*: pp. 49-50.

[16] National Counterterrorism Center (2008). *2007 Report on Terrorism.*, National Counterterrorism Center.

[17] National Counterterrorism Center (2009). *2008 Report on Terrorism.*, National Counterterrorism Center.

[18] National Counterterrorism Center (2007). *Report on Terroist Incidents - 2006.*, National Counterterrorism Center.

[19] Kim, H., Kim, J. and An, D. (2009). "Development of integrated system for progressive collapse analysis of building structures considering dynamic effects." *Adv.Eng.Software*: 40(1): pp. 1-8.

[20] Bounds, W. L. (2010). [Design of Blast-Resistant Buildings in Petrochemical Facilities], *ASCE Publications*.

[21] Smith, P. D. and Hetherington, J. G. (1994). [Blast and Ballistic Loading of Structures], *Digital Press*.

[22] Baker, W. E. (1973). [Explosions in Air], *University of Texas press*.

[23] Applied Research Associates, I.*AT Blast Version 1.0* (1998) Vicksburg, MS.

[24] DoD (2014). *Unified Facilities Criteria : Structures to Resist the Effects of Accidental Explosions.*, United States Department of Defense.

[25] ASCE (2011). [Blast Protection of Buildings (59-11)], *American Society of Civil Engineers*, Reston, Virginia.

[26] Dragos, J., Wu, C., Haskett, M. and Oehlers, D. (2012). "Derivation of normalized pressure impulse curves for flexural ultra high performance concrete slabs." *J.Struct.Eng.*: 139(6): pp. 875-885.

[27] Fallah, A., Nwankwo, E. and Louca, L. (2013). "Pressure-impulse diagrams for blast loaded continuous beams based on dimensional analysis." *Journal of Applied Mechanics*: 80(5): pp. 051011.

[28] Li, Q. and Meng, H. (2002). "Pressure-impulse diagram for blast loads based on dimensional analysis and single-degree-of-freedom model." *J.Eng.Mech.*: 128(1): pp. 87-92.

[29] Shi, Y., Li, Z. and Hao, H. (2010). "A new method for progressive collapse analysis of RC frames under blast loading." *Eng.Struct.*: 32(6): pp. 1691-1703.

[30] Ding, Y., Wang, M., Li, Z. and Hao, H. (2013). "Damage evaluation of the steel tubular column subjected to explosion and post-explosion fire condition." *Eng.Struct.*: 55: pp. 44-55.

[31] Lu, Y. and Wang, Z. (2006). "Characterization of structural effects from above-ground explosion using coupled numerical simulation." *Comput.Struct.*: 84(28): pp. 1729-1742.

[32] Kinney, G. and Kenneth, J. (1985). [Explosive Shocks in Air], *New York: Springer-Verlag*, New York, 84.

[33] Krauthammer, T., Astarlioglu, S., Blasko, J., Soh, T. and Ng, P. (2008). "Pressure–impulse diagrams for the behavior assessment of structural components." *Int.J.Impact Eng.*: 35(8): pp. 771-783.

[34] Islam, A. A. and Yazdani, N. (2008). "Performance of AASHTO girder bridges under blast loading." *Eng.Struct.*: 30(7): pp. 1922-1937.

[35] McConnell, J. R. and Brown, H. (2011). "Evaluation of progressive collapse alternate load path analyses in designing for blast resistance of steel columns." *Eng.Struct.*: 33(10): pp. 2899-2909.

[36] Tang, E. K. and Hao, H. (2010). "Numerical simulation of a cable-stayed bridge response to blast loads, Part I: Model development and response calculations." *Eng.Struct.*: 32(10): pp. 3180-3192.

[37] Son, J. and Lee, H. (2011). "Performance of cable-stayed bridge pylons subjected to blast loading." *Eng.Struct.*: 33(4): pp. 1133-1148.

[38] Winget, D. G., Marchand, K. A. and Williamson, E. B. (2005). "Analysis and design of critical bridges subjected to blast loads." *J.Struct.Eng.*: 131(8): pp. 1243-1255.

[39] Johnson, W. (1983). "Aspects of damage to buildings from uncased explosives." *Mechanics of Material Behavior(The Daniel C.Drucker Anniversary*: pp. 175-190.

[40] Ellingwood, B. R., Smilowitz, R., Dusenberry, D. O., Duthinh, D., Lew, H. and Carino, N. J. (2007). [Best Practices for Reducing the Potential for Progressive Collapse in Buildings], *US Department of Commerce, National Institute of Standards and Technology*.

[41] Gamaniouk, T. (2014). "Parametric Analysis of Progressive Collapse in High-Rise Buildings." *Massachusetts Institute of Technology*.

[42] Marjanishvili, S. and Agnew, E. (2006). "Comparison of various procedures for progressive collapse analysis." *J.Perform.Constr.Facil.*: 20(4): pp. 365-374.

[43] McKay, A., Marchand, K. and Diaz, M. (2012). "Alternate path method in progressive collapse analysis: Variation of dynamic and nonlinear load increase factors." *Pract.Periodical Struct.Des.Constr.*: 17(4): pp. 152-160.

[44] General Services Administration (GSA) (2013). *Alternate Path Analysis & Design Guidelines for Progressive Collapse Resistance.*

[45] Kim, J. and Kim, T. (2009). "Assessment of progressive collapse-resisting capacity of steel moment frames." *Journal of Constructional Steel Research*: 65(1): pp. 169-179.

[46] Tsai, M. and Lin, B. (2008). "Investigation of progressive collapse resistance and inelastic response for an earthquake-resistant RC building subjected to column failure." *Eng.Struct.*: 30(12): pp. 3619-3628.

[47] Hao, H. and Tang, E. K. (2010). "Numerical simulation of a cable-stayed bridge response to blast loads, Part II: Damage prediction and FRP strengthening." *Eng.Struct.*: 32(10): pp. 3193-3205.

[48] Sasani, M., Kazemi, A., Sagiroglu, S. and Forest, S. (2011). "Progressive collapse resistance of an actual 11-story structure subjected to severe initial damage." *J.Struct.Eng.*: 137(9): pp. 893-902.

[49] Kazemi-Moghaddam, A. and Sasani, M. (2015). "Progressive collapse evaluation of Murrah Federal Building following sudden loss of column G20." *Eng.Struct.*: 89: pp. 162-171.

[50] Jiang, H., Wang, J., Chorzepa, M. G. and Zhao, J. (2017). "Numerical Investigation of Progressive Collapse of a Multispan Continuous Bridge Subjected to Vessel Collision." *J.Bridge Eng.*: 22(5): pp. 04017008.

[51] Brownjohn, J. M. (2007). "Structural health monitoring of civil infrastructure." *Philos.Trans.A.Math.Phys.Eng.Sci.*: 365(1851): pp. 589-622.

[52] Carden, E. P. and Fanning, P. (2004). "Vibration based condition monitoring: a review." *Structural health monitoring*: 3(4): pp. 355-377.

[53] Salehi, M., Rad, S. Z., Ghayour, M. and Vaziry, M. (2011). "A non model-based damage detection technique using dynamically measured flexibility matrix." *Iranian Journal of Science and Technology.Transactions of Mechanical Engineering*: 35(M1): pp. 1-13.

[54] Yan, Y., Cheng, L., Wu, Z. and Yam, L. (2007). "Development in vibration-based structural damage detection technique." *Mechanical Systems and Signal Processing*: 21(5): pp. 2198-2211.

[55] Alvandi, A. and Cremona, C. (2006). "Assessment of vibration-based damage identification techniques." *J.Sound Vibrat.*: 292(1): pp. 179-202.

[56] Pandey, A. and Biswas, M. (1994). "Damage detection in structures using changes in flexibility." *J.Sound Vibrat.*: 169(1): pp. 3-17.

[57] Farrar, C. R., Doebling, S. W. and Nix, D. A. (2001). "Vibration–based structural damage identification." *Philosophical Transactions of the Royal Society of London A: Mathematical, Physical and Engineering Sciences*: 359(1778): pp. 131-149.

[58] Ewins, D. (2000). [Modal Testing: Theory, Practice, and Application], *Research Studies Press*.

[59] Yuen, K. (2010). "Efficient model correction method with modal measurement." *J.Eng.Mech.*: 136(1): pp. 91-99.

[60] Yuen, K. (2012). "Updating large models for mechanical systems using incomplete modal measurement." *Mechanical Systems and Signal Processing*: 28: pp. 297-308.

[61] Wu, Y. and Loh, C. (2013). "Application of Efficient Model Correction for Damage Assessment Using Limited Measurements." *Topics in Dynamics of Civil Structures - Proceedings of the 31st IMAC*: pp. 231-241.

[62] Visser, W. J. (1992). "Updating structural dynamics models using frequency response data." *University of London.* Doctor of Philosophy.

[63] Friswell, M. I. (2007). "Damage identification using inverse methods." *Philos.Trans.A.Math.Phys.Eng.Sci.*: 365(1851): pp. 393-410.

[64] Friswell, M. and Mottershead, J. E. (1995). [Finite Element Model Updating in Structural Dynamics], *Springer Science & Business Media*.

[65] Wang, Z., Lin, R. and Lim, M. (1997). "Structural damage detection using measured FRF data." *Comput.Methods Appl.Mech.Eng.*: 147(1): pp. 187-197.

[66] Begambre, O. and Laier, J. E. (2006). "Structural Damage Identification Using Particle Swarm Optimization." *Proceedings of the Fifth International Conference on Engineering Computational Technology*: pp. Paper 41.

[67] Jaishi, B. and Ren, W. (2007). "Finite element model updating based on eigenvalue and strain energy residuals using multiobjective optimisation technique." *Mechanical Systems and Signal Processing*: 21(5): pp. 2295-2317.

[68] Hao, H. and Xia, Y. (2002). "Vibration-based damage detection of structures by genetic algorithm." *J.Comput.Civ.Eng.*: 16(3): pp. 222-229.

[69] Friswell, M. I., Mottershead, J. E. and Ahmadian, H. (2001). "Finite–element model updating using experimental test data: parametrization and regularization." *Philosophical Transactions of the Royal Society of London A: Mathematical, Physical and Engineering Sciences*: 359(1778): pp. 169-186.

[70] Friswell, M., Penny, J. and Garvey, S. (1997). "Parameter subset selection in damage location." *Inverse Problems in Engineering*: 5(3): pp. 189-215.

[71] Song, W., Dyke, S., Yun, G. and Harmon, T. (2009). "Improved damage localization and quantification using subset selection." *J.Eng.Mech.*: 135(6): pp. 548-560.

[72] Yun, G. J., Ogorzalek, K. A., Dyke, S. J. and Song, W. (2010). "A parameter subset selection method using residual force vector for detecting multiple damage locations." *Structural Control and Health Monitoring*: 17(1): pp. 48-67.

[73] Yun, G. J., Ogorzalek, K. A., Dyke, S. J. and Song, W. (2009). "A two-stage damage detection approach based on subset selection and genetic algorithms." *Smart Structures and Systems*: 5(1): pp. 1-21.

[74] Shadan, F., Khoshnoudian, F. and Esfandiari, A. (2016). "A frequency response-based structural damage identification using model updating method." *Structural Control and Health Monitoring*: 23(2): pp. 286-302.

[75] Limongelli, M. (2003). "Optimal location of sensors for reconstruction of seismic responses through spline function interpolation." *Earthquake Eng.Struct.Dyn.*: 32(7): pp. 1055-1074.

[76] Shrikhande, M. (2011). "Reconstruction of missing response data for identification of higher modes." *Earthquakes and Structures*: 2(4): pp. 323-336.

[77] Chang, M. and Pakzad, S. N. (2014). "Optimal sensor placement for modal identification of bridge systems considering number of sensing nodes." *J.Bridge Eng.*: 19(6): pp. 04014019.

[78] Levine-West, M., Milman, M. and Kissil, A. (1996). "Mode shape expansion techniques for prediction-Experimental evaluation." *AIAA J.*: 34(4): pp. 821-829.

[79] O'Callahan, J. and Li, P. (1996). "SEREP expansion." *Proceedings of SPIE - The International Society for Optical Engineering*: pp. 1258-1264.

[80] Zhao, J. and Zhang, L. (2011). "A method for structural damage identification using residual force vector and mode shape expansion." *Multimedia Technology (ICMT), 2011 International Conference on Multimedia Technology*: pp. 945-949.

[81] Shi, Z., Law, S. and Zhang, L. (2000). "Damage localization by directly using incomplete mode shapes." *J.Eng.Mech.*: 126(6): pp. 656-660.

[82] Link, R. J. and Zimmerman, D. C. (2015). "Structural damage diagnosis using frequency response functions and orthogonal matching pursuit: theoretical development." *Structural Control and Health Monitoring*: 22(6): pp. 889-902.

[83] Lin, C., Lin, G. and Hsieh, K. (2014). "Damage Assessment of Seismically Excited Buildings Through Incomplete Measurements." *Journal of Pressure Vessel Technology*: 136(6): pp. 061801.

[84] Kammer, D. C. (1991). "Sensor placement for on-orbit modal identification and correlation of large space structures." *Journal of Guidance, Control, and Dynamics*: 14(2): pp. 251-259.

[85] Meo, M. and Zumpano, G. (2004). "Optimal sensor placement on a large-scale civil structure." *NDE for Health Monitoring and Diagnostics*: pp. 108-117.

[86] Li, D. and Li, H. (2006). "The state of the art of sensor placement methods in structural health monitoring." *Smart structures and materials*: pp. 61743T-61743T-11.

[87] Chow, H. M., Lam, H. F., Yin, T. and Au, S. K. (2011). "Optimal sensor configuration of a typical transmission tower for the purpose of structural model updating." *Structural Control and Health Monitoring*: 18(3): pp. 305-320.

[88] He, L., Lian, J., Ma, B. and Wang, H. (2014). "Optimal multiaxial sensor placement for modal identification of large structures." *Structural Control and Health Monitoring*: 21(1): pp. 61-79.

[89] Jalsan, K., Soman, R. N., Flouri, K., Kyriakides, M. A., Feltrin, G. and Onoufriou, T. (2014). "Layout optimization of wireless sensor networks for structural health monitoring." *Smart Structures and Systems*: 14(1): pp. 39-54.

[90] Papadopoulos, M. and Garcia, E. (1998). "Sensor placement methodologies for dynamic testing." *AIAA J.*: 36(2): pp. 256-263.

[91] Li, D., Li, H. and Fritzen, C. (2007). "The connection between effective independence and modal kinetic energy methods for sensor placement." *J.Sound Vibrat.*: 305(4): pp. 945-955.

[92] Meo, M. and Zumpano, G. (2005). "On the optimal sensor placement techniques for a bridge structure." *Eng.Struct.*: 27(10): pp. 1488-1497.

[93] Shi, Z., Law, S. and Zhang, L. (2000). "Optimum sensor placement for structural damage detection." *J.Eng.Mech.*: 126(11): pp. 1173-1179.

[94] Guo, Y., Ni, Y. and Chen, S. (2016). "Optimal sensor placement for damage detection of bridges subject to ship collision." *Structural Control and Health Monitoring*.

[95] Azarbayejani, M., El-Osery, A., Choi, K. and Taha, M. R. (2008). "A probabilistic approach for optimal sensor allocation in structural health monitoring." *Smart Mater.Struct.*: 17(5): pp. 055019.

[96] Cheng, L., Xie, H., Spencer Jr, B. and Giles, R. (2009). "Optimized finite element model updating method for damage detection using limited sensor information." *Smart Structures and Systems*: 5(6): pp. 681-697.

[97] Riveros, C. A., García, E. F. and Rivero, J. E. (2014). "Structural Damage Detection Using Sensors Optimally Located." *World Academy of Science, Engineering and Technology, International Journal of Civil, Environmental, Structural, Construction and Architectural Engineering*: 8(10): pp. 1071-1074.

[98] Tedesco, J. W., McDougal, W. G. and Ross, C. A. (1999). [Structural Dynamics: Theory and Applications], *Addison Wesley Longman*.

[99] Balageas, D., Fritzen, C. and Güemes, A. (2010). [Structural Health Monitoring], *John Wiley & Sons*.

[100] Van Overschee, P. and De Moor, B. (1994). "N4SID: Subspace algorithms for the identification of combined deterministic-stochastic systems." *Automatica*: 30(1): pp. 75-93.

[101] Skolnik, D., Lei, Y., Yu, E. and Wallace, J. W. (2006). "Identification, model updating, and response prediction of an instrumented 15-story steel-frame building." *Earthquake Spectra*: 22(3): pp. 781-802.

[102] He, C., Xing, J., Li, J., Yang, Q., Wang, R. and Zhang, X. (2013). "A combined optimal sensor placement strategy for the structural health monitoring of bridge structures." *International Journal of Distributed Sensor Networks*: 2013.

[103] Johnson, E. A., Lam, H. F., Katafygiotis, L. S. and Beck, J. L. (2004). "Phase I IASC-ASCE structural health monitoring benchmark problem using simulated data." *J.Eng.Mech.*: 130(1): pp. 3-15.

[104] Eskew, E. and Jang, S. (2014). "Damage Assessment of a Building Subjected to a Terrorist Attack." *Adv.Struct.Eng.*: 17(11): pp. 1693-1704.

[105] Li, J., Huang, M. and Zhu, H. (2009). "Study on Different Residual and Weight Coefficient in Model Updating of Bridge Structure." *ICCTP 2009@ sCritical Issues In Transportation Systems Planning, Development, and Management*: pp. 1-8.

[106] Haupt, R. L. and Haupt, S. E. (2004). [Practical Genetic Algorithms], *John Wiley & Sons*.

[107] Van Overschee, P. and De Moor, B. (1994). "N4SID: Subspace algorithms for the identification of combined deterministic-stochastic systems." *Automatica*: 30(1): pp. 75-93.

[108] Krauthammer, T., Hall, R. L., Woodson, S. C., Baylot, J. T., Hayes, J. R. and Sohn, Y. (2002). *Development of Progressive Collapse Analysis Procedure and Condition Assessment for Structures.*, DTIC Document.

[109] American Society of Civil Engineers (2007). [Seismic Rehabilitation of Existing Buildings], *ASCE Publications*.

[110] Johnson, G. R. and Cook, W. H. (1985). "Fracture characteristics of three metals subjected to various strains, strain rates, temperatures and pressures." *Eng.Fract.Mech.*: 21(1): pp. 31-48.

[111] Seidt, J., Gilat, A., Klein, J. and Leach, J. (2007). "High strain rate, high temperature constitutive and failure models for EOD impact scenarios." *Proceedings of the SEM Annual Conference & Exposition on Experimental and Applied Mechanics*: pp. 15.

[112] Hyde, D. W. (1988). [User's Guide for Microcomputer Programs ConWep and FunPro, Applications of TM 5-855-1," Fundamentals of Protective Design for Conventional Weapons"], *US Army Engineer Waterways Experiment Station*.

[113] Li, D., Li, H. and Fritzen, C. (2009). "A note on fast computation of effective independence through QR downdating for sensor placement." *Mechanical Systems and Signal Processing*: 23(4): pp. 1160-1168.

[114] Ribeiro, J., Santiago, A. and Rigueiro, C. (2016). "Material modelling of tensile steel component under impulsive loading." *International Journal of Structural Integrity*: 7(2): pp. 323-342.

[115] Xue, L. (2007). "Damage accumulation and fracture initiation in uncracked ductile solids subject to triaxial loading." *Int.J.Solids Structures*: 44(16): pp. 5163-5181.

[116] Shen, Z. and Dong, B. (1997). "An experiment-based cumulative damage mechanics model of steel under cyclic loading." *Adv.Struct.Eng.*: 1(1): pp. 39-46.

[117] Worden, K. and Burrows, A. (2001). "Optimal sensor placement for fault detection." *Eng.Struct.*: 23(8): pp. 885-901.

[118] Penny, J., Friswell, M. and Garvey, S. (1994). "Automatic choice of measurement locations for dynamic testing." *AIAA J.*: 32(2): pp. 407-414.

[119] Kammer, D. C. and Tinker, M. L. (2004). "Optimal placement of triaxial accelerometers for modal vibration tests." *Mechanical systems and signal processing*: 18(1): pp. 29-41.

[120] Lian, J., He, L. and Wang, H. (2012). "Optimal sensor placement in hydropower house based on improved triaxial effective independence method." *Water Science and Engineering*: 5(3): pp. 329-339.

9. APPENDIX A – OPTIMAL SENSOR PLACEMENT FOR FINITE ELEMENT MODELS USER MANUAL

An executable program titled the UConn Optimal Sensor Placement Tool Suite for Finite Element Models was created to locate sensors on numerical models of structures, using a variety of methods. The user manual for the program is presented in this appendix. The program can be downloaded at http://smart.engr.uconn.edu.

Program Overview

Monitoring of structures is important for many different structural engineering tasks. These include measuring modal parameters for model verification, construction monitoring, performance assessment, structural health monitoring (SHM), etc. The success of a monitoring application is directly dependent on the sensor placement. Well placed sensors can provide extensive information on the structure, whereas poorly placed sensors can lead to poor or wrong conclusions. Optimal sensor placement (OSP) is the study of how to place sensors, single or multi-axial, on a structure to optimize the output measurements. Many OSP methods utilize modal information from the structure to place the sensors at different degrees-of-freedom (DOF). Some different methods include the Effective Independence (EI) method, Effective Independence with Driving Point Residue (EI-DPR), Modal Kinetic Energy (MKE), and Genetic Algorithms (GA).

For practicing engineers, the SAP2000 finite element (FE) software from Computers and Structures inc (CSI), is a common design tool, especially for bridges. To facilitate the use of OSP for structures, this program was designed to provide access to multiple OSP methods, with the ability to draw models directly from SAP2000, as well as using user-generated numerical models. The following sections describe the operation of the program, as well as the analytical methods used within.

NOTE : The program is an executable program, built in MATLAB 2013a. Therefore, if the user doesn't own MATLAB 2013a, they may be required to load the MCR installer found in the installation package onto their computer before the program will run.

Exporting SAP2000 Models

One of the purposes of this program is to perform OSP using SAP2000 models. SAP2000 generates files to compile the stiffness (**K**) and mass (**M**) matrices of its models. These files can be exported out of SAP2000, for use in other programs. To export the model compilation files, in SAP2000 go to the Analyze tab and open Set Analysis Options. Clicking on the Solver Options button opens the Equation Solver Options box. Set the Solver Options option to Advanced Solver. This will enable the Select Analysis Case for Mass and Stiffness Text File Output. Select the appropriate case for model output, and select OK.

After running the analysis, a TXA, TXE, TXK, and TXM file will be generated in the solution folder. These files can be opened and saved in a text reader. The TXE file provides joint to DOF relationships. The TXK file provides the upper triangular global stiffness matrix value for each DOF. The TXM file provides the diagonal global mass matrix values. And the TXA file explains the outputs of the

previously mentioned files. In addition, a TXC file may be created for constraint equations, but it will not be used in this program.

The TXE, TXK, and TXM files can be used in the OSP program. However, the files need to be prepared for the simulation. Open each file individually, delete the header text, and save the file as a text file. This will prepare the TXK and TXM files. For the TXE files, if opened in Notepad, the last column will be shifted down a row. A fix for this is present in the program, and no modifications are required. If using a different text editor, please ensure that the TXE file columns are in order before loading. In addition, constrained joints may show up with text as the joint number. Please set any NULL joint terms to zero, and reassign any relevant constrained joint locations with a value. If plotting the geometry of the model, a file with the geometric locations of the additional joints will need to be created. The process is shown below, where Figure 9.1 is the original TXE file for a diaphragm constrain, Figure 9.2 is the modified TXE, and Figure 9.3 is the additional joint file.

	411					
171		-203	-204	138	137	136
	412					
172		-271	-272	10	11	12
	394					
NULL		0	0	0	0	0
	0					
CDIAPH1_		0	0	0	0	0
	0					
CDIAPH1_		391	392	0	0	0
	393					
CDIAPH1_		409	410	0	0	0
	411					
CDIAPH1_		414	413	0	0	0
	412					
CDIAPH1_		396	395	0	0	0
	394					

Figure 9.1 Original TXE with constraints and DOF shift

	411					
171		-203	-204	138	137	136
	412					
172		-271	-272	10	11	12
	394					
0		0	0	0	0	0
	0					
173		0	0	0	0	0
	0					
174		391	392	0	0	0
	393					
175		409	410	0	0	0
	411					
176		414	413	0	0	0
	412					
177		396	395	0	0	0
	394					

Figure 9.2 Modified TXE with constraints and DOF shift

173	0	0	0
174	0	0	14.6667
175	0	0	29.3333
176	0	0	44
177	0	0	58.6667

Figure 9.3 Constrained joint locations

If using a SAP2000 file, it is possible to generate the geometry of the model, and display the sensors. This requires the use of a geometry file, which can be generated from SAP2000. Once your model is complete, in SAP2000 go to the Display tab and click on the Show Tables button. Open the Connectivity Data tab, select Joint Coordinates, and then select Table: Joint Coordinates. Open the Object Connectivity tab under the Connectivity Data tab, and select Connectivity – Frame if your model contains frames, and/or Connectivity – Area if you model contains areas. The relevant tabs are shown in Figure 9.4. Once the tabs are selected, press OK. This will generate the appropriate tables. Export those tables to excel by opening the File tab, and selecting Export All Tables, and then To Excel. This generate an excel file, which is the geometry file for the program. Currently, the program is only capable of generating frames and areas with up to four corners.

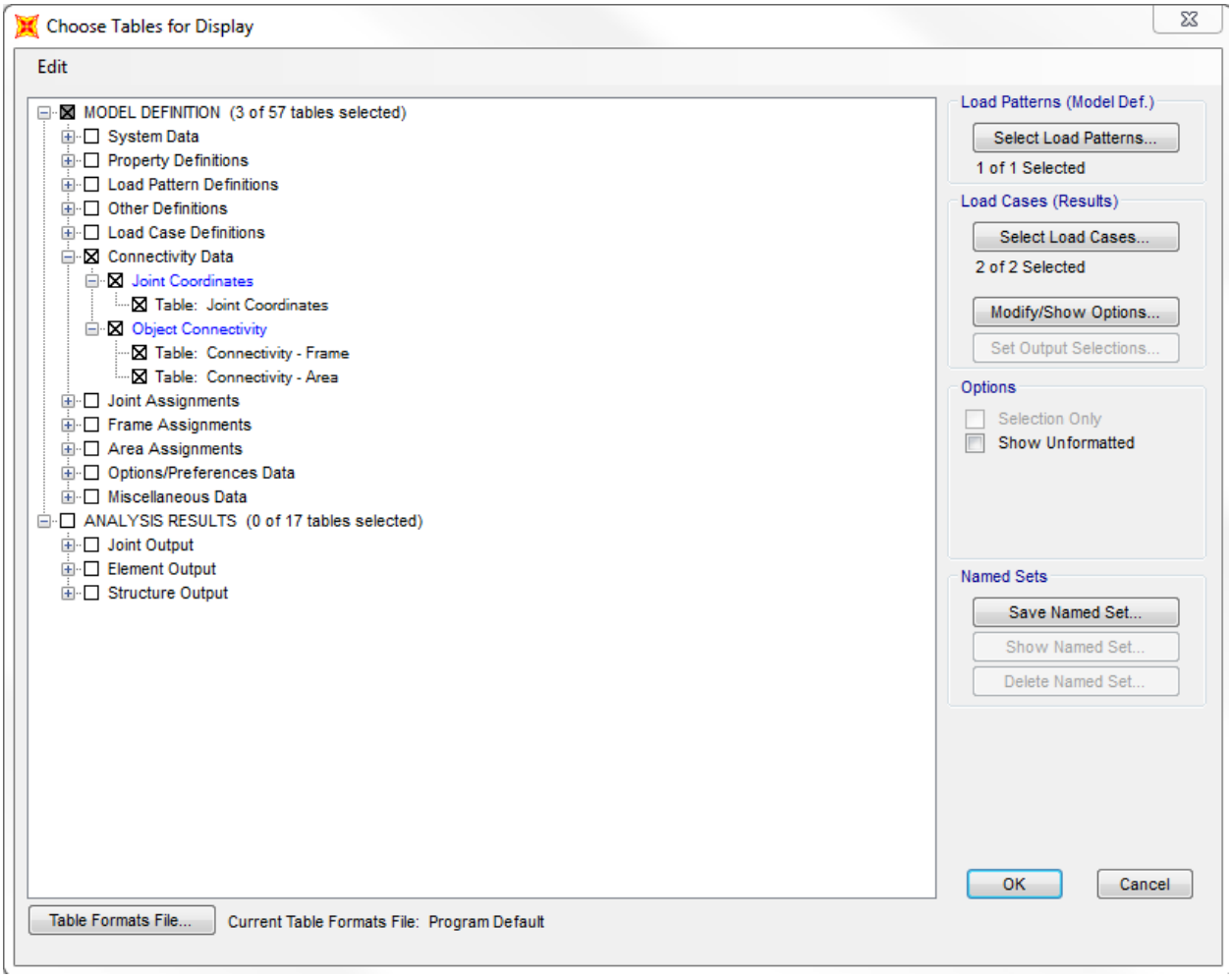

Figure 9.4 Generating the geometry file

Opening Pop-Up Menu

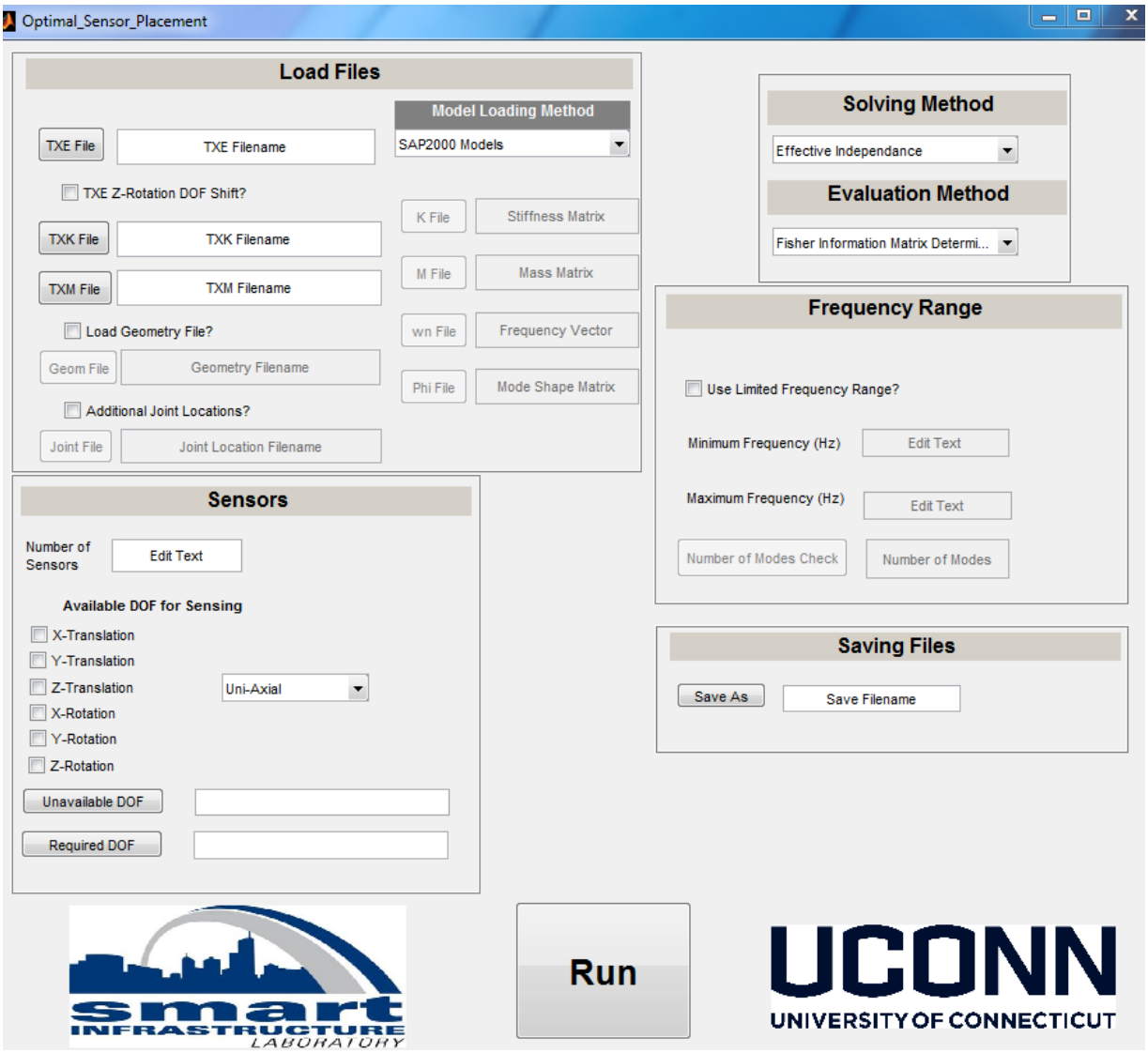

Figure 9.5 Opening pop-up menu

Load Files

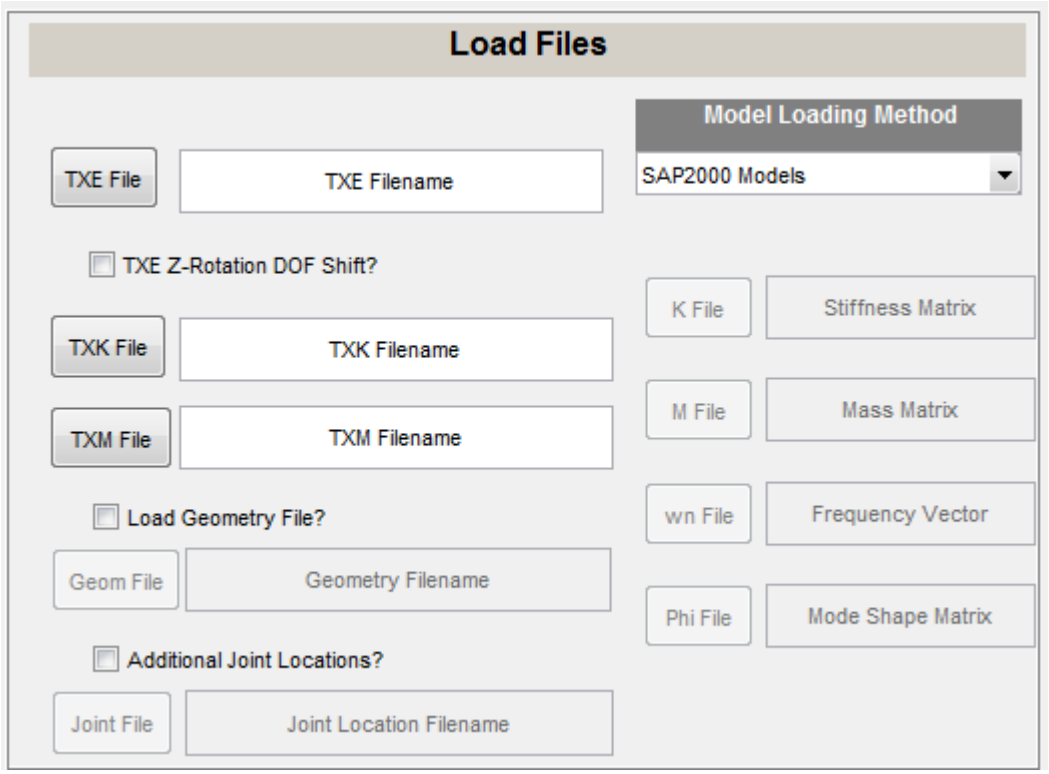

Figure 9.6 Load files box

The *Load Files* box, shown in Figure 9.6, is where the numerical model files are loaded into the program. First select the *Model Loading Method*. The types of models which can be loaded are SAP2000 model files, stiffness (**K**) and mass (**M**) matrices, or the natural frequency vector (**ω**) and mass-normalized mode shapes (**Φ**). Selecting the *SAP2000 Models* allows the user to load the *TXE File*, *TXK File*, and *TXM File*. If the TXE file has the column shift described previously, the user can select the *TXE Z-Rotation DOF Shift?* checkbox which will modify the file in the program. If the user wants to utilize a geometry file, they can select the *Load Geometry File?* checkbox and then load the file using the *Geom File* button. If the geometry file requires additional joint locations to compensate for constraints, the user can select the *Additional Joint Locations?* checkbox and load the file using the *Joint File* button.

If using **K** and **M** matrices for the model, change the *Model Loading Method* to *K and M Matrices*. This will activate the *K File* and *M File* buttons. These buttons will allow the user to load the appropriate .mat files.

If using **ω** and **Φ** for the model, change the *Model Loading Method* to *wn and Mass Normalized Phi*. This will activate the *wn File* and *Phi File* buttons. These buttons will allow the user to load the appropriate .mat files. The natural frequencies need to be in hertz.

Sensors

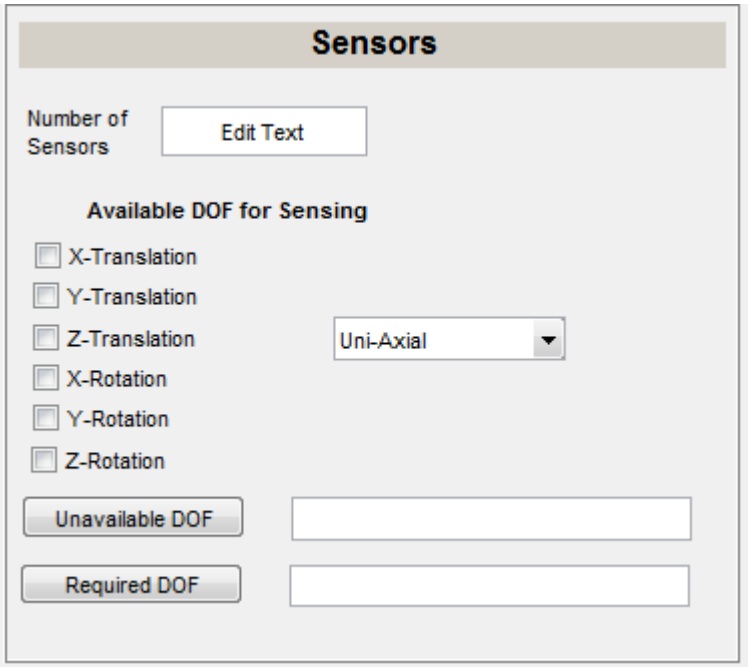

Figure 9.7 Sensors box

The *Sensors* box, shown in Figure 9.7, is used to identify the number of sensors to be used for monitoring, and the DOF available for measurement if using a SAP2000 model. In the *Number of Sensors* box, the user will input the number of sensors available for monitoring. It is important to note that, a principle of modal monitoring is that one cannot monitor more modes then sensors being used. Therefore, for accurate monitoring, it is important to ensure that the number of sensors is greater than the number of modes in the frequency range.

If the user is using a SAP2000 model as the *Model Loading Method*, then the user has to identify the type of sensors in use and select potential DOF for monitoring. The type of sensor is identified as *Uni-Axial*, where each sensor only monitors a single DOF, or *Multi-Axial*, where each sensor monitors all available DOF at the sensor location. The available DOF for monitoring are identified by selecting the checkboxes of the DOF that the user would like to be available for sensing. The DOF of the unchecked boxes will be treated as unavailable by the program.

The user can also select DOF to be unavailable or required for monitoring. This is done by creating a text file(s) with unavailable or required DOF in a vector. The file(s) are then loaded by clicking on the *Unavailable DOF* button, or the *Required DOF* button respectively.

Solution and Evaluation Methods

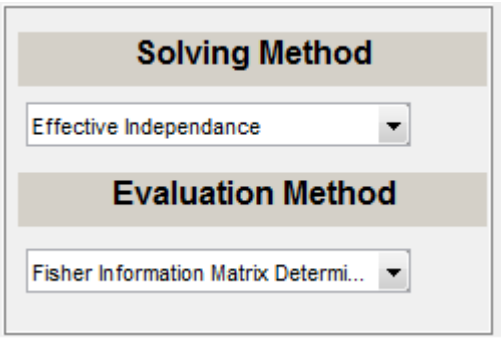

Figure 9.8 Solving method box

The *Solving Method* box, shown in Figure 9.8, is used to determine the analytical method for OSP. This is done by clicking on the pull-down menu, and selecting the desired method. The analysis methods include *Effective Independence*, *Effective Independence Driving Point Residue*, *Modal Kinetic Energy*, and *Genetic Algorithm* for *Uni-Axial* sensors, and *Multi-Axial Effective Independence*, *Multi-Axial Effective Independence Driving Point Residue*, *Multi-Axial Modal Kinetic Energy*, and *Genetic Algorithm* for *Multi-Axial* sensors. Each method is described in detail in subsequent sections. In addition, selection of the *Genetic Algorithm* method will result in a different pop-up menu, which will be described later, upon clicking on the Run button.

The *Evaluation Method* box, also shown in Figure 9.8, is used to select the method of evaluation of the determined sensor network. Selection is performed by clicking on the pull-down menu, and selecting the desired method. The analysis methods include *Fisher Information Determinant*, *Trace of Fisher Information Matrix*, *Condition Number of Fisher Information Matrix*, *Maximum Off-Diagonal MAC Term*, and *Singular Value Decomposition Ratio*. Each evaluation method is described in the Evaluation Methods section.

Frequency Range

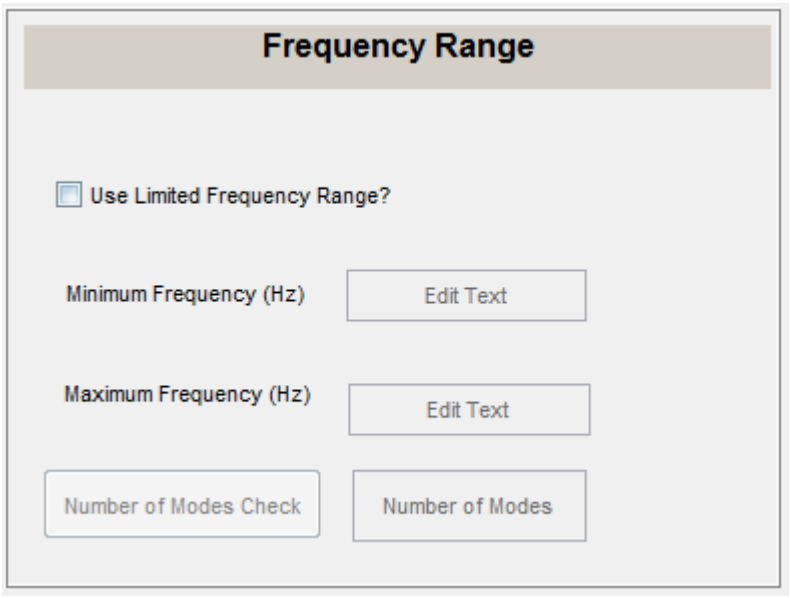

Figure 9.9 Frequency range box

The *Frequency Range* box, shown in Figure 9.9, allows the user to select the range of frequencies for monitoring. To select a limited frequency range, the user can activate the selection process by clicking on the *Use Limited Frequency Range?* checkbox. The user can then input the *Minimum Frequency* and *Maximum Frequency*, in hertz, into the applicable boxes. To see the number of modes within the range of frequencies selected, the user can click on the *Number of Modes Check* button. After loading, the number of modes in the frequency range will be displayed in the box adjacent to the button. It is important to note that accurate OSP requires more sensors than modes in the monitoring range.

Note: If using the full frequency range, the number of modes will equal the number of potential sensor DOF. This will likely cause inaccurate OSP results. It is highly encouraged to use a limited frequency range.

Saving Files

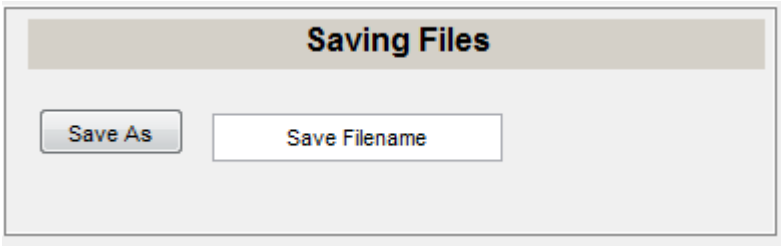

Figure 9.10 Saving files box

The *Saving Files* box, shown in Figure 9.10, is used to designate the location of the output files. This can be done by clicking on the *Save As* button, and inputting a save name and location. After the analysis is completed, the results will be exported to an excel file with that name.

Initializing the OSP

Figure 9.11 Run button

Once all of the above selections have been made, the user can initialize the OSP program by clicking on the *Run* button, shown in Figure 9.11.

Genetic Algorithm Pop-Up Menu

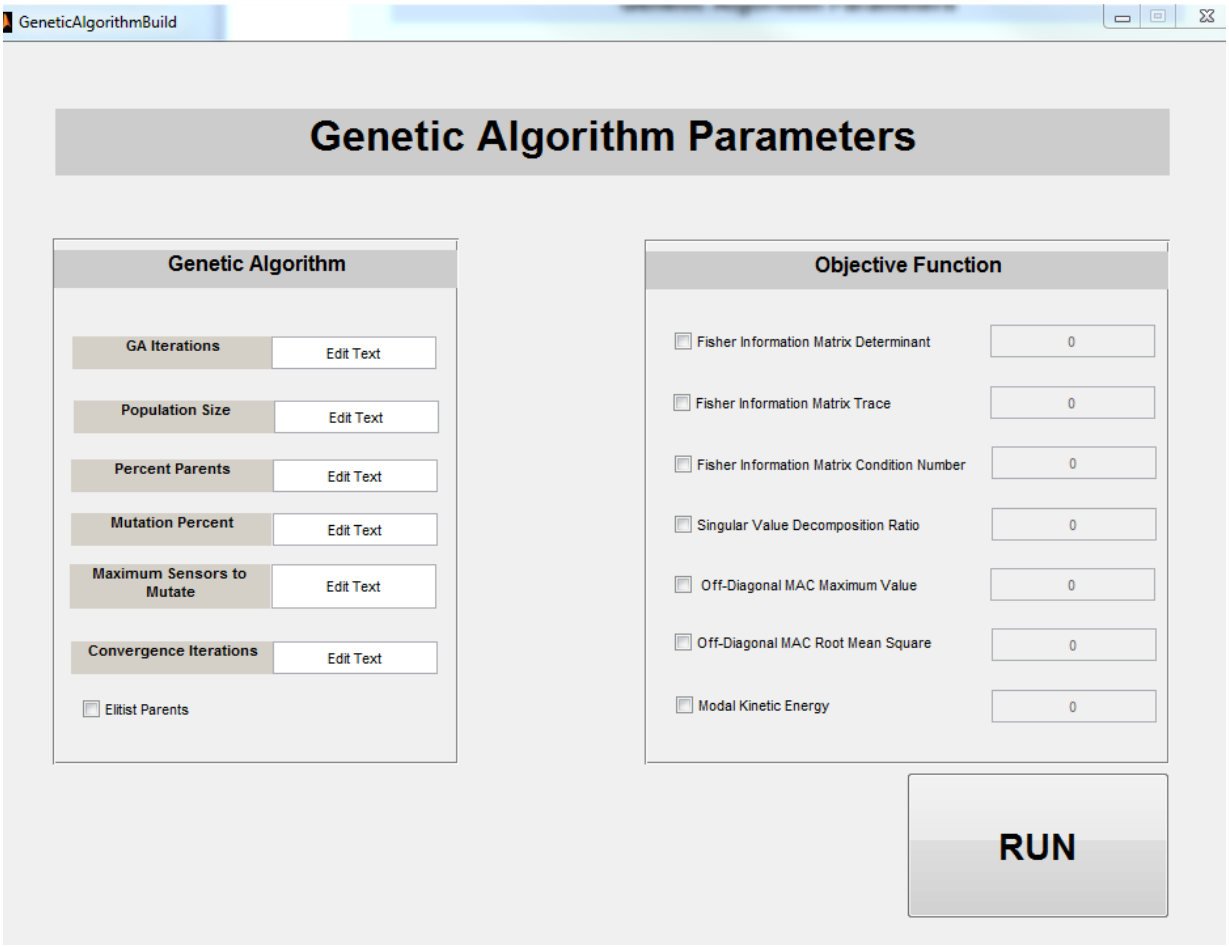

Figure 9.12 Genetic algorithm pop-up menu

If the *Genetic Algorithm* option is selected for the *Solving Method* in the *Opening Pop-Up Menu*, then the *Genetic Algorithm Pop-Up Menu*, shown in Figure 9.12, will open. In this pop-up menu, the parameters for the GA and its objective function are input. In the *Genetic Algorithm* box, the values for *GA Iterations*, *Population Size*, *Percent Parents*, *Mutation Percent*, *Maximum Sensors to Mutate*, and *Convergence Iterations* are input. If the user wants to include elitist parents in the GA, they can click on the *Elitist Parents* checkbox. In the *Objective Function* box, the values for *Fisher Determinant Weight*, *Fisher Norm Weight*, *Modal Kinetic Energy Weight*, and *Modal Assurance Criterion Weight* are input. The purpose of these parameters is described later in the Genetic Algorithm section. To initialize the program with the genetic algorithm solving methodology, the user can clicks the *RUN* button after the parameters are input.

Geometry Output

Geometrically displaying the results of an OSP analysis is a useful way of presenting the sensors locations. If using a SAP2000 model for the OSP, this program provides the capability to assemble a geometric model of the structure under analysis, and show the selected sensor DOF. In this program, the user can utilize frame elements, and area elements with up to four joints. Assembling the structural model requires the joint coordinates and connectivity information. The global joint coordinates, frame connectivity, and area connectivity can be exported as a single excel file from SAP2000 by selecting the appropriate tables in the Table tab of SAP2000, as described in the Exporting SAP2000 Models section. The program then assembles the structural model by coordinating the joints for the frames and areas from there connectivity tables, to the joints global coordinates.

Once the global structural model has been generated, the sensor locations and local DOF can be shown. If using *Uni-Axial* sensors, the joint coordinate table from SAP2000 is used to turn the selected sensor joint number(s) into global coordinates. The local DOF of the sensor is then represented by using different markers. X-Translation monitoring is represented by a red square, Y-Translation monitoring is represented by a green star, Z-Translation monitoring is represented by a black diamond, X-Rotation monitoring is represented by a magenta asterisk, Y-Rotation monitoring is represented by a yellow *X*, and Z-Rotation monitoring is represented by a cyan inverse triangle. A legend of the local DOF markers is shown in Figure 9.13. It is important to note that due to the limitations of the graphical imaging, some symbols may overlap others, making a final evaluation from the graphical interface can be difficult. The program table outputs should be consulted in regards the final sensor placement.

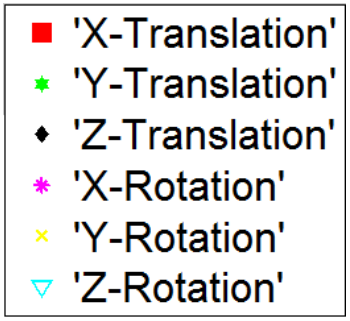

Figure 9.13 Local DOF marker legend

If using *Multi-Axial* sensors, the selected nodes for monitoring will be identified using red circles over the relevant locations.

Effective Independence Method

Methodology

The EI method, initially proposed by Kammer [84], locates the sensors to maximize the linear independence of the modal information [84, 90, 91]. The EI method begins by calculating the Fisher information matrix (***A***), which is the inverse of the covariance of the measurements [91, 117], for the potential sensor DOF. The Fisher information matrix is calculated using equation 9.1,

$$A = \frac{1}{{\sigma_s}^2} {\Phi_s}^{\boldsymbol{T}} \Phi_s \tag{9.1}$$

where $\boldsymbol{\sigma}$ is the measurement noise variance, and $_s$ are the monitored DOF. If the measurement noise is assumed to be uncorrelated [84], then the Fisher information matrix can be simplified to equation 9.2,

$$A = {\Phi_{sM}}^{\boldsymbol{T}} \Phi_{sM} \tag{9.2}$$

where $_M$ are the modes in the range of interest. The EI can then be calculated by equation 9.3,

$$EI = \boldsymbol{diag}[\Phi_{sM}\left(A^{\boldsymbol{-1}}\right){\Phi_{sM}}^{\boldsymbol{T}}] \tag{9.3}$$

The values of the EI will vary from 0 to 1, with 0 meaning that the sensor provides no independent information, and 1 meaning that the information from the sensor is completely independent from any other sensor [84]. OSP occurs by removing the sensors which provide the least independent information. In this program, this occurs sequentially by selecting the DOF with the lowest EI. That DOF is removed from the mode shapes, and the EI is recomputed. The procedure is repeated until requested number of sensors is reached, or all of the EI values are 1 and are therefore linearly independent from each other.

Outputs

After the analysis is completed a results pop-up will appear. On this pop-up, four main pieces of information will be shown, the selected sensors locations table (1), the number of sensors and measured modes (2), the effective independence of the removed sensors (3), and the evaluation metric at each sensor removal iteration (4). An example of the results pop-up using a SAP2000 file is shown in Figure 9.14. If using a SAP2000 model, the selected measurement locations table will display the joint number and measurement direction of the selected sensors. If using stiffness and mass matrices, or natural frequencies and mass-normalized mode shapes, the table will display the selected DOF numbers. The number of sensors and modes measured will be displayed to the right of the selected measurement locations. The requested number of selected measurements should match the selected number of sensors, unless the EI reached 1[1] before the requested number of sensors were removed, or there are more mode shapes in the frequency range then number of sensors for monitoring. The effective independence of the removed sensors figure will show the lowest EI value at each iteration which was selected for removal. And the evaluation metric figure will show the selected metric before each sensor is removed.

[1] For EI analysis; 0.9999999 is used instead of 1

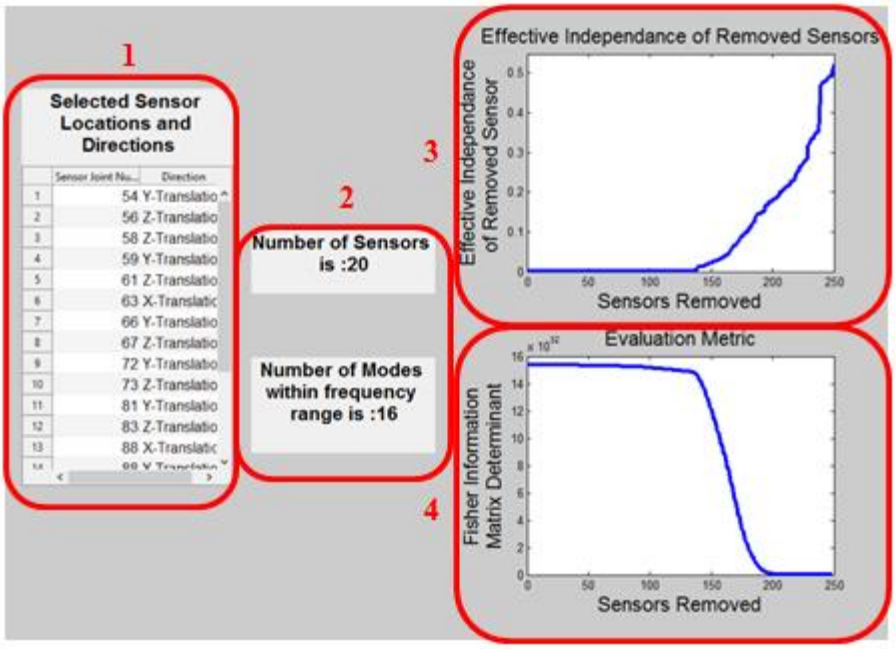

Figure 9.14 Sample effective independence results

After the EI analysis is completed, an excel file will be generated with the filename selected by the user in the *Saving Files* box. This excel file will have two spreadsheets. On sheet one, the selected sensor results are presented. If using a SAP2000 model, column 1 will present the joint number of the selected sensor(s), column 2 will present the selected sensor direction(s), column 3 will present the global DOF of the selected sensor(s), and column 4 will present the evaluation metric of the final sensor network. If using a stiffness and mass model or natural frequency and mass-normalized mode shapes, column 1 will present the global DOF of the selected sensor(s), and column 2 will present the evaluation metric of the final sensor network.

On the second sheet, the removed sensor information are presented. If using a SAP2000 model, column 1 will present the iteration(s) of the sensor removal, column 2 will present the effective independence of the removed sensor(s) which is also displayed in the results pop-up, column 3 will show the joint number of the removed sensor(s), column 4 will display the direction of the removed sensor(s), and column 5 will present the evaluation metric at each iteration of sensor removal. If using a stiffness and mass model or natural frequency and mass-normalized mode shapes, column 1 will present the iteration(s) of the sensor removal, column 2 will present the effective independence of the removed sensor(s) which is also displayed in the results pop-up, column 3 will present the global DOF of the removed sensor(s), and column 4 will present the evaluation metric at each iteration of sensor removal.

NOTE : The excel file updates upon saving. Saving to the same file name will only update the original excel output, and errors may results. It is recommended to either save to a new file name every time, or delete previous files with the same file name before running the OSP program.

Effective Independence with Driving Point Residue Method

Methodology

The driving point residue (DPR) is a measure of the DOF contribution in the modal range of interest [77, 90]. The DPR equation is presented in equation 9.4.

$$DPR_s = \sum_{j=1}^{U} \frac{\boldsymbol{\Phi}_{sj}^2}{\boldsymbol{\omega}_j} \tag{9.4}$$

where j is the jth mode number, and U are the number of modes in the range of interest. The EI method can present results which have low energy responses [12, 77, 92]. The DPR is utilized as a weighting function for the EI method to ensure that the sensor locations are linearly independent with high energy responses [12, 77, 92]. The combined method is called the EI-DPR method. The EI-DPR equation is presented in equation 9.5,

$$EI\_DPR = EI \otimes DPR \tag{9.5}$$

where $\otimes$ represents term-by-term multiplication. At each iteration of sensor selection, the smallest value of the EI-DPR is removed as the sensor presenting the least information. That DOF is removed from the mode shapes, and the EI-DPR is recomputed. The procedure is repeated until requested number of sensors is reached, or the EI-DPR of the sensor to be removed is less than the value of the previously removed sensor as that means that the number of sensors is at a critical level for providing information to the system, or the effective independence of the sensor network is equal to one[2].

Outputs

After the analysis is completed a results pop-up will appear. On this pop-up, four main pieces of information will be shown, the selected sensors locations table (1), the number of sensors and measured modes (2), the effective independence driving point residue of the removed sensors (3), and the evaluation metric at each sensor removal iteration (4). An example of the results pop-up using a SAP2000 file is shown in Figure 9.15. If using a SAP2000 model, the selected measurement locations table will display the joint number and measurement direction of the selected sensors. If using stiffness and mass matrices, or natural frequencies and mass-normalized mode shapes, the table will display the selected DOF numbers. The number of sensors and modes measured will be displayed to the right of the selected measurement locations. The requested number of selected measurements should match the selected number of sensors, unless there are more mode shapes in the frequency range then number of sensors for monitoring. The effective independence -DPR of the removed sensors figure will show the lowest EI-DPR value at each iteration which was selected for removal. And the evaluation metric figure will show the selected metric before each sensor is removed.

[2] For EI analysis; 0.9999999 is used instead of 1

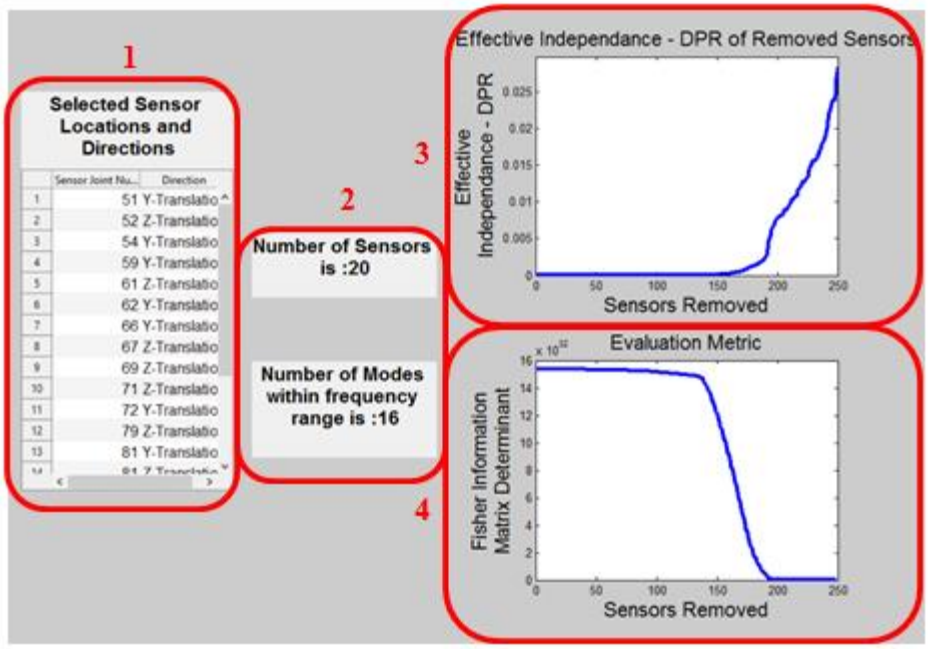

Figure 9.15 Sample effective independence – driving point residue results

An excel file will be generated with the filename selected by the user in the *Saving Files* box. This excel file will have two spreadsheets. On sheet one, the selected sensor results are presented. If using a SAP2000 model, column 1 will present the joint number of the selected sensor(s), column 2 will present the selected sensor direction(s), column 3 will present the global DOF of the selected sensor(s), and column 4 will present the evaluation metric of the final sensor network. If using a stiffness and mass model or natural frequency and mass-normalized mode shapes, column 1 will present the global DOF of the selected sensor(s), and column 2 will present the evaluation metric of the final sensor network.

On the second sheet, the removed sensor information are presented. If using a SAP2000 model, column 1 will present the iteration(s) of the sensor removal, column 2 will present the effective independence driving point residue of the removed sensor(s) which is also displayed in the results pop-up, column 3 will show the joint number of the removed sensor(s), column 4 will display the direction of the removed sensor(s), and column 5 will present the evaluation metric at each iteration of sensor removal. If using a stiffness and mass model or natural frequency and mass-normalized mode shapes, column 1 will present the iteration(s) of the sensor removal, column 2 will present the effective independence driving point residue of the removed sensor(s) which is also displayed in the results pop-up, column 3 will present the global DOF of the removed sensor(s), and column 4 will present the evaluation metric at each iteration of sensor removal.

NOTE : The excel file updates upon saving. Saving to the same file name will only update the original excel output, and errors may results. It is recommended to either save to a new file name every time, or delete previous files with the same file name before running the OSP program.

Modal Kinetic Energy Method

Methodology

The MKE is a measure of the kinetic energy from each mode at each DOF [90, 91]. The sensor locations with high MKE are likely to have the highest vibrational measurements when the modes are excited, and therefore be the best locations for system identification [90]. The MKE for the entire range of potential sensor locations is calculated using equation 9.6,

$$MKE = \Phi_{GM}{}^{T} M \Phi_{GM} \tag{9.6}$$

where $_G$ are all of the global DOF. To compare the MKE across the range of monitored modes, the modal kinetic energy can be averaged at each DOF across all of the modes of interest used[90]. The MKE at each DOF is calculated using equation 9.7.

$$\boldsymbol{MKE_s = \frac{1}{U}\sum_{j=1}^{U} MKE_{sj}} \tag{9.7}$$

For OSP, the sensors with the highest MKE are selected as monitoring DOF. This is done by initially calculating the MKE for the global system. The DOF which are not potential sensor locations are then removed from the analysis. The remaining DOF are ordered from the highest to lowest MKE values. The highest *N* MKE DOF are selected for monitoring, where *N* is the number of sensors selected by the user.

Outputs

After the analysis is completed a results pop-up will appear. On this pop-up, four main pieces of information will be shown, the selected sensors locations table (1), the number of sensors and measured modes (2), the modal kinetic energy of the sensors selected for monitoring (3), and the modal kinetic energy of the sensors removed from the monitoring system (4). An example of the results pop-up using a SAP2000 file is shown in Figure 9.16. If using a SAP2000 model, the selected measurement locations table will display the joint number and measurement direction of the selected sensors. If using stiffness and mass matrices, or natural frequencies and mass-normalized mode shapes, the table will display the selected DOF numbers. The number of sensors and modes measured will be displayed to the right of the selected measurement locations. The modal kinetic energy of the sensors selected for monitoring will display the MKE of the sensors determined to be monitoring DOF. And the MKE of the sensors removed from the monitoring system will display the MKE of the sensors which were determined not to be monitoring DOF.

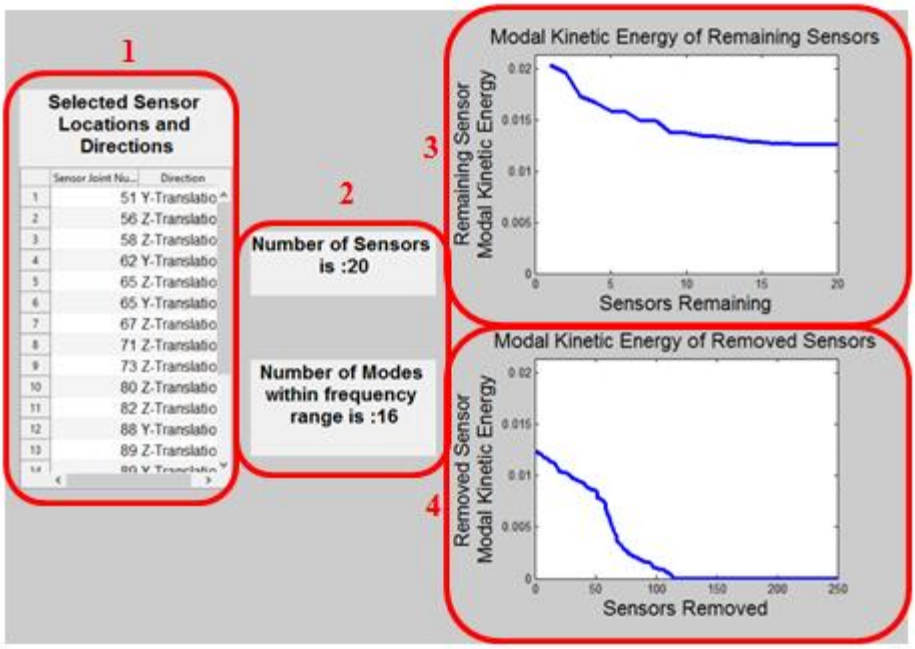

Figure 9.16 Sample modal kinetic energy results

An excel file will be generated with the filename selected by the user in the *Saving Files* box. This excel file will have two spreadsheets. On sheet one, the selected sensor results are presented. If using a SAP2000 model, column 1 will present the joint number of the selected sensor(s), column 2 will present the selected sensor direction(s), column 3 will present the global DOF of the selected sensor(s), and column 4 will present the evaluation metric of the final sensor network. If using a stiffness and mass model or natural frequency and mass-normalized mode shapes, column 1 will present the global DOF of the selected sensor(s), and column 2 will present the evaluation metric of the final sensor network.

On the second sheet, the removed sensor information are presented. If using a SAP2000 model, column 1 will present the iteration(s) of the sensor removal, column 2 will present the MKE of the removed sensor(s) which is also displayed in the results pop-up, column 3 will show the joint number of the removed sensor(s), and column 4 will display the direction of the removed sensor(s). If using a stiffness and mass model or natural frequency and mass-normalized mode shapes, column 1 will present the iteration(s) of the sensor removal, column 2 will present the MKE of the removed sensor(s) which is also displayed in the results pop-up, and column 3 will present the global DOF of the removed sensor(s).

NOTE : The excel file updates upon saving. Saving to the same file name will only update the original excel output, and errors may results. It is recommended to either save to a new file name every time, or delete previous files with the same file name before running the OSP program.

Genetic Algorithm

Methodology

Genetic algorithms are a type of evolutionary metaheuristic. They mimic the principles of natural selection to derive a solution to an optimization problem. A potential solution to the genetic algorithm is called a "chromosome," which is an array of variables which are the parameters being optimized. To begin the GA, a random initial population of chromosomes is generated. Each chromosome is evaluated using an objective function. The fittest solutions are then selected to "breed". In this program fitness relates to maximizing the objective function. "Breeding" is the process of generating the next population of solutions using the best solutions of the current population. In this program, breeding occurs using a crossover function, described later. The new generation is then subjected to mutations. Additionally, the parents can be elitist, which means the fittest solutions from the past generation are carried over into the new generation. The next population is then evaluated using the objective function. This process is repeated until the solutions meet a set convergence criteria. The process is described in Figure 9.17. Due to the random nature of the GA, repeating the analysis multiple times is recommended to insure a quality solution. The program offers the ability to repeat the GA using the input *GA Iterations*.

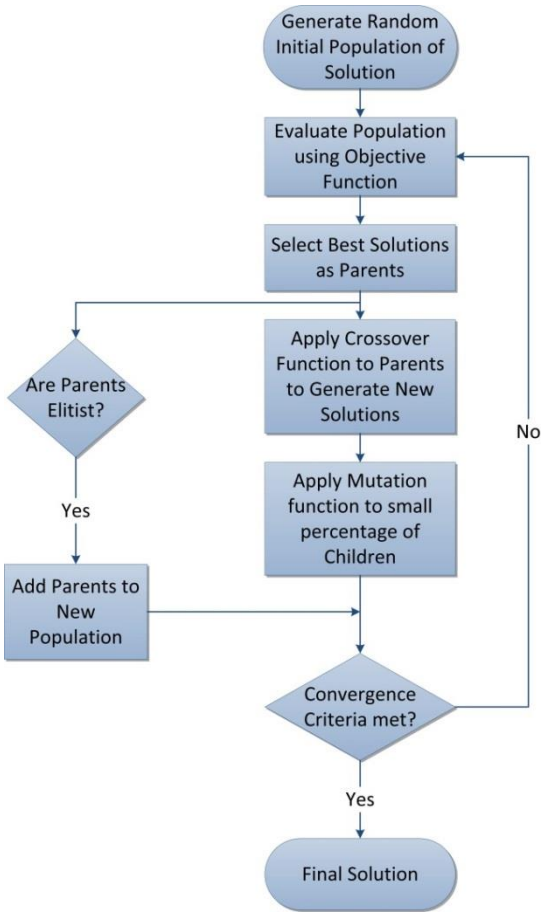

Figure 9.17 Genetic algorithm flowchart

For this program, if using *K and M Matrices, wn and Mass Normalized Phi*, or *SAP2000 Models* with *Uni-Axial* sensors, each chromosome is an array the size of the number of potential monitored DOF. If using, *SAP2000 Models* with *Multi-Axial* sensors, then the chromosome will be the size of potential monitoring nodes. The array is filled with zeros which represent non-active sensor locations, and *N* ones which represent active sensor locations. The number of chromosomes in a generation is dictated by the user input *Population Size*. Breeding for the integer chromosomes is performed by randomly selecting two different parents from the fittest solutions of the previous generation. The size of the parent pool is calculated as percent of the total population, using the input *Percent Parents*. A chromosome cut point is then randomly selected. Child A merges the array of parent A to the left of the cut and the array of parent B to the right of the cut. Child B merges the array of parent B to the left of the cut and the array of parent A to the right of the cut. This process is demonstrated in Figure 9.18. After each child is generated, it is randomly determined if it will undergo mutations. This is done by randomly generating a number between 0 and 1. If the number is below the *Mutation Percent*, input by the user, then mutations will occur for that child. The mutation process begins by randomly selecting the number of mutations to occur within the chromosome. This is done by generating a random integer between 1 and the *Maximum Sensors to Mutate*, as input by the user. Different locations within the child array totaling the number of mutations are then randomly selected. If the value of the mutated cell is 0 then it is changed to 1, and if it is 1 then it is changed to 0. After the mutation phase of the GA is finished, the program applies a constraint equation to ensure that the number of active sensors each chromosome is the same as requested by the user. If the number of active sensors in the child does not equal the number requested by the user, then the child is discarded. This process is repeated until the number of children required for the next population are generated. If the breeding process generates one more child then needed, Child B is discarded. If the parents are elitist, the breeding will generate the size of the next population minus the number of parents.

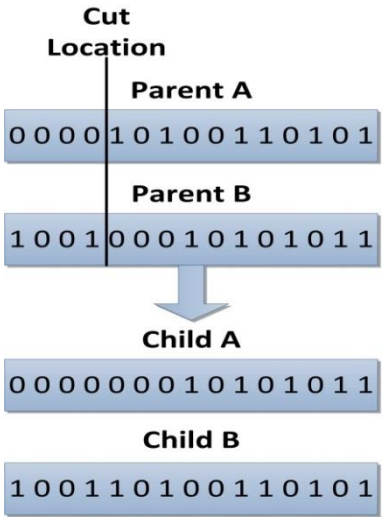

Figure 9.18 Genetic algorithm chromosome breeding

Objective Function

After a population is generated, each chromosome is evaluated using the objective function, which determines the fitness of the solution. Fitness is determined through maximization of the objective function. This program utilizes a multi-objective function with weights on each objective, as shown in equation 9.8,

$$\boldsymbol{J(\theta) = \sum W_q J_q(\theta)} \tag{9.8}$$

where J is the objective function, θ is the chromosome being evaluated, $_q$ is each individual objective function, and W are the individual objective function weights which are user inputs from the *Objective Function* box of the *Genetic Algorithm Pop-Up Menu*. There are 7 individual objective functions, the relative determinant (*det*) of the Fisher information matrix, the relative trace (*tr*) of the Fisher information matrix, the relative condition number (κ) of the Fisher information matrix, the singular value decomposition (SVD) ratio of the mode shapes, the maximum off-diagonal term of the Modal Assurance Criterion (MAC), the root mean square (RMS) of the MAC, and the averaged MKE. The relative determinant of the Fisher information matrix is a measure of the information within the sensor network [84, 118]. The objective function for the relative determinant of the Fisher Information matrix is shown in equation 9.9,

$$\boldsymbol{J_{\mathbf{det}(A)}(\theta) = \frac{\mathbf{det}(A_s)}{\mathbf{det}(A_S)}} \tag{9.9}$$

where $_S$ are all of the potential sensor locations. The values of the relative determinant will be less than one, with the GA maximizing the objective term. The relative trace of the Fisher Information matrix is a measure of the estimate error covariance matrix, and is a metric of the accuracy of the sensor information [12, 84]. The relative trace of the Fisher Information matrix is shown in equation 9.10.

$$\boldsymbol{J_{\mathbf{tr}(A)}(\theta) = \frac{\mathbf{tr}(A_s)}{\mathbf{tr}(A_S)}} \tag{9.10}$$

The values of the relative trace will be less than one, with the GA maximizing the objective term. The condition number of the Fisher Information matrix is a measure of the sensitivity of the estimates to analytical modeling error, with lower values being ideal [12, 84]. The relative condition number is shown in equation 9.11.

$$\boldsymbol{J_{\boldsymbol{\kappa}(A)}(\theta) = \frac{\boldsymbol{\kappa}(A_s)}{\boldsymbol{\kappa}(A_S)}} \tag{9.11}$$

The values of the relative condition number will be less than one, with the GA maximizing the objective term. The SVD ratio is the ratio of the largest and smallest singular values of the mode shape for the measured DOF and monitored modes, with values ranging from one to infinity [118]. The closer to one the SVD, the better the network is in terms of the mode orthogonality, capability for modal expansion, and observability of modes. The SVD ratio is inverted for the objective function, to set the maximum value as one. The SVD vector and SVD ratio objective function are shown in equations 9.12 and 9.13.

$$SVD = \boldsymbol{svd}(\Phi_{sM}) \tag{9.12}$$

$$\boldsymbol{J_{\mathbf{SVD}}(\theta) = \frac{\mathbf{min}(SVD)}{\mathbf{max}(SVD)}} \tag{9.13}$$

The MAC is a measure of two mode shape matrices correlation to each other. The MAC equation is shown in equation 9.14,

$$MAC_{xy} = \frac{(\phi_{a,x}{}^T \phi_{b,y})^2}{(\phi_{a,x}{}^T \Phi_{a,x})(\phi_{b,y}{}^T \phi_{b,y})} \tag{9.14}$$

where $_a$ is the first mode shape matrix, $_b$ is the second mode shape matrix, and $_x$ and $_y$ are index terms for the mode numbers. All terms in the MAC matrix range from 0 to 1. The off-diagonal terms in the MAC represent the correlation of different mode shapes in the matrix to each other. When both mode shapes in the MAC equation are from the same model with limited sensors, the off-diagonal terms show the linear dependence between the two mode shapes. To maximize the independence of the individual sensors measurements, the maximum off-diagonal MAC objective term minimizes the largest off-diagonal term of the MAC matrix of the active DOF across all modes of interest in comparison to itself. The maximum off-diagonal MAC objective function is shown in equation 9.15,

$$\boldsymbol{J(\theta)_{\max(MAC_{uy})} = \left(1 - \max(MAC(\theta)_{xy})\right) \ , \ x \neq y} \tag{9.15}$$

The RMS of the off-diagonal MAC terms is another method to measure the linear dependence of the sensors responses. The RMS of the off-diagonal MAC objective function is shown in equation 9.16.

$$\boldsymbol{J(\theta)_{\max(MAC_{uy})} = \left(1 - rms(MAC(\theta)_{xy})\right) \ , \ x \neq y} \tag{9.16}$$

The MKE objective function takes the global MKE, calculated using equation 9.7, and sums the values at each active DOF, divided by the number of measured modes. The MKE objective term has values ranging from 0 to 1, with larger values being sought by the GA. This MKE objective function is shown in equation 9.17.

$$\boldsymbol{J(\theta)_{MKE} = \sum MKE_{\theta}} \tag{9.17}$$

While the GA is in operation, progress will be shown through plotting of the fittest objective function values. The plot will be updated every *Convergence Iterations*, or after the current GA iteration is completed. The different GA iterations will be plotted using randomly generated colors. An example of the objective function plot is shown in Figure 9.19.

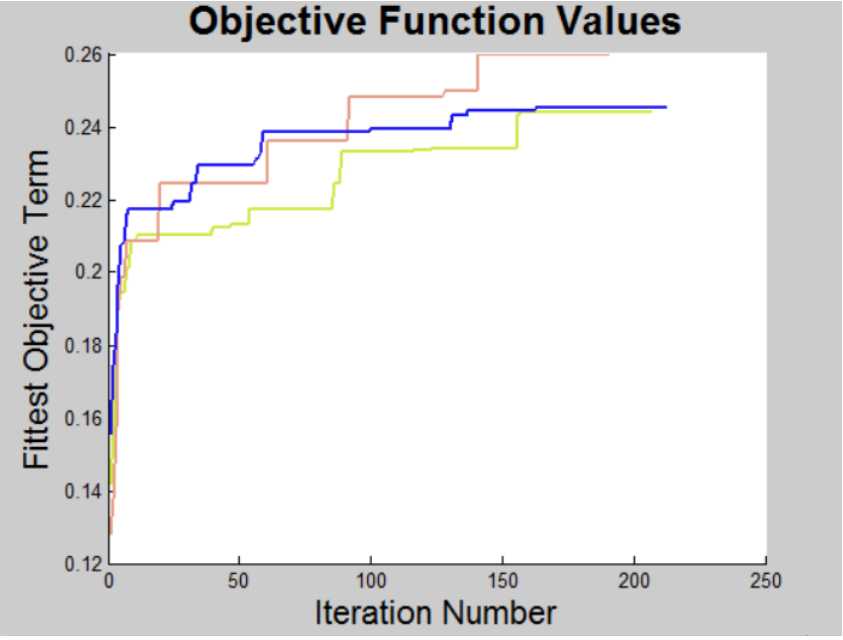

Figure 9.19 Objective term progress plot

Outputs

After the analysis is completed a results pop-up will appear. On this pop-up, four main pieces of information will be shown, the selected sensors locations table (1), the number of sensors and measured modes (2), the histogram of the final sensor locations from all of the iterations of the GA (3), and a histogram of the final objective function values from each iteration of the GA (4). An example of the results pop-up using a SAP2000 file is shown in Figure 9.20. If using a SAP2000 model with *Uni-Axial* sensors, the selected measurement locations table will display the joint number and measurement direction of the selected sensors. If a SAP2000 model with *Multi-Axial* sensors is used, the selected measurement locations table will display the node numbers of the selected sensors. And, if using stiffness and mass matrices or natural frequencies and mass-normalized mode shapes, the table will display the selected DOF numbers. The number of sensors and modes measured will be displayed to the right of the selected measurement locations. The sensor location histogram shows the frequency of a measurement DOF or node being selected as a sensor location over in the converged solutions from the GA iterations. And the histogram of the final objective values shows the winning values of each GA iteration. The user can use this to evaluate the results of the GA.

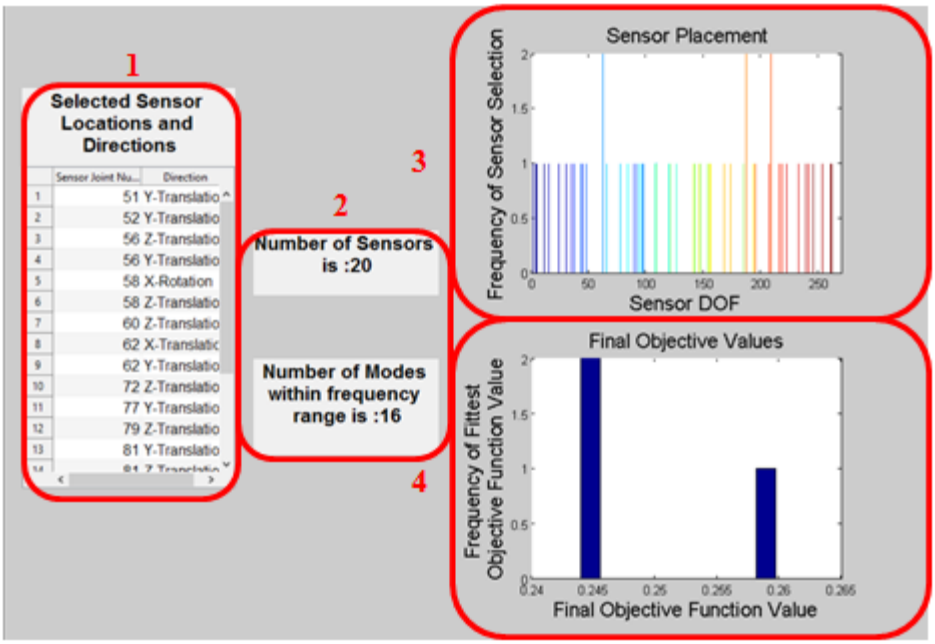

Figure 9.20 Sample genetic algorithm results

An excel file will be generated with the filename selected by the user in the *Saving Files* box. This excel file will have two spreadsheets. On sheet one, the active sensors results from the GA evaluation are presented. The final sensor selection is the GA solution with the highest objective function value. If using a SAP2000 model with *Uni-Axial* sensors, column 1 will present the joint number of the selected sensor(s), column 2 will present the selected sensor direction(s), column 3 will present the global DOF of the selected sensor(s), and column 4 will present the evaluation metric of the final sensor network. If using a SAP2000 model with *Multi-Axial* sensors, column 1 will present the node number of the selected sensor(s), and column 2 will present the evaluation metric of the final sensor network. And, if using a stiffness and mass model or natural frequency and mass-normalized mode shapes, column 1 will present the global DOF of the selected sensor(s), and column 2 will present the evaluation metric of the final sensor network.

On the second sheet, the fittest solution from each iteration of the GA is presented. In the first row, the GA iteration number is presented. In the second row, the evaluation metric for that sensor network is presented. In the third row, the objective function of the fittest solution from each iteration is presented. And in the subsequent rows, the final selected DOF or nodes for monitoring are shown.

NOTE : The excel file updates upon saving. Saving to the same file name will only update the original excel output, and errors may results. It is recommended to either save to a new file name every time, or delete previous files with the same file name before running the OSP program.

Multi-Axial Effective Independence Method

Methodology

The multi-axial effective independence method, proposed by Kammer [119], locates sensors which measure multiple DOF to maximize the linear independence of the modal information. The multi-axial EI calculates the effective independence at each node for the monitored DOF. The sensor EI is calculated using equation 9.18,

$$EI_{D,n} = \mathbf{1} - \mathbf{det}(I_D - \Phi_{D,n,M} A_{D,n,M}^{-\mathbf{1}} \Phi_{D,n,M}{}^{\boldsymbol{T}}) \tag{9.18}$$

where $\boldsymbol{I}$ is the identity matrix, $_D$ are the DOF monitored for each sensor, $_n$ is the sensor node, and $\boldsymbol{A}_{D,n,M}$ is the Fisher Information matrix for the sensor, calculated using equation 9.19.

$$A_{D,n,M} = \Phi_{D,n,M}{}^{\boldsymbol{T}} \Phi_{D,n,M} \tag{9.19}$$

The values of the multi-axial EI will vary from 0 to 1, with 0 meaning that the sensor provides no independent information, and 1 meaning that the information from the sensor is completely independent from any other sensor [84]. OSP occurs by removing the sensors which provide the least independent information. In this program, this occurs sequentially by selecting the nodes with the lowest EI. That sensor node is removed from the mode shapes, and the EI is recomputed. The procedure is repeated until requested number of sensors is reached, or all of the EI values are 1[3] and are therefore linearly independent from each other.

Outputs

After the analysis is completed a results pop-up will appear. On this pop-up, four main pieces of information will be shown, the selected sensors node numbers table (1), the number of sensors and measured modes (2), the effective independence of the removed sensors (3), and the evaluation metric at each sensor removal iteration (4). An example of the results pop-up is shown in Figure 9.21. The number of sensors and modes measured will be displayed to the right of the selected sensor node locations. The requested number of selected measurements should match the selected number of sensors, unless the EI reached 1 before the requested number of sensors were removed, or there are more mode shapes in the frequency range then number of sensors for monitoring. The effective independence of the removed sensors figure will show the lowest EI value at each iteration which was selected for removal. And the evaluation metric figure will show the selected metric before each sensor is removed.

[3] For EI analysis; 0.9999999 is used instead of 1

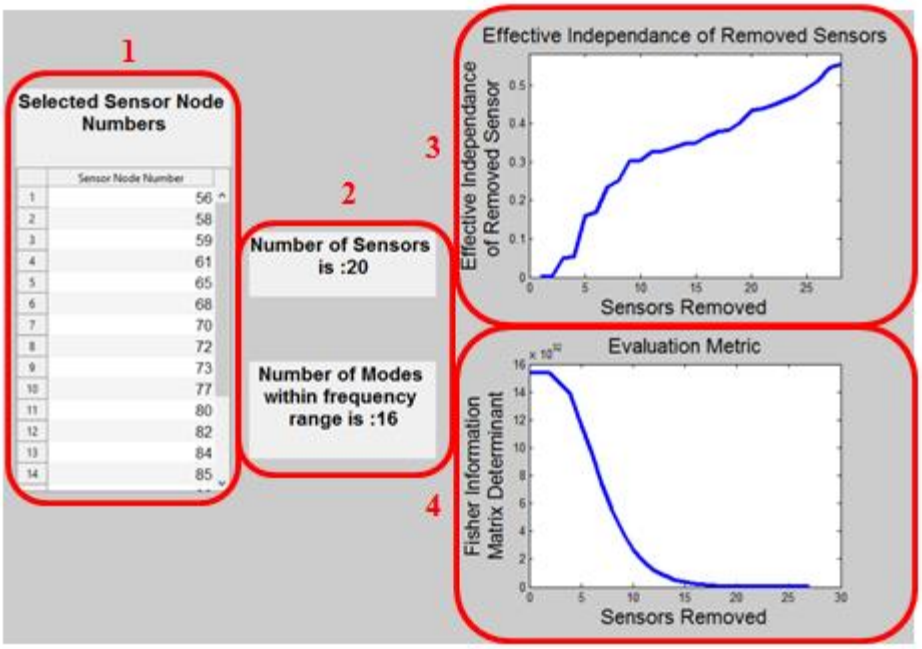

Figure 9.21 Sample multi-axial effective independence results

After the multi-axial EI analysis is completed, an excel file will be generated with the filename selected by the user in the *Saving Files* box. This excel file will have two spreadsheets. On sheet one, the selected sensor results are presented. Column 1 will present the node number of the selected sensor(s), and column 2 will present the evaluation metric of the final sensor network. On the second sheet, the removed sensor information are presented. Column 1 will present the iteration(s) of the sensor removal, column 2 will present the effective independence of the removed sensor(s) which is also displayed in the results pop-up, column 3 will show the node number of the removed sensor(s), and column 4 will present the evaluation metric at each iteration of sensor removal.

NOTE : The excel file updates upon saving. Saving to the same file name will only update the original excel output, and errors may results. It is recommended to either save to a new file name every time, or delete previous files with the same file name before running the OSP program.

Multi-Axial Effective Independence Driving Point Residue Method

Methodology

The multi-axial EI-DPR method weights the multi-axial EI with the DPR of the measured DOF of the sensor [120]. The sensor DPR is calculated using equation 9.20, with the multi-axial EI-DPR equation shown in equation 9.21.

$$DPR_{\boldsymbol{n}} = \sum_{\boldsymbol{j=1}}^{\boldsymbol{U}} \frac{\sum_{\boldsymbol{i=1}}^{\boldsymbol{D}} \boldsymbol{\Phi_{ij}^2}}{\boldsymbol{\omega_j}} \tag{9.20}$$

$$EI\_DPR_{D,n} = DPR_{D,n} EI_{D,n} \tag{9.21}$$

At each iteration of the sensor selection, the smallest value of the multi-axial EI-DPR is removed as the sensor presenting the least information. That nodes DOF are removed from the mode shapes, and the multi-axial EI-DPR is recomputed. The procedure is repeated until requested number of sensors is reached, the EI-DPR of the sensor to be removed is less than the value of the previously removed sensor as that means that the number of sensors is at a critical level for providing information to the system, or the effective independence of the sensor network is equal to one[4].

Outputs

After the analysis is completed a results pop-up will appear. On this pop-up, four main pieces of information will be shown, the selected sensors node numbers table (1), the number of sensors and measured modes (2), the effective independence driving point residue of the removed sensors (3), and the evaluation metric at each sensor removal iteration (4). An example of the results pop-up is shown in Figure 9.22. The number of sensors and modes measured will be displayed to the right of the selected sensor node locations. The requested number of selected measurements should match the selected number of sensors, unless there are more mode shapes in the frequency range then number of sensors for monitoring. The effective independence -DPR of the removed sensors figure will show the lowest EI-DPR value at each iteration which was selected for removal. And the evaluation metric figure will show the selected metric before each sensor is removed.

[4] For EI analysis; 0.9999999 is used instead of 1

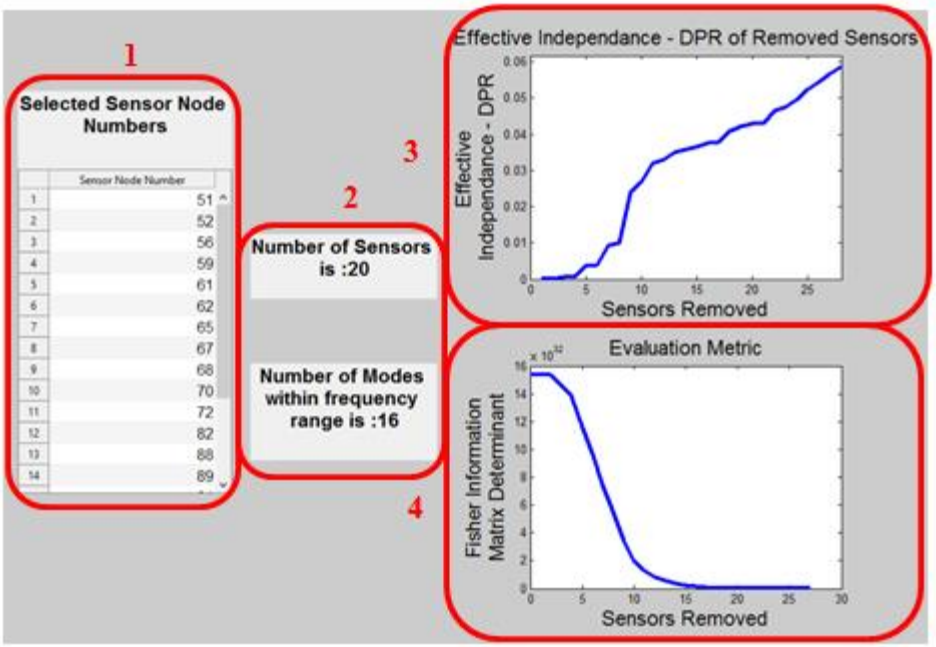

Figure 9.22 Sample multi-axial effective independence - driving point residue results

After the multi-axial EI-DPR analysis is completed, an excel file will be generated with the filename selected by the user in the *Saving Files* box. This excel file will have two spreadsheets. On sheet one, the selected sensor results are presented. Column 1 will present the node number of the selected sensor(s), and column 2 will present the evaluation metric of the final sensor network. On the second sheet, the removed sensor information are presented. Column 1 will present the iteration(s) of the sensor removal, column 2 will present effective independence driving point residue of the removed sensor(s) which is also displayed in the results pop-up, column 3 will show the node number of the removed sensor(s), and column 4 will present the evaluation metric at each iteration of sensor removal.

NOTE : The excel file updates upon saving. Saving to the same file name will only update the original excel output, and errors may results. It is recommended to either save to a new file name every time, or delete previous files with the same file name before running the OSP program.

Multi-Axial Modal Kinetic Energy Method

Methodology

The multi-axial MKE method combines the MKE of each monitored DOF at the sensor node. The sensor locations with high MKE are likely to have the highest vibrational measurements when the modes are excited, and therefore be the best locations for system identification [90]. The MKE for each node is calculated using equation 9.22.

$$MKE_n = \Phi_{\boldsymbol{DM}}{}^{\boldsymbol{T}} M \Phi_{\boldsymbol{DM}} \tag{9.22}$$

To compare the MKE across the range of monitored modes, the MKE is averaged at each node across all of the modes of interest. The averaged MKE at each node is calculated using equation 9.23.

$$\boldsymbol{MKE_n} = \frac{\boldsymbol{1}}{\boldsymbol{U}} \sum_{\boldsymbol{j=1}}^{\boldsymbol{U}} \boldsymbol{MKE_{Dj}} \tag{9.23}$$

For OSP, the *N* sensors locations with the highest average MKE are selected as the monitoring nodes, where *N* is the number of sensors selected by the user.

Outputs

After the analysis is completed a results pop-up will appear. On this pop-up, four main pieces of information will be shown, the selected sensors node numbers table (1), the number of sensors and measured modes (2), the modal kinetic energy of the sensors selected for monitoring (3), and the modal kinetic energy of the sensors removed from the monitoring system (4). An example of the results pop-up using a SAP2000 file is shown in Figure 9.23. The number of sensors and modes measured will be displayed to the right of the selected sensor node locations. The modal kinetic energy of the sensors selected for monitoring will display the MKE of the sensors determined to be monitoring nodes. And the MKE of the sensors removed from the monitoring system will display the MKE of the sensors which were determined not to be monitoring nodes.

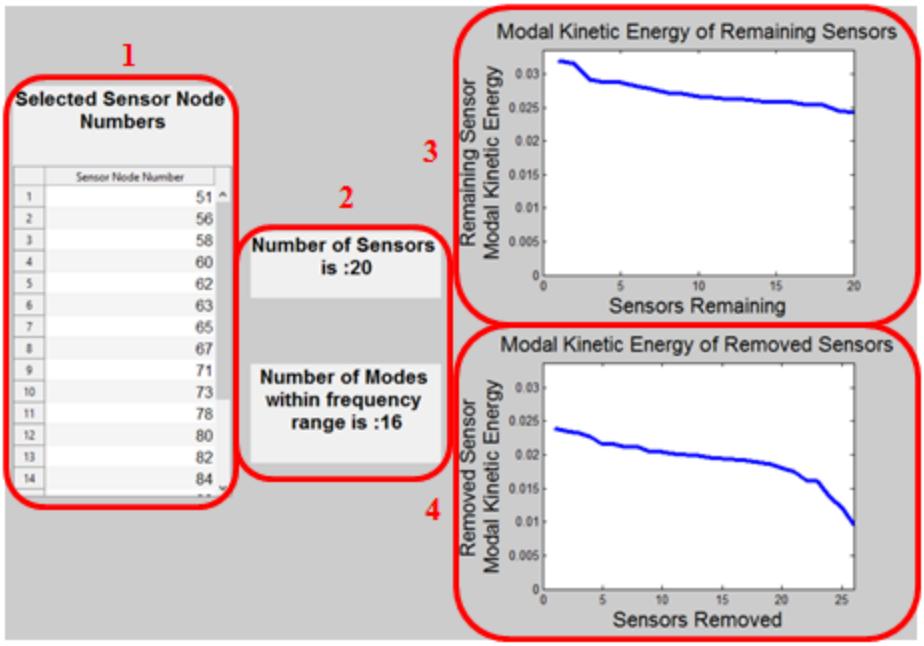

Figure 9.23 Multi-axial sample modal kinetic energy results

An excel file will be generated with the filename selected by the user in the *Saving Files* box. This excel file will have two spreadsheets. On sheet one, the selected sensor results are presented. Column 1 will present the node number of the selected sensor(s), and column 2 will present the evaluation metric of the final sensor network. On the second sheet, the removed sensor information are presented. Column 1 will present the order of the sensor removal, column 2 will present the MKE of the removed sensor(s) which is also displayed in the results pop-up, and column 3 will show the node number of the removed sensor(s).

NOTE : The excel file updates upon saving. Saving to the same file name will only update the original excel output, and errors may results. It is recommended to either save to a new file name every time, or delete previous files with the same file name before running the OSP program.

Evaluation Methods

Fisher Information Determinant

The determinant of the Fisher Information matrix is a measure of the information within sensor network [84, 118]. Higher values of the Fisher Information determinant are therefore preferable. However, the values of the determinant of the Fisher Information vary based upon the model, making it hard to judge comparatively [118]. Analysis should consider the changes in the value as sensors are removed, or the normalized by the initial value [118].

Trace of Fisher Information Matrix

The trace of the Fisher Information matrix is a measure of the estimate error covariance matrix, and is therefore a metric of the accuracy of the sensor information [12, 84]. The larger the trace value, the smaller

the estimate error covariance matrix, leading to better state estimates [84]. The trace can be analyzed using its percent reduction from the initial, full model value [12].

Condition Number of Fisher Information Matrix

The condition number of the Fisher Information matrix is a measure of the sensitivity of the estimates to analytical modeling error [12, 84]. The smaller the condition number, the less sensitive the sensor networks state estimates will be to modeling errors [12]. The condition number can be analyzed by comparing its values as sensors are removed to the initial, full model value.

Maximum Off-Diagonal MAC Value

The MAC is a measure of the correlation between two mode shape matrices. When analyzing the MAC of a mode shape to itself, the off-diagonal terms show the correlation between mode shapes [12]. This is a measure of the linear independence of the mode shapes from the measured DOF. The smaller the off-diagonal MAC terms, the more linearly independent the measurements are. This evaluation is the maximum value of the off-diagonal MAC.

Singular Value Decomposition Ratio

The SVD ratio is the ratio of the largest and smallest singular values of the mode shape for the measured DOF, and monitored modes. The SVD equation is shown in equation 9.12, with the SVD ratio presented in equation 9.24.

$$SVD_{ratio} = \frac{\mathbf{max}(SVD)}{\mathbf{min}(SVD)} \tag{9.24}$$

The closer the SVD ratio is to unity the better the sensor network, with values ranging from one to infinity [118]. The SVD ratio is a measure of the mode orthogonality, capability for modal expansion, and observability of modes. Further explanation of these principles is provided by Penny, Friswell, and Garvey [118].